NOTICE

AVIS

The quality of this microform is heavily dependent upon the quality of the original thesis submitted for microfilming. Every effort has been made to ensure the highest quality of reproduction possible.

If pages are missing, contact the university which granted the degree.

Some pages may have indistinct print especially if the original pages were typed with a poor typewriter ribbon or if the university sent us an inferior photocopy.

Reproduction in full or in part of this microform is governed by the Canadian Copyright Act, R.S.C. 1970, c. C-30, and subsequent amendments.

La qualité de cette microforme dépend grandement de la qualité de la thèse soumise au microfilmage. Nous avons tout fait pour assurer une qualité supérieure de reproduction.

S'il manque des pages, veuillez communiquer avec l'université qui a conféré le grade.

La qualité d'impression de certaines pages peut laisser à désirer, surtout si les pages originales ont été dactylographiées à l'aide d'un ruban usé ou si l'université nous a fait parvenir une photocopie de qualité inférieure.

La reproduction, même partielle, de cette microforme est soumise à la Loi canadienne sur le droit d'auteur, SRC 1970, c. C-30, et ses amendements subséquents.

Canada

THE UNIVERSITY OF ALBERTA

MAGNETIC ANISOTROPY IN THE HIGH TRANSITION TEMPERATURE
SUPERCONDUCTOR $YBa_2Cu_3O_{7-\delta}$

BY

$\copyright$ ADO UMEZAWA

A THESIS

SUBMITTED TO THE FACULTY OF GRADUATE STUDIES AND

RESEARCH IN PARTIAL FULFILMENT OF THE REQUIREMENTS FOR

THE DEGREE OF DOCTOR OF PHILOSOPHY

DEPARTMENT OF PHYSICS

EDMONTON, ALBERTA

FALL, 1991

The author has granted an irrevocable non-exclusive licence allowing the National Library of Canada to reproduce, loan, distribute or sell copies of his/her thesis by any means and in any form or format, making this thesis available to interested persons.

The author retains ownership of the copyright in his/her thesis. Neither the thesis nor substantial extracts from it may be printed or otherwise reproduced without his/her permission.

L'auteur a accordé une licence irrévocable et non exclusive permettant à la Bibliothèque nationale du Canada de reproduire, prêter, distribuer ou vendre des copies de sa thèse de quelque manière et sous quelque forme que ce soit pour mettre des exemplaires de cette thèse à la disposition des personnes intéressées.

L'auteur conserve la propriété du droit d'auteur qui protège sa thèse. Ni la thèse ni des extraits substantiels de celle-ci ne doivent être imprimés ou autrement reproduits sans son autorisation.

Canada

THE UNIVERSITY OF ALBERTA

RELEASE FORM

NAME OF AUTHOR: ADO UMEZAWA

TILE OF THESIS: MAGNETIC ANISOTROPY IN THE HIGH TRANSITION TEMPERATURE SUPERCONDUCTOR $YBa_2Cu_3O_{7-\delta}$.

DEGREE: DOCTOR OF PHILOSOPHY

YEAR THIS DEGREE GRANTED: FALL 1991

Permission is hereby granted to THE UNIVERSITY OF ALBERTA LIBRARY to reproduce single copies of this thesis and to lend or sell such copies for private, scholarly or scientific research purposes only.

The author reserves other publication rights, and neither the thesis nor extensive extracts from it may be printed or otherwise reproduced without the author's written permission.

(SIGNED) ....

Permanent Address:

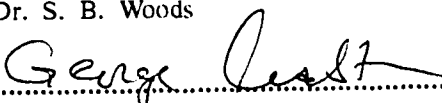14116   52 Ave.

Edmonton, Alberta

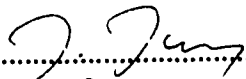CANADA T6H 0P8

DATED ...23 July..... 19 71
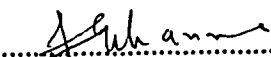
THE UNIVERSITY OF ALBERTA
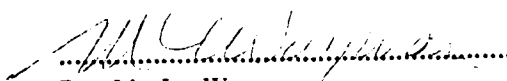
FACULTY OF GRADUATE STUDIES AND RESEARCH

The undersigned certify that they have read, and recommend to the Faculty of Graduate Studies and Research for acceptance, a thesis entitled MAGNETIC ANISOTROPY IN THE HIGH TRANSITION TEMPERATURE SUPERCONDUCTOR $YBa_2Cu_3O_{7-\delta}$ submitted by Ado Umezawa in partial fulfillment of the requirements for the degree of Doctor of Philosophy in Physics.

Dr. S. B. Woods
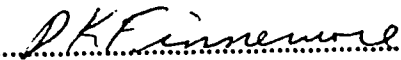
Dr. G. W. Crabtree

Dr. J. Jung

Dr. F. C. Khanna

Dr. M. L. Wayman

Dr. D. K. Finnemore

Date: ...June...05...,.1991...

This thesis is dedicated to my wife Yukako. I have received so much more than I have given.

ABSTRACT

The strong anisotropy found in the electronic structure of $YBa_2Cu_3O_{7-\delta}$ resulting from the existence of both the CuO_2 planes within the a,b plane and the CuO chains along the b axis has brought strong interest regarding the effect of the electronic structure anisotropy on the superconducting properties in this material. Such superconducting properties include both the intrinsic type (such as H_{c1}, H_{c2}, H_c, λ, ξ ....) and the non-intrinsic type (such as flux pinning and j_c). The availability of twinned and more recently, untwinned single crystals of $YBa_2Cu_3O_{7-\delta}$ has made it possible for such anisotropic properties to be investigated. Magnetization critical currents (j_c) were measured for H//c and H//a,b in order to investigate the characteristics of flux pinning. The temperature dependence of j_c was measured up to 77 K, to determine the viability of the material for application use at such high temperatures. Irradiation of the single crystals with high energy neutrons is also done to investigate the possibility of using such a method for increasing j_c. Intrinsic superconducting parameters are investigated by measuring the magnitude and anisotropy of the lower critical field H_{c1} and comparing it to the measurements of the upper critical field H_{c2}. From these values the magnitude and anisotropy of the other characteristic values such as λ, κ and H_c are estimated using an anisotropic Ginzburg-Landau model. The temperature dependence of H_{c1} was found to give unusual results, which differed with the direct temperature dependent measurements of the magnetic penetration depth λ.

The lower critical field was measured on an untwinned single crystal of $YBa_2Cu_3O_{7-\delta}$, to investigate both the a-b anisotropy and the effects of the twin boundaries on the measurements of H_{c1}.

ACKNOWLEDGEMENTS

Table of Contents

List of Tables

List of Figures

Ch.1 <u>Introduction</u>

Since the observation of zero resistivity in mercury at 4 K by H. K. Onnes in 1911[1], superconductivity has been a subject of interest in solid state physics. Its combined characteristics of zero resistivity and diamagnetism have enticed researchers into investigating and understanding its physical properties. However, the very low temperatures at which these materials undergo a superconducting phase transition have limited the technological and practical applications of superconductivity to areas in which such characteristics are absolutely necessary or where low temperatures are readily available. For most applications however, the trouble obtaining and maintaining such low temperatures far outweighs the convenience of getting perfect conductivity and diamagnetism. Thus one of the major areas of research in superconductivity has been in finding a method for increasing the superconducting transition temperature T_c.

The study of metallic oxide superconductors existed as far back as 1964 with the discovery of superconductivity in $SrTiO_3$ with a transition temperature of approximately $0.3K$[2]. However the major breakthrough in oxide superconductivity came in 1986 when J. G. Bednorz and K. A. Müller found that the mixed-valent perovskite compound $(La_{1-x}Ba_x)_2CuO_4$ underwent a superconducting transition at $T_c(onset)=30K$[3], the highest superconducting transition temperature observed at that time. In the early part of 1987, M. K. Wu and C. W. Chu found the

1

compound Y-Ba-Cu-O to become superconducting at approximately 90K[4]. This discovery created much excitement in solid state physics for it was the first material whose superconducting transition temperature was observed above 77K, the boiling temperature of liquid nitrogen. Practical applications of superconductors in liquid nitrogen became a possibility and a significant surge in the study of superconductivity followed. Since then, several other classes of oxide systems have been found to exhibit superconductivity at high temperatures[5-8]. Table 1-1 lists chronologically some of the most important high T_C oxide superconductors and their transition temperatures to date. A graphical representation of the major breakthroughs in T_C since the original discovery of superconductivity in mercury in 1911 is shown on Figure 1-1. Figure 1-1 gives the reader a picture of just how significant a discovery these high T_C superconductors were.

Structural studies have shown that the majority of these high T_C superconductors have a variation on the perovskite structure as will be discussed in greater detail in Chapter 2. The CuO_3 octahedron found within the perovskite structure is elongated along one direction creating a strong bonding CuO_2 plane with weaker Cu-O bonds along the elongated direction[9,10]. This layered network of CuO_2 planes in the crystal structure has been commonly observed in the majority of high T_C superconductors with the exception being the cubic perovskite structured $Ba_xK_{1-x}BiO$ compound[11,12]. The elongation of the CuO bond along one axis makes electron conduction along that direction lower than

2

Table 1-1

List of High T_c Oxide Superconductors

Compound	T_c	Discovered by
LaBaCuO		J. G. Bednorz, K. A. Muller (1986)
$(La_xBa_{1-x})_2CuO_4$	40 K	
$La_{1.85}Sr_{.15}CuO_4$	45 K	
YBaCuO		W. K. Wu, C. W. Chu (1987)
$YBa_2Cu_3O_7$	90 K	
$YBa_2Cu_4O_8$	85 K	
BiSrCaCuO		H. Maeda, et al. (1988)
$Bi_xSr_2CaCu_2O_y$	85 K	
$Bi_xSr_2Ca_2Cu_3O_y$	115 K	
TlBaCaCuO		Z. Z. Sheng, A. M. Hermann (1988)
$Tl_xBa_2CaCu_2O_y$	100 K	
$Tl_xBa_2Ca_2Cu_3O_y$	120 K	
†$Ba_xK_{1-x}BiO$	30 K	R. J. Cava, et al.(1988)
*$Nd_{2-x}Ce_xCuO_4$	20 K	Y. Tokura, H. Takagi and S. Uchida (1989)

†First high T_c oxide superconductor found with cubic perovskite symmetry
*First high T_c oxide superconductor found having electrons as charge carriers

Figure 1-1

Tc (K)

Date

Hg

Nb3Sn

SrTiO

NbGe

LaSrCuO
LaBaCuO

YBaCuO

BiSrCaCuO

TlBaCaCuO

BaKBiO

NdCeCuO

4
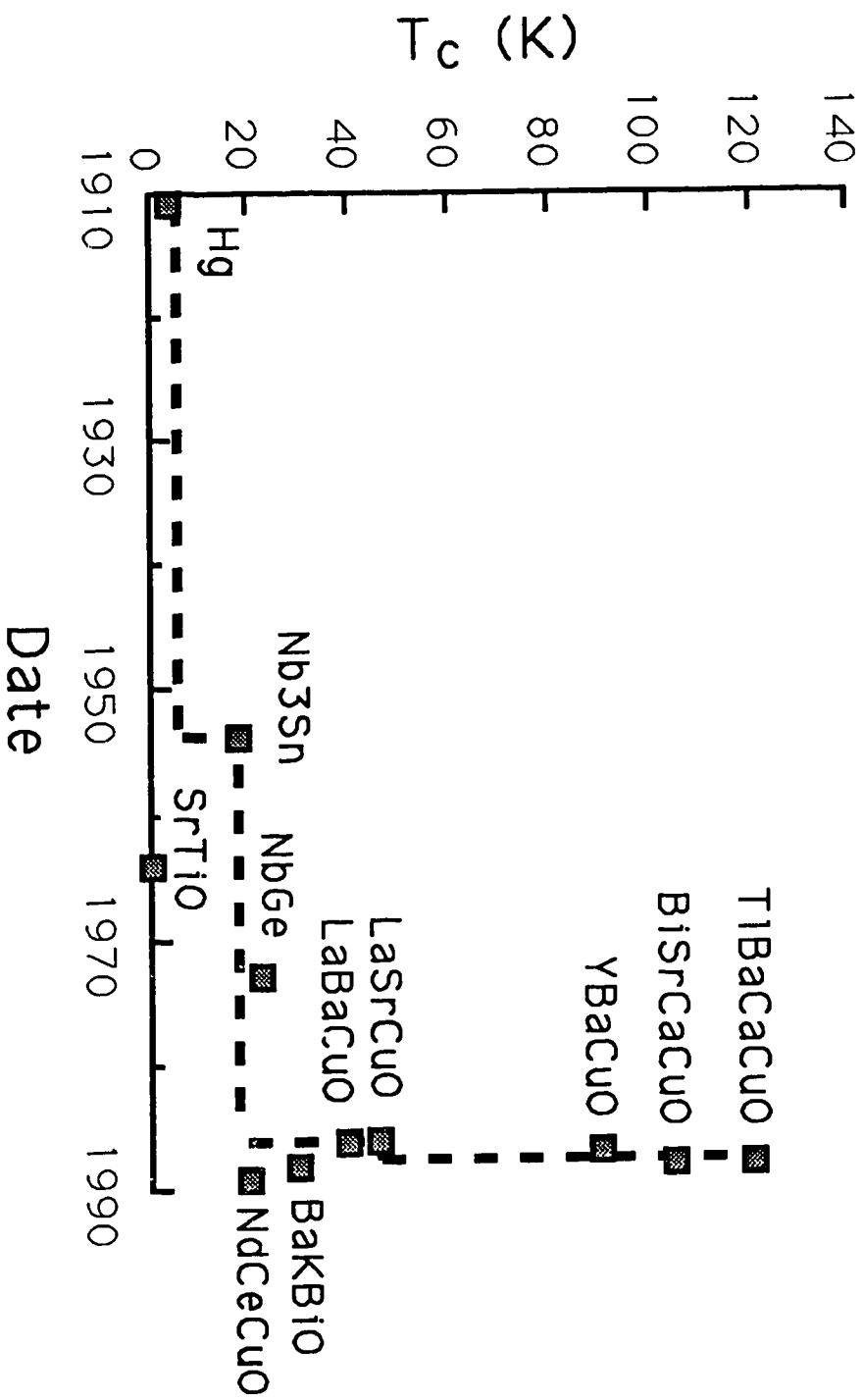
the conduction within the stronger bonding CuO_2 plane resulting in a 2-D like behavior in the electronic structure of these systems.

At present, the mechanism of these new high T_c superconductors is not yet fully understood. However there has been some interest focused on the possibility of the layered anisotropy having an effect on the superconducting mechanism. Even before the discovery of high T_c superconductors, W. A. Little[13] and V. L. Ginzburg[14] suggested an increase in T_c for lower dimensional superconductors through a possible excitonic mechanism instead of the traditional electron-phonon mechanism. Since the discovery of the high T_c oxides, theorists have speculated on if and how the low dimensional electronic structure of the CuO layered system may influence its superconducting properties[15-17]. To determine the significance of these theories, it has become important to determine whether or not anisotropy strongly influences the superconductivity of these materials, and the exact nature and consequences of this effect.

Recent availability of single crystals, has made the study of anisotropy in these systems possible[18-20]. Measurements of the magnetic and transport properties have yielded insight into the anisotropic effects on superconductivity. In particular, upper and lower critical field measurements done on single crystal high T_c superconductors have given insight into the two fundamental characteristic lengths, the coherence length and the penetration depth[21-23]. Both these values are found to be anisotropic and their ratio gives a large value of the Ginzburg-Landau (GL) parameter κ.

5

Several problems have made the analysis of the anisotropic properties of these oxide superconductors very difficult. In $YBa_2Cu_3O_{7-\delta}$, twin boundaries along the <110> type directions have until recently obscured any distinction between the a and b axis of the CuO_2 plane for the orthorhombic crystals[24]. Diverse oxygen concentrations and multiple superconducting phases in many of these systems have made the production of high quality single crystals a non-trivial task[25,26]. Strong flux pinning observed in the mixed state of these materials has influenced the intrinsic magnetic characteristics of these superconductors and has made the determination of the lower critical field very difficult[27]. Finally the limited range of the size and shape of the single crystals has complicated the experimental measurements in these materials[18-20].

In the following chapters we will analyze some of the anisotropic properties in these high transition temperature superconductors. Emphasis will be placed on measurements of the upper and lower critical fields of $YBa_2Cu_3O_{7-\delta}$ and also the determination of the characteristic lengths and the GL parameter, κ. These will be analyzed using existing anisotropic theories including the effective mass theory. The anisotropy of the non-equilibrium flux pinning behavior will also be discussed in connection with some measurements taken on magnetization of single crystals of these materials. From the magnetization curves, some values of the magnetic critical currents can be calculated using the Bean model[29]. The results of these measurements will be

6

analyzed and compared with other measurements to give a general picture of the anisotropic properties of the high T_c superconductors to date.

Ch. 2 Structural Anisotropy

Anisotropy in the Crystal Structure

The basic structure of the high T_c superconductors is derived from a simple cubic perovskite form having the formula ABO_3. This structure is a combination of the face centered and body centered cubic structures where element A is situated on the corners of the unit cell with element B in the body center of the cell surrounded on the center of each face by oxygen atoms O. Figure 2-1 shows the structure of a cubic perovskite. The element B has six fold symmetry with the surrounding oxygens and the cubic structure is symmetric in the three dimensions such that all three primitive translational vectors are the same magnitude.

La-Ba-Cu-O, the original high T_c superconductor found by Bednorz and Müller[3], is a variation on the perovskite ABO_3 structure where A=La or Ba and B=Cu. X-ray and neutron diffraction measurements have found the structure to be tetragonal with a parent structure of K_2NiF_4 and having two formula units per unit cell[9,10]. Figure 2-2 shows the structure of $(La_{1-x}Ba_x)_2CuO_4$. At the center of the cell is a CuO_4 octahedron surrounded by La or Ba atoms. The octahedron consists of Cu with four strongly bonded oxygen atoms in a square planar arrangement (O1) and two other oxygens situated above and below the CuO_2 plane at a larger distance (O2). This results in the cubic perovskite structure being elongated along the c direction of the

8

Figure 2-1

Structure of ABO$_3$ Perovskite
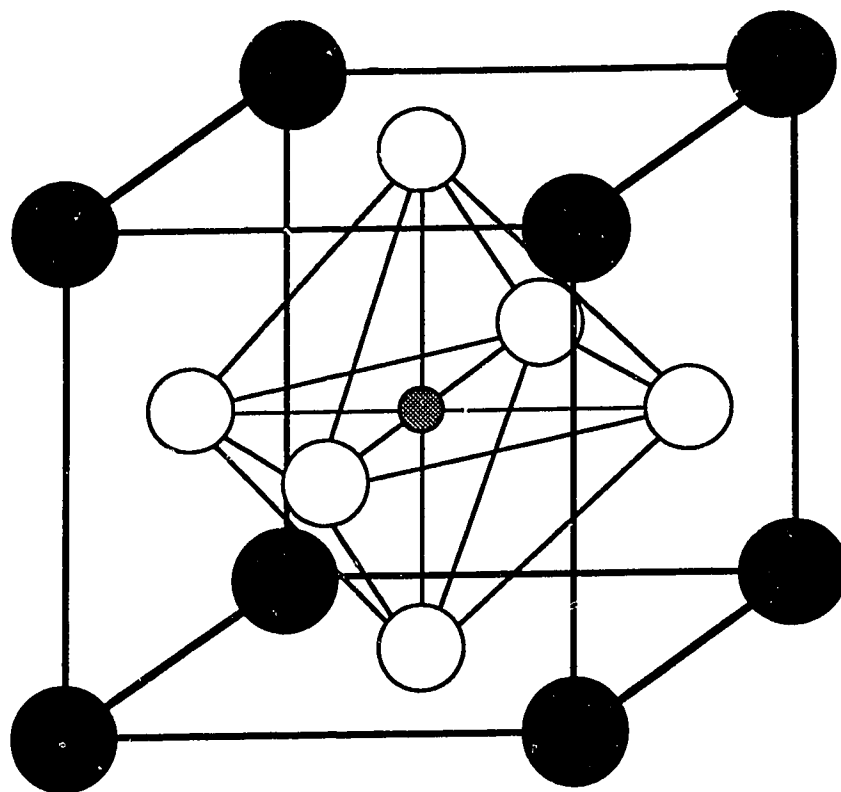
A = La, Ba, Sr

O = Oxygen

B = Cu

Figure 2-2

Structure of $(La_{1-x}Ba_x)_2CuO_4$
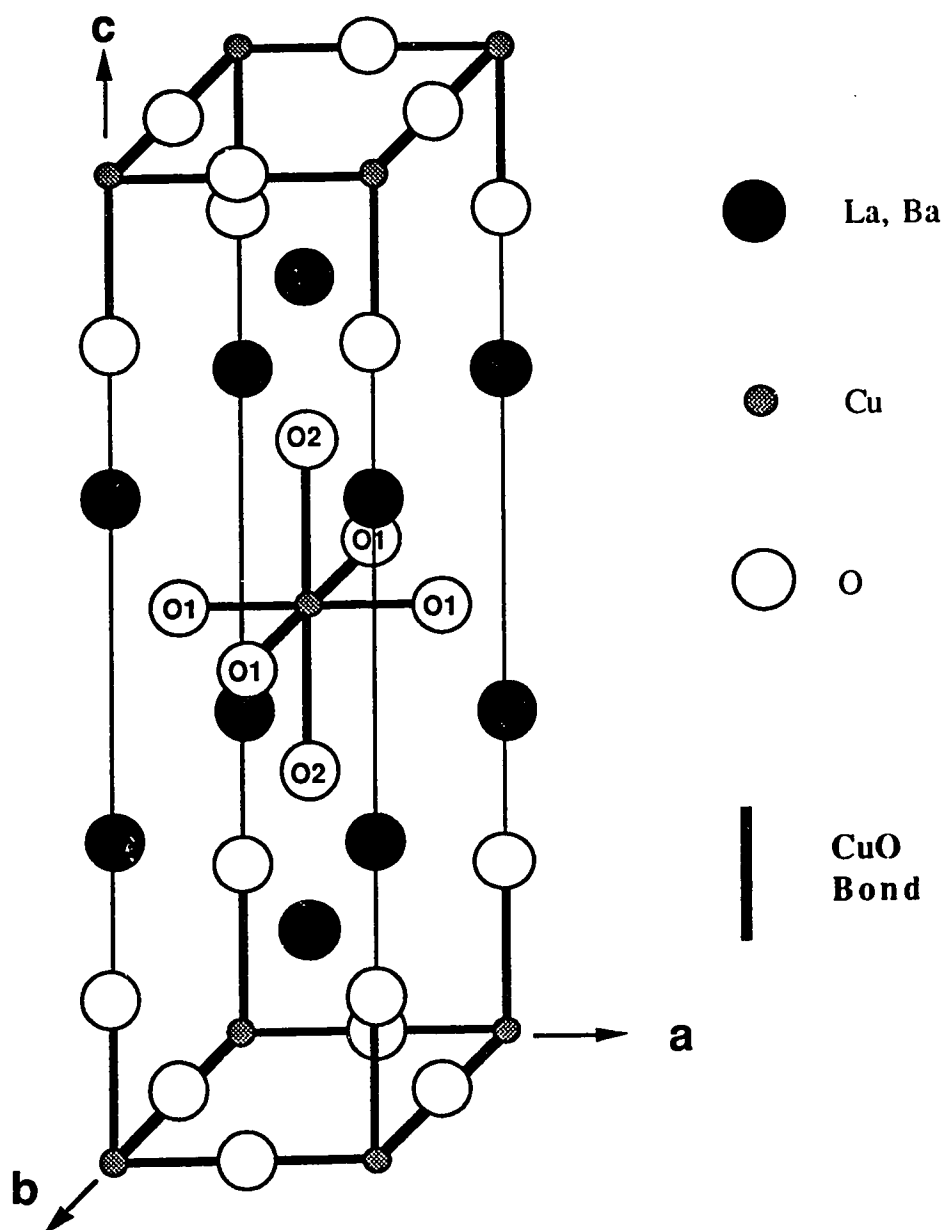
cell and the formation of a planar layer of Cu and O1 atoms. Above and below this perovskite structure there is another layer of elongated perovskites that are shifted along the a and b axes by half a unit cell resulting in the CuO_4 octahedra being situated at the corners of the unit cell of $(La_{1-x}Ba_x)_2CuO_4$. This structure is often said to be an alternating layer arrangement of perovskite $(LaCuO_3)$ and rocksalt (LaO) structures and results in a network of planar CuO_2 layers. There are two formula units and two CuO_2 layers per unit cell of this system. The dimensions of the unit cell are 3.8 Å x 13.2 Å for the tetragonal structure[10].

The 90 K superconductor, $YBa_2Cu_3O_{7-\delta}$ has a more complex structure, where a stacking of three ABO_3 type perovskites make up one unit cell[30-33]. Figure 2-3 shows the diagram of the unit cell of $YBa_2Cu_3O_{7-\delta}$. The A element in this case is Y or Ba and compared to a true perovskite structure, there are two key oxygens missing in the unit cell. The oxygens at the center of the c axis and the corners of the a,b plane surrounding the Y site are missing. Also the oxygen located at the top and bottom plane along the a direction (O5) is missing causing an orthorhombic distortion in the unit cell. The absence of the O5 oxygens in the top and bottom plane destroys the planar CuO_2 structure forming one dimensional periodic chains of Cu and O sites along the b direction. Also, the oxygen between the chains and the planes (O4) moves towards the CuO chain weakening the bonding between it and the Cu on the CuO_2 planes. This produces a planar effect

Figure 2-3

Structure of YBa₂Cu₃O₇
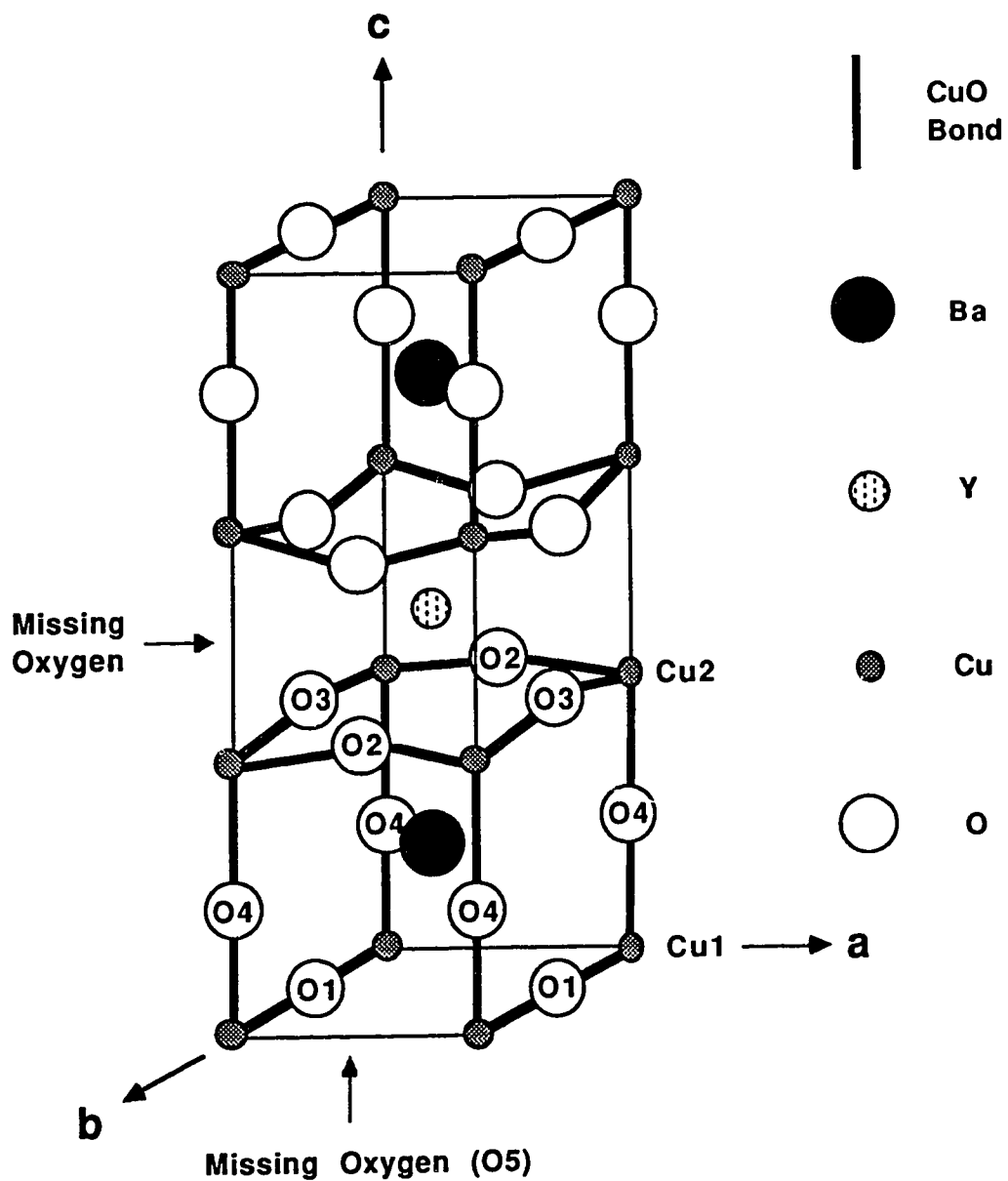
between the copper and the remaining oxygens (O2, O3) with the unit cell containing two CuO_2 planes per unit cell. The unit cell dimensions are a=3.82 Å, b=3.88 Å, c=11.67 Å with one formula unit per cell[30].

A particular characteristic of $YBa_2Cu_3O_{7-\delta}$ systems results from the near tetragonal nature of the orthorhombic unit cell. The similar magnitude of the a and b axes creates domains in the system where the a and b axes interchange from one domain to the next. These domains are separated by boundaries running along the <110> and <$\bar{1}$10> direction as illustrated by Figure 2-4. These boundaries, often described as (110) mirror twins, have been investigated by electron microscopy[34-36,24] and polarized light microscope[37,38]. The thickness of the twin boundary layer has been found to be about 1.0 nm for $YBa_2Cu_3O_{7-\delta}$[24]. The mixture of the a and the b axes in the single crystals of $YBa_2Cu_3O_{7-\delta}$ have obscured any differences in the physical properties between them. Thus anisotropic measurements, even in single crystals, have in most cases been between the c axis and the a,b plane. Recently, certain growth techniques[39] and post growth annealing[38] techniques have been found to produce crystals of a single domain with no observable twin boundaries. This has in turn made it possible not only to observe the difference in the physical properties between the a and b axis but also the physical characteristics resulting from the twins themselves. Some of these properties will be discussed in the following chapters.

13

Figure 2-4
Twin Boundaries in $YBa_2Cu_3O_{7-\delta}$

● Cu1 sites   ○ O1 sites

Twin Boundary
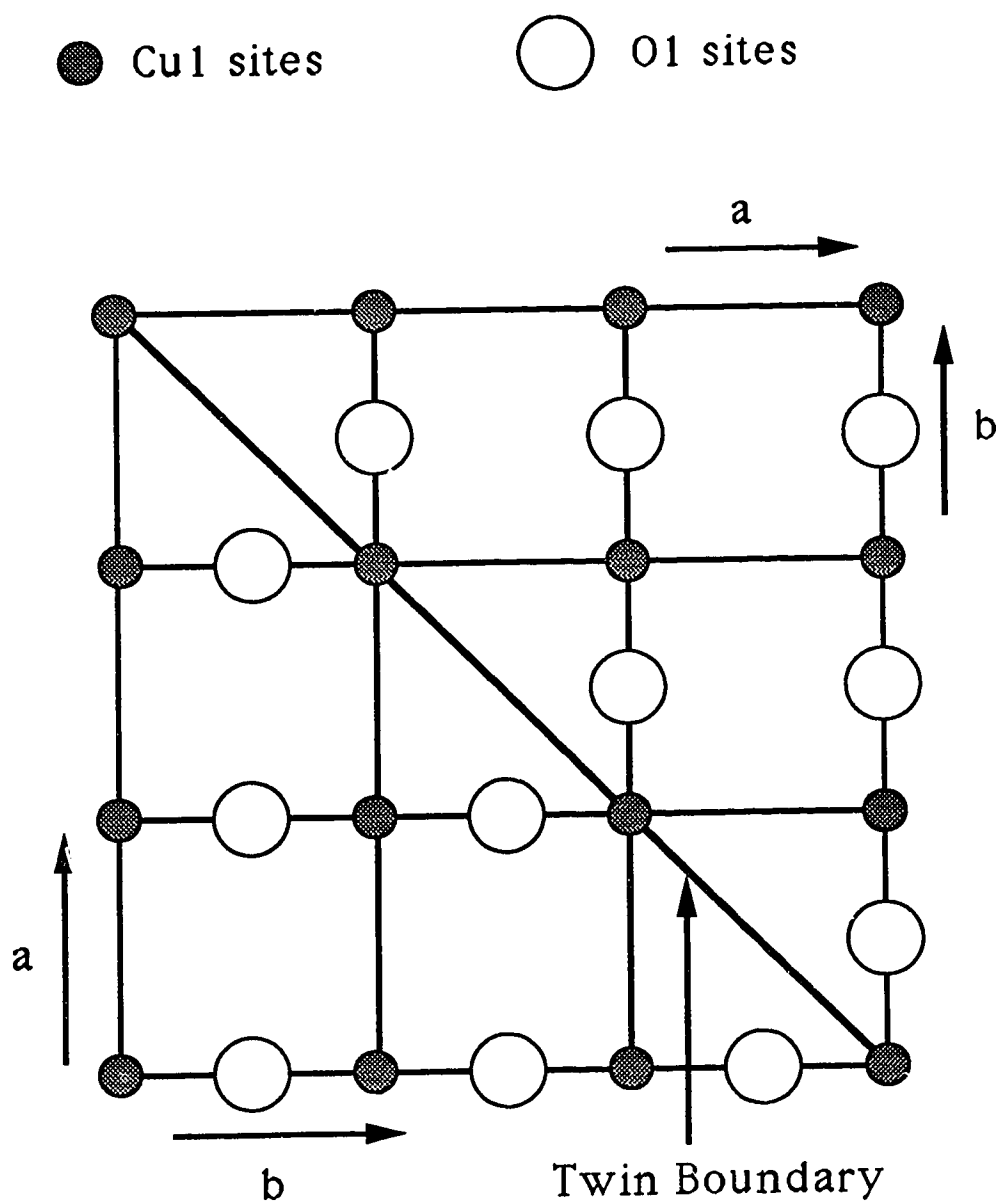
The crystal structures of the Bi and Tl based superconductors are very complicated. The difficulty in obtaining pure phases of the superconducting material and the complexity in the structure of the superconducting phases (as will be discussed) has made the determination of the crystal structure a difficult task[40]. The Bi and Tl structure is said to have similar characteristics to the phases in both the La-Ba-Cu-O and Y-Ba-Cu-O systems. The subcell structure contains a combination of CuO_2 layers and rocksalt like (AO) BO (AO) layers where A is Sr/Ba and B is Bi/Tl, similar to the La-Ba-Cu-O systems. Further, the oxygen deficient Ca planes separating the CuO_2 planes from each other are similar to the oxygen deficient Y planes found in the Y-Ba-Cu-O systems. The oxygen coordinates can be divided into three main groups. First there are the oxygens (O1) that are located in a square planar arrangement with the copper atoms. There are also oxygen atoms (O3) in the A(Sr/Ba) layer bonded to the copper atoms along the c axis. Finally there are the oxygen atoms (O2) located on the B(Bi/Tl) layer at the top and bottom of the unit cell. The O3 atoms are further from the Cu atoms than the O1 atoms resulting in the formation of planar CuO_2 layers. Several superconducting phases have been found to exist within these systems with the notable differences in the structures being the number of CuO_2 layers present within the unit cell. The minimum number of layers is one CuO_2 layer per unit cell found in $Bi_ySr_2CuO_x$ and $Tl_yBa_2CuO_x$ as shown in Figure 2-5[41-44]. $Bi_ySr_2CaCu_2O_x$ and $Tl_yBa_2CaCu_2O_x$

15

Figure 2-5

Structure of $(Bi,Tl)(Sr,Ba)_2CuO_5$
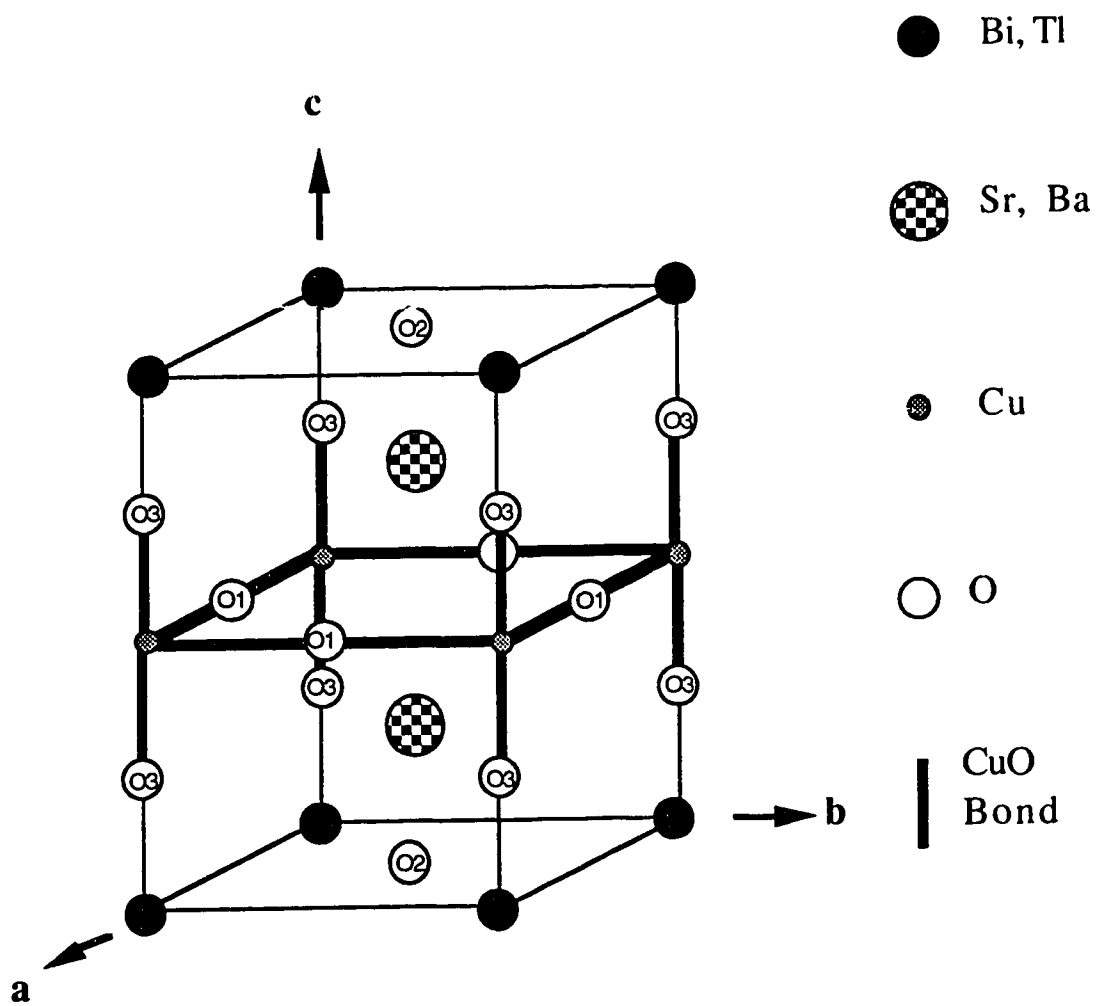
(often called the 1212 or 2212 phase) have two CuO_2 layers per unit cell[45-48], as shown in Figure 2-6, while $Bi_ySr_2Ca_2Cu_3O_x$ and $Tl_yBa_2Ca_2Cu_3O_x$ (often called the 1223 or 2223 phase) contain three CuO_2 planes per unit cell[45,47,49] as shown in Figure 2-7. The general chemical formula for these systems can be written as $B_yA_2Ca_{n-1}Cu_nO_x$ where element B is Bi or Tl, element A is Sr or Ba and n is the number of CuO_2 planes[40]. The subscript y represents the number of Bi or Tl in the unit cell where y=1 or 2, depending upon whether there is a doubling of the Bi or Tl layer in the cell or not. For y=1, the Bi or Tl layers which are situated at the top and bottom of the unit cell are shared by the neighboring cells. For y=2 the neighboring cells do not share the Bi or Tl layers but instead have their own layers such that there are two adjacent layers between two adjacent unit cells. For y=2, these layers and thus their unit cells are said to shift along both the a and b axes by 1/2 a unit cell. Thus the primitive translational vectors span two unit cells in the c axis. The unit cell structure of $Bi_ySr_2CaCu_2O_8$ where y=2 is given in Figure 2-8.

Anisotropy in the Electronic Structure

The electronic structure and its anisotropy found in these high T_c materials seem to correspond with their crystal structure. Band calculations on the $(La_{1-y}X_y)_2CuO_4$[50], the $YBa_2Cu_3O_7$[51], and the $Bi_2Sr_2CaCu_2O_x$[52] systems have found low dimensional Fermi surfaces suggesting anisotropic electronic properties for these

17

Figure 2-6

Structure of $(Bi,Tl)(Sr,Ba)_2CaCu_2O_7$

● Bi, Tl

▨ Sr, Ba

◪ Ca

• Cu

○ O

▮ CuO Bond

18
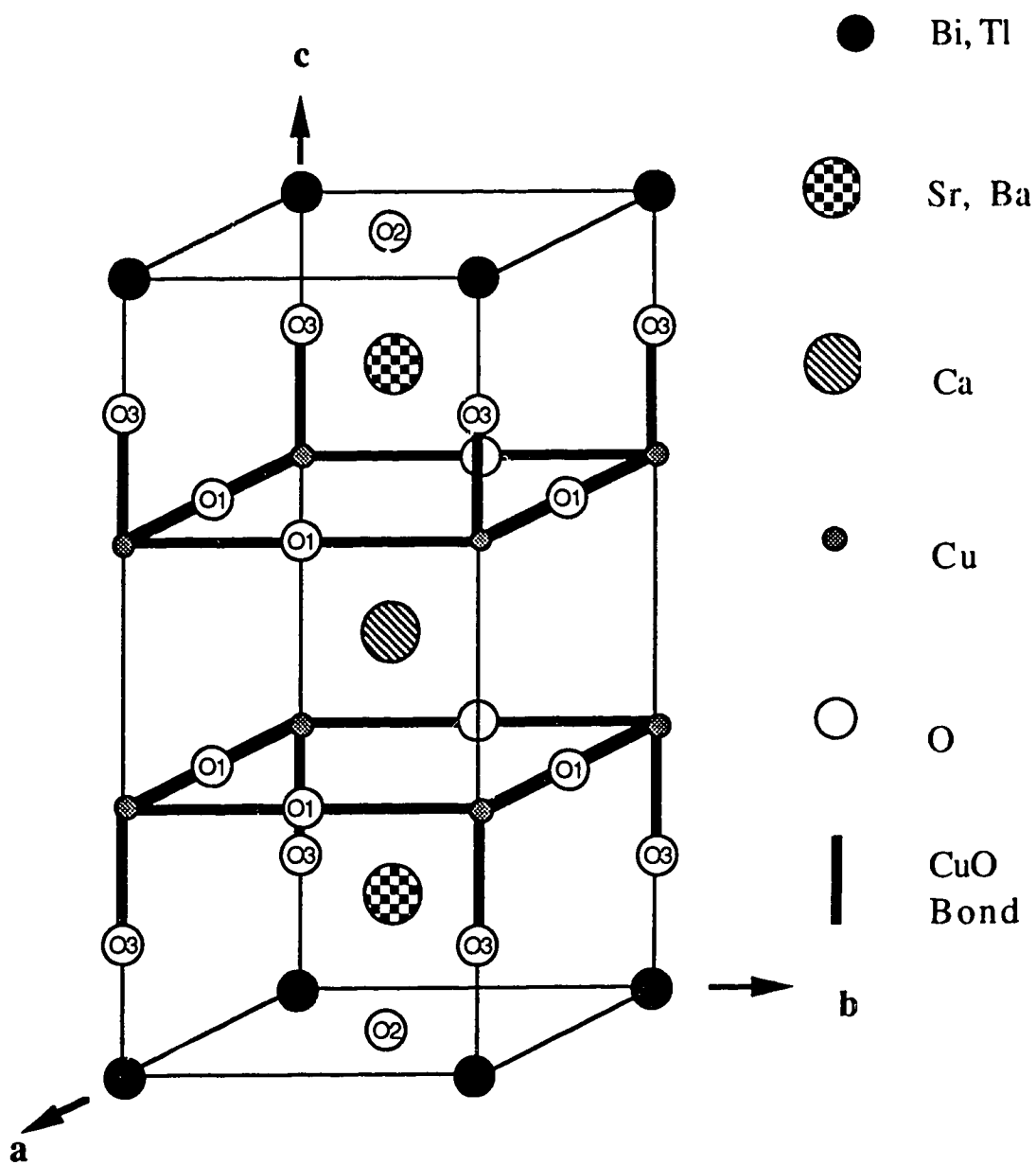
Figure 2-7

Structure of $(Bi,Tl)(Sr,Ba)_2Ca_2Cu_3O_9$

●   Bi, Tl

▦   Sr, Ba

◍   Ca

•   Cu

○   O
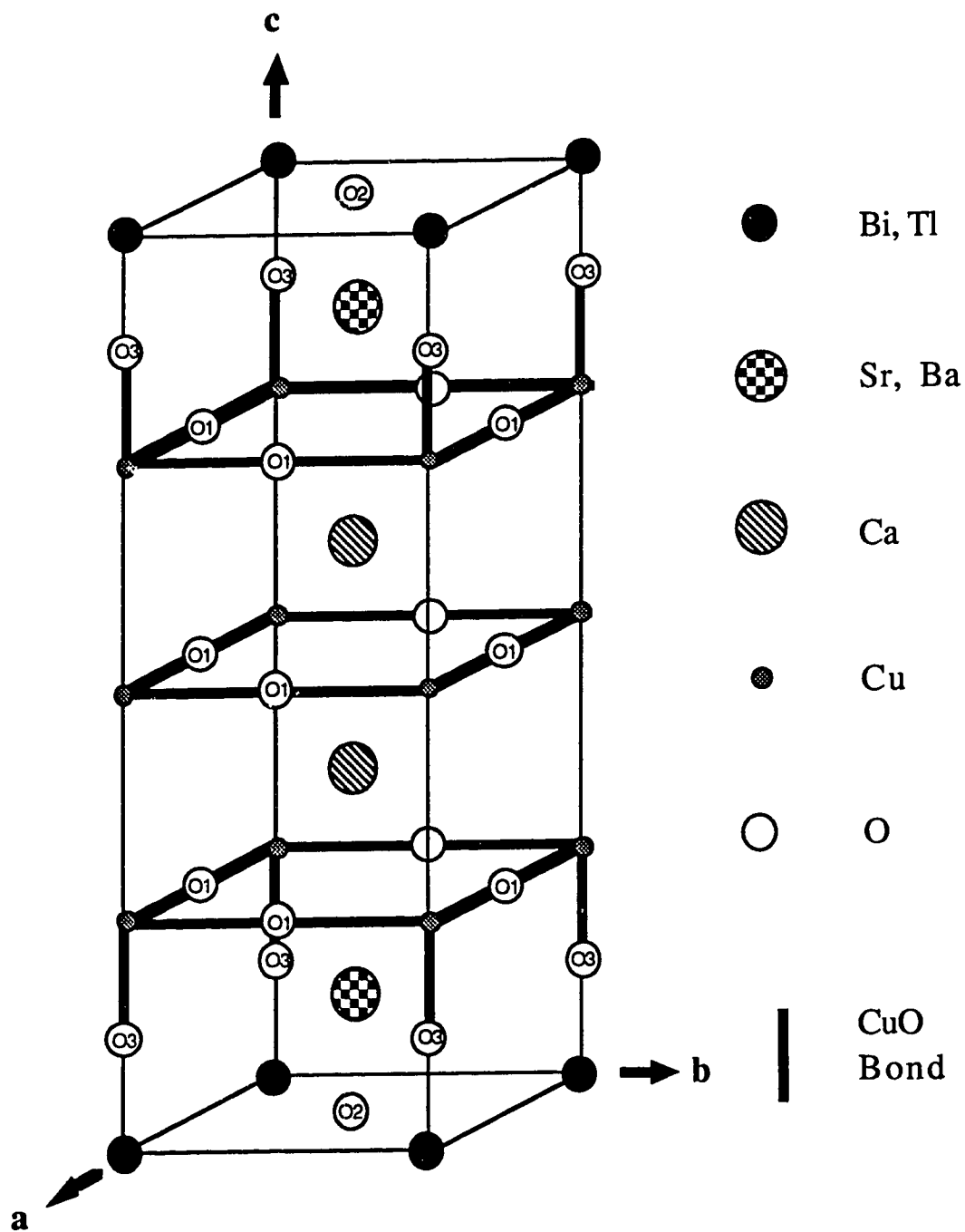
| CuO Bond

Figure 2-8
Structure of Bi2CaSr2Cu2O8

● Bi

⊗ Sr

◉ Ca

• Cu

○ O

| CuO
ı Bond

20
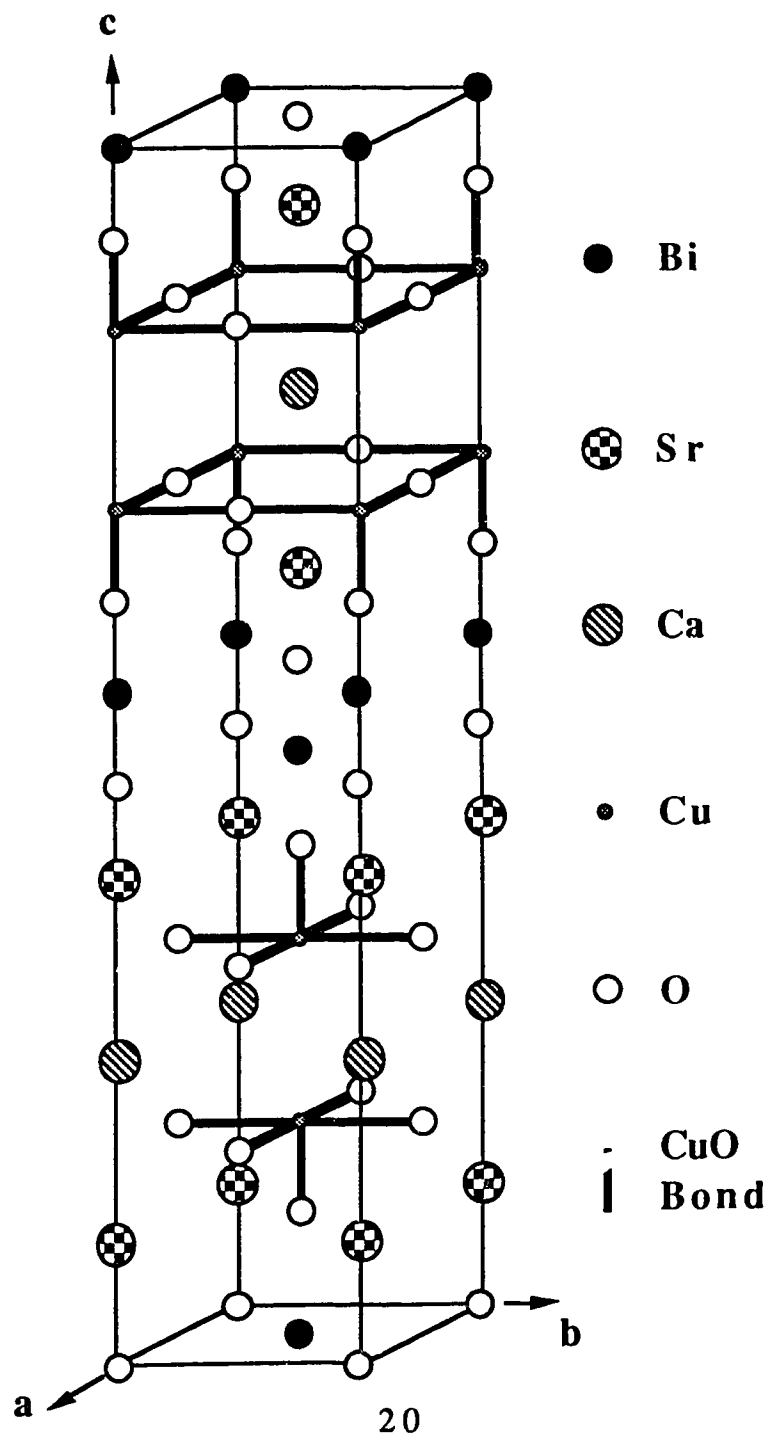
materials. The electronic structure is dominated by a layered character arising from the in-plane $Cu(3d)-O(2p)$ electron interaction while weaker bands were found for the Cu-O bonds along the c direction. The two dimensional Fermi surface which results from these bands consists of square hole surfaces. Band calculations on $YBa_2Cu_3O_{7-\delta}$ have also found a two dimensional nature to the band structure resulting from the $Cu2(3d)-O2(p)-O3(p)$ interactions in the CuO_2 plane. Further, one dimensional character bands were found from the $Cu1(d)-O1(p)-O4(p)$ interactions occurring in the chains. Thus the Fermi surface of $YBa_2Cu_3O_{7-\delta}$ falls naturally into the two-dimensional-like closed sheets resulting from the CuO_2 planes and the one-dimensional-like flat sheets from the Cu-O chains as shown in Figure 2-9. The ionic Y and Ba bands were found to have little interaction with these low dimensional bands. Positron annihilation experiments done on $YBa_2Cu_3O_{7-\delta}$ have found the electronic structure of this material to be two dimensional, in agreement with the band structure calculations[53]. For the Bi-Sr-Ca-Cu-O systems, the electronic system consists primarily of states resulting from the $Cu(d)-O(p)$ interaction as well as from the Bi-O interaction. The resulting Fermi surface consists of a two-dimensional-like hole surface arising from the Cu-O bands and a small electron surface arising from the Bi-O bands. The strong two dimensionality results from the existence of the non-interacting Ca layer that separates the CuO_2 layers. The low dimensionality found in the Fermi

Figure 2-9
Fermi Surface of $YBa_2Cu_3O_{7-\delta}$
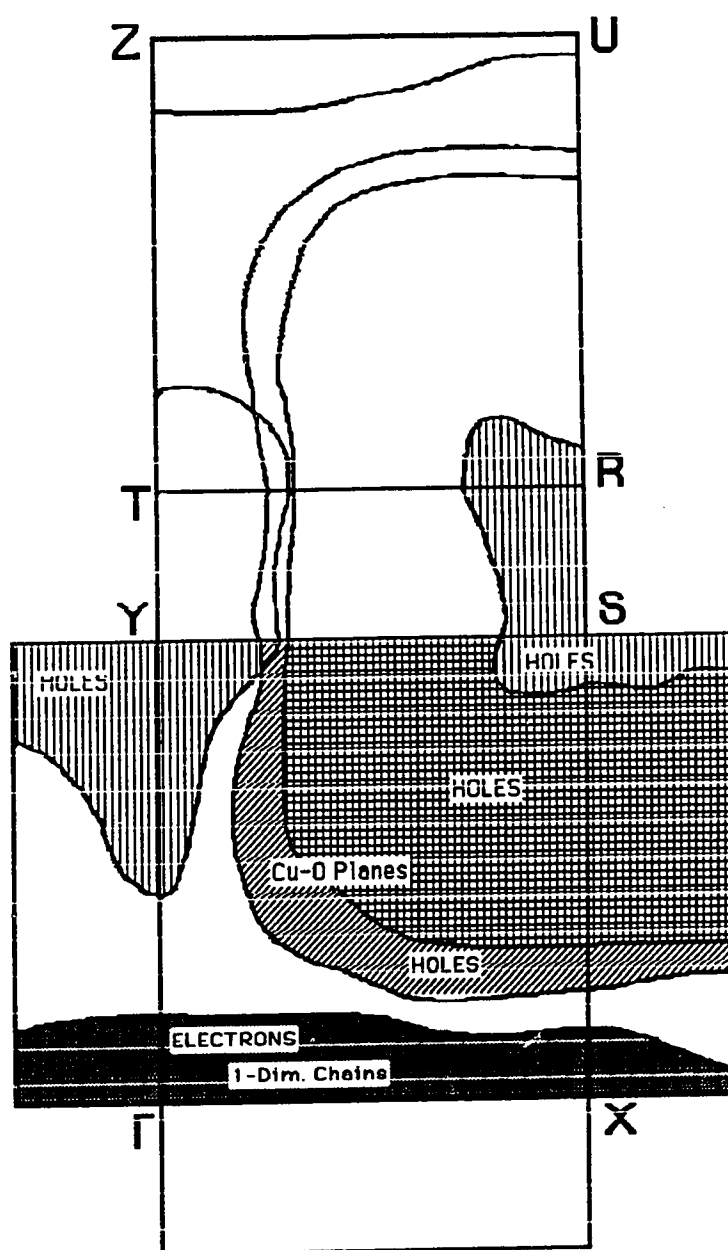
surface of these systems would result in highly anisotropic electronic characteristics for these materials.

The anisotropic layered structure in the Fermi surface of these high T_c materials indicates that the normal state conductivity also should be anisotropic with lower conductivity for currents off the CuO_2 planes than for currents in the planes. Resistive measurements on single crystals of $YBa_2Cu_3O_{7-\delta}$ have found the resistivity for currents along the c direction to be higher than for currents in the a,b plane, with the resistivity anisotropy ranging from 30 to 100 at 300K[54-57]. Resistivity measurements along the a,b plane have found a linear temperature dependence at high temperatures indicating a metallic behavior in the conductivity for currents within the planes. The temperature dependence of the resistivity along the c axis has been controversial, with both increasing and decreasing resistivities observed with decreasing temperatures. It has been said that the semiconductor-like increase in resistivity with decreasing temperatures reflects poor sample quality and oxygen deficiency. Such a statement arises from oxygen deficient studies on single crystals of $YBa_2Cu_3O_{7-\delta}$ where greater increases in the resistivity with decreasing temperatures have been observed for samples having large δ values[58]. Transport measurements done on $Bi_2Sr_{2.2}Ca_{0.8}Cu_2O_8$ single crystals have also found anisotropy in the resistivity[59] with the anisotropy ratio as large as 10^5:1. The c direction resistivity was found to increase with decreasing

temperature. With the small dimensions of the single crystals, especially in the c direction, a detailed investigation of the anisotropy in the normal state resistivity has been very difficult. However preliminary transport measurements on single crystals have found the normal state resistivity of these high T_c materials to be highly anisotropic with the higher conductivity occurring for currents in the CuO_2 planes, in agreement with band structure calculations done on these materials.

Initial indications of localized behavior in the conductivity of the superconducting charge carriers came from transport and inductive measurements on bulk polycrystalline $(La_{1-x}Sr_x)_2CuO_4$ and $YBa_2Cu_3O_{7-\delta}$ substituted with magnetic ions. Traditionally, the superconducting transition temperatures were found to decrease with the addition of magnetic impurities[60] since these magnetic impurities help break the Cooper pairs. Thus the investigation of magnetic ion doping in the high temperature superconductors seemed a logical investigation into the superconducting properties of the high T_c materials. Early resistive and magnetic measurements of Nd-doped polycrystalline $La_{1.85-x}Sr_xCuO_4$ found that although T_c decreased with the addition of Nd ions, there was also a decrease in $\left.\frac{dH_{c2}}{dT}\right|_{T_c}$ (the upper critical field slope near T_c), which could not be explained from orbital pair breaking since the normal state susceptibility from the Nd was too small to give such a decrease[61]. Instead, this decrease seemed to be from the lowering of the effective density

of states as the Fermi level moves off a Van Hove singularity, which was found to exist from band calculations. Thus the change in the transition temperature seemed to occur due to a change in the density of states rather than from a strong magnetic moment.

Soon after the discovery of the 90 K $YBa_2Cu_3O_{7-\delta}$ system, full substitutions of rare earths (Nd, Sm, Eu, Gd, Dy, Ho, Er,Tm Yb, Lu) on the Y site were found to be possible with no significant loss in superconductivity[33,62]. These studies have found that the resistive transition temperature is typically within the 90K range with ΔT_c being about 2K. This small effect of the rare earth ions on the transition temperature suggests that the exchange between the strong magnetic moment of the rare earth and the spin of the superconducting electrons is small since rare earth ions with partially filled 4f electron shells usually depress T_c in conventional superconductors through pair-breaking effects described by the pairbreaking parameter α,

$$\alpha = n\hbar N(E_F)\mathcal{J}^2(g_J-1)2J(J+1) \qquad (2\text{-}1)$$

where n is the concentration of rare earth ions, $N(E_F)$ is the density of conduction electron states at the Fermi level, $\mathcal{J}$ is the exchange interaction parameter and g_J and J are the Landé g-factor and the total angular momentum of the rare earth ion[40]. A small $\mathcal{J}$ indicates minimal overlap between the rare earth 4f orbital wavefunctions and the wavefunctions of the electrons from neighboring CuO_2 planes. Furthermore, recent measurements which correlate the T_c of $RBa_2Cu_3O_{7-\delta}$ (R=rare earth) with the rare

earth ionic radius find the small changes in T_c for the different rare earths to depend more on the size of the rare earth ions than on their 4f moments[63].

Finally, the numerous superconducting phases found in the $B_yA_2Ca_{n-1}Cu_nO_x$ (B = Bi or Tl, A = Sr or Ba) system have proved useful in comparing the superconducting properties of the different phases with respect to their crystal structure. It has been found that the superconducting transition temperature increases with the number of CuO_2 planes that exist within the unit cell[64]. This change in the transition temperature with the number of CuO_2 layers has been observed for both the Bi and the Tl systems. Comparisons between the volume fraction, f_s of the CuO_2 planes within a $B_yA_2Ca_{n-1}Cu_nO_x$ system and its transition temperature have found that T_c relates to f_s by

$$\ln(T_c) \propto (f_s)^{-p} \qquad (2\text{-}2)$$

where p ~ 1. Since Bi and Tl samples having more than four CuO layers have not yet been synthesized, the limit to this increase in T_c is not yet known. However within the systems that are available, this increase in T_c with the number of CuO_2 planes seems to indicate the importance of the layered nature towards the superconducting properties of these oxide systems.

In summary, the crystal structure of the high T_c superconductors are all variations on the perovskite structure which results in a planar CuO_2 network being created in the unit cell. The electronic structures of these high T_c oxides are strongly

26

affected by this planar network in the crystal structure. Thus it is likely that the superconducting properties of these oxides will be affected by the layered CuO_2 planes and will be highly anisotropic. An investigation into the behavior and anisotropy of the superconducting properties in these systems is essential towards understanding the mechanisms of high T_c superconductivity.

Ch. 3 <u>Review of Basic Properties</u>

Though the exact mechanisms of the high temperature superconductivity are not yet fully understood, many of the characteristics are found to be similar to the traditional, low T_c systems. Inductive measurements have found these materials to exhibit magnetic properties similar to the traditional type II superconductors[65,66]. Decoration techniques have shown the existence of a vortex state[67], further confirming the type II nature of the superconductivity. Tunneling[68,69] and infra red absorption[70] measurements have revealed the existence of an energy gap, indicating long range order in the electronic state. A jump in the electronic specific heat at T_c has further confirmed this[71]. Thus, the nature of high T_c superconductors can be understood by observing how the traditional superconducting parameters behave in these materials. Further, the effects from the layered nature of the electronic structure can be analyzed by observing how anisotropy affects these parameters. The following sections will briefly cover some of the key areas and define some of the important parameters in superconductivity. The latter part of this chapter will introduce some existing theories in anisotropic superconductors. This section has been written for the convenience of the reader as a reference to the discussions of the experimental results appearing in the following chapters.

Some of the characteristic properties

The initial discovery of superconductivity by H. K. Onnes[1] came with the observation of zero resistivity in mercury. As the sample was cooled below a certain temperature, T_c, it underwent a superconducting phase transition and the resistivity dropped below the resolution of the measuring instrument. The value of T_c is intrinsic to the material and is stated as being a characteristic property of the superconductivity in that material.

Later Meissner and Oschenfeld[72] found that when a superconductor was cooled through T_c, the system expelled all magnetic fields, exhibiting perfect diamagnetism (called the Meissner effect). At high enough fields however, the superconductivity and Meissner effect are destroyed and the field fully enters the sample. The critical field where the superconductivity is destroyed, H_c, is also an intrinsic, characteristic property of superconductivity. Most superconducting systems were later found to have two magnetic transitions, a lower critical field, H_{c1} where the material loses perfect diamagnetism but remains superconducting and partially diamagnetic, and an upper critical field H_{c2} where the system loses superconductivity altogether. These materials were called type II superconductors, while the superconductors with only one critical field, H_c, were called type I. The type II critical field values are also intrinsic to the superconductor. The relation between the two types of superconductors depends on two characteristic lengths,

29

the magnetic penetration depth, λ and the coherence length, ξ, as will be discussed later.

Finally, the superconducting phase also depends on the current density that passes through the material. At a high enough current density, the material returns to its normal state. This current density is defined as the critical depairing current, J_c. Besides the depairing current there are other critical current densities that are discussed in superconductivity. For type I superconductors, there is the critical current density which describes the surface currents that create a local field that is greater than H_c due to demagnetization effects. For type II superconductors, due to the existence of the mixed state, a critical current is produced from a non-equilibrium, non-uniform distribution of flux vortices which is often described by the critical state. Also, there may be a current at which resistivity is first observed in the system due to the motion of magnetic vortices often called flux creep critical current. These latter J_c's, depend upon non-intrinsic properties which influence the vortex dynamics in type II superconductors. As the high T_c materials are strongly type II materials, these non-intrinsic critical current densities will be discussed later.

Part I: Basic Superconducting Analysis
Cooper pairs and T_c

Some initial insight into the microscopic mechanisms of superconductivity appeared when Frölich extended Bloch's

interpretation of the electron-lattice interaction to that of the emission and absorption of a vibrational quantum[73]. He suggested that attractive interactions between the electrons are possible from the virtual emission and absorption of these vibrational quanta and that the quantum-vibrational motions responsible for this interaction were the phonon vibrations from the lattice.

In 1956, Cooper performed calculations[74] for a model where two electrons are added to a metal at $T = 0$ K such that individually, they are forced to occupy states greater than the Fermi energy, E_F. Cooper showed that if there is an attractive interaction between the two electrons (called Cooper pairs), they can form a bound state with an energy that is less than the sum of their individual energies. It was found that the maximum lowering of energy from this virtual process was obtained from electron pairs having equal and opposite momenta, and energies within $\hbar\omega$ of E_F where ω is the frequency of the vibrational quanta. To observe the total energy condensation from the system, the interaction was extended to include many electron states whose momenta were near the Fermi momentum state k_F. This energy condensation from the Cooper pairs could then be used to estimate the thermal energy ($k_B T_c$) necessary to destroy this interacting state.

The condensed state can be shown by considering the wavefunction of the two electrons such that the center of gravity of the pair is at rest. This wavefunction is expanded for all

momentum states **k** such that[75]

$$\Psi(r_1-r_2) = \sum_{\mathbf{k}} g(k) \exp\big(i\mathbf{k}\cdot(r_1-r_2)\big) \qquad (3\text{-}1)$$

where g(k) is the probability amplitude for the pair to be in opposite momentum states **k, -k**. Since all states are occupied below k_F

$$g(k) = 0 \qquad \text{for } k < k_F. \qquad (3\text{-}2)$$

The Schrödinger equation for the pair is written

$$\frac{-\hbar^2}{2m}(\nabla_1^2 + \nabla_2^2)\Psi(r_1,r_2) + V(r_1,r_2)\Psi = \left(E + \frac{-\hbar^2 k_F^2}{m}\right)\Psi \qquad (3\text{-}3)$$

where E is the energy of the interacting pair relative to E_F.
Substituting (3-1) in (3-3), and defining the term

$$V_{k,k'} = \frac{1}{L^3}\int V(r)\exp\big(-i(k-k')\cdot r\big)dr \qquad (3\text{-}4)$$

where L^3 is the volume of the system, gives the equation

$$\frac{\hbar^2}{m}k^2 g(k) + \sum_{k'} g(k')V_{k,k'} = (E + 2E_F)g(k). \qquad (3\text{-}5)$$

Equation (3-5) is the Bethe-Goldstone equation for two electrons. The interaction term V is nonzero only in the region where the energy of the two electrons k_1 and k_2 follows $|E(k_1) - E(k_2)| < \hbar\omega$, where $\hbar\omega$ is the order of $k_B\Theta$ (Θ=the Debye temperature) for phonon mediation. To observe the effects of (3-5) for an attractive interaction, one can consider the interaction term $V_{k,k'}$ to be

$$V_{k,k'} = \frac{-V}{L^3} \qquad \text{for } E < (E_F + \hbar\omega) \qquad (3\text{-}6)$$

$$= 0 \qquad \text{otherwise.}$$

By substituting (3-6) into (3-5), one gets the self consistency equation

32

$$1 = \frac{V}{L^3} \sum_{k'} \left(-E + \frac{\hbar^2 k'^2}{m} - 2E_F \right)^{-1} \qquad (3-7)$$

for $E_F < \dfrac{\hbar^2 k'^2}{2m} < E_F + \hbar\omega$. By defining the energy range ξ' and the

density of states[75] per unit energy level $N(\xi')$,

$$\xi' = \frac{\hbar^2 k'^2}{2m} - E_F \quad \text{and} \quad N(\xi') = (2\pi)^{-3} 4\pi k'^2 \frac{dk'}{d\xi'} \qquad (3-8)$$

the summation in (3-7) can be replaced by an integration so that

$$1 = V \int_0^{\hbar\omega} N(\xi') \frac{1}{2\xi' - E} d\xi'. \qquad (3-9)$$

Assuming $\hbar\omega < E_F$, and $N(\xi')$ is approximately N_F, the density of

states at the Fermi surface, then

$$1 = \frac{1}{2} N_F V \ln\left(\frac{E - 2\hbar\omega}{E} \right), \qquad (3-10)$$

which for weak interactions ($N_F V \ll 1$) gives

$$E = \Delta = -2\hbar\omega \exp\left(\frac{-2}{VN_F} \right). \qquad (3-11)$$

E is the relative energy condensation from the Fermi energy and is

often defined as the condensation energy Δ as shown in (3-11).

Later from the BCS theory, this condensed state was shown to be

the superconducting state[76].

By comparing the thermal energy necessary to destroy the

condensed state with the condensation energy, (3-11) can be

rewritten in terms of T_C as

$$T_C = \frac{2\omega}{k_B} \exp\left(\frac{-2}{VN_F} \right). \qquad (3-12)$$

Equation (3-12) relates T_C with the physical characteristics of the

system: the density of superconducting carriers, the interaction

potential between the superconducting electrons and the frequency of the vibrational quanta. From (3-12) it is seen that a possible method of increasing T_c is by increasing the frequency of the vibrational quanta that mediate the superconducting electrons. In BCS theory these quanta are not specifically designated as being phonons. In fact, W. A. Little[13] and V. L. Ginzburg[14] suggested that the increase in T_c necessary to describe superconductivity near 100 °K might be achieved by electron interactions instead of phonons. They suggested that lower-dimensional electronic systems may induce such interactions and result in the increase of T_c. Another way to increase T_c is by increasing the density of superconducting charge carriers. Hirsch and Scalapino[15] have investigated the effects of T_c enhancement due to the presence of a Van Hove singularity near the Fermi energy for a quasi-two-dimensional electronic system. Z. Ye and H. Umezawa[77] have also investigated how inter-plane and intra-plane coupled superconductive systems can result in the increase of the density of states. Thus with the possibility of T_c enhancement occurring from the layered nature of these high T_c systems, it is important to investigate the effects of the layered electronic structure on the superconducting parameters in these systems.

London equations and the penetration depth

One of the first steps towards understanding the mechanisms of superconductivity came when F. and H. London[78,79] described

the electromagnetic properties of superconductivity using two equations,

$$E = \frac{\partial}{\partial t}(\Lambda J_s) \qquad (3\text{-}13)$$

and
$$h = -c \ \text{curl} \ (\Lambda J_s), \qquad (3\text{-}14)$$

where
$$\Lambda = \frac{4\pi\lambda_L^2}{c^2} = \frac{m}{n_s e^2}. \qquad (3\text{-}15)$$

The parameter n_s is the number of superconducting carriers in the system. Equation (3-13) describes perfect conductivity, since any electric field accelerates the superconducting electrons rather than simply sustaining their velocity against resistance. Equation (3-14), when combined with the Maxwell equation

$$\text{curl} \ h = \frac{4\pi J}{c} \qquad (3\text{-}16)$$

leads to
$$(\nabla^2 h) = \frac{h}{\lambda_L^2}, \qquad (3\text{-}17)$$

implying that the magnetic field damps exponentially into the superconductor with a length λ_L. Equation (3-14) describes the Meissner effect and introduces one of the characteristic lengths of superconductivity, the penetration depth, λ_L.

Pippard's nonlocal theory and the coherence length

In 1953 A. B. Pippard[80] stated that the change in λ with the addition of impurities could not be explained from London's equations, where λ was an intrinsic parameter. Pippard explained this by stating that London's equation (3-14) rewritten in the form,

$$J = \frac{-A}{\Lambda c} \qquad (3\text{-}18)$$

35

is only correct for the current and vector potential which vary slowly in space. If the vector potential changes within a correlation distance ξ_0, the current at a point will be affected by the vector potential at neighboring points within this distance, and (3-18) must be rewritten as

$$J = -\frac{3}{4\pi\xi_0\Lambda} \int \frac{r(r\cdot A)e^{-r/\xi}}{r^4} \, d\tau , \qquad (3-19)$$

where τ is the volume element containing A, r is the distance from τ to where J is being evaluated and ξ is related to ξ_0 and the mean free path, ℓ, by $\frac{1}{\xi} = \frac{1}{\xi_0} + \frac{1}{\ell}$. Equation (3-19) introduced the second characteristic length of superconductivity, the coherence length ξ_0. If $A(r)$ changed within the distance of ξ_0, there would be a weakening of the supercurrent response to the changing vector potential resulting in a larger λ.

From the uncertainty principle the coherence length ξ_0 can be related to the momentum range δp by

$$\xi_0 \delta p \sim \hbar. \qquad (3-20)$$

where $\hbar$ is Planck's constant. Only the electrons within $k_B T_c$ of the Fermi energy play a major role in the condensation so that $\delta p \sim (k_B T_c / v_F)$, where v_F is the Fermi velocity. Thus the value, ξ becomes

$$\xi_0 \sim \frac{\hbar v_F}{k_B T_c} . \qquad (3-21)$$

36

The Ginzburg Landau Theory

Even before the microscopic theory of superconductivity was formulated by Bardeen, Cooper and Schreiffer[76], Ginzburg and Landau[81] gave a macroscopic, phenomenological model of superconductivity near T_c. Their explanation was based on the fact that the superconducting phase transition is second order and the order parameter, which describes the ordered state, continuously changes through zero at T_c. Near T_c, the free energy of the superconducting state F_s, can be described in terms of the normal state free energy F_n, and the power series expansion of $|\psi|^2$ where ψ is the order parameter. In the absence of fields and gradients, this can be expressed as[82]

$$F_s = F_n + \alpha|\psi|^2 + \frac{\beta}{2}|\psi|^4 + \dots \qquad (3\text{-}22)$$

The most energetically favorable system can be found from the minimum free energy, where the derivative of (3-22) is set to zero. β is set to be positive so that the minimum free energy does not occur at $|\psi|^2 = \infty$. For $\alpha > 0$, the minimum free energy occurs only when $\psi = 0$, indicating that the system is in its normal state. For $\alpha < 0$, there is a non-trivial solution to (3-22) whose minimum occurs at

$$|\psi|^2 = \frac{-\alpha}{\beta} . \qquad (3\text{-}23)$$

During the superconducting transition, α goes from positive to negative, passing zero at T_c. Thus the free energy can be written

$$F_s = F_n - \frac{\alpha^2}{2\beta} . \qquad (3\text{-}24)$$

37

From the Gorter-Casmir[83] relation, where the free energy is written

$$F_n - F_s = -\frac{H_c^2(T)}{8\pi} , \qquad (3\text{-}25)$$

(3-24) can be written as

$$\frac{H_c^2(T)}{8\pi} = \frac{\alpha^2}{2\beta} . \qquad (3\text{-}26)$$

Near T_c, the temperature dependence of α and β are

$$\alpha(T) \sim (T\text{-}T_c) \{\frac{d\alpha}{dT}\}_{T=T_c} \quad \text{and} \quad \beta(T) \sim \beta(T_c) . \qquad (3\text{-}27)$$

Thus from GL theory, the temperature dependence of the critical field near T_c is approximately linear in T. At lower temperatures[84], where the GL equations become less valid, H_c saturates to follow $(T\text{-}T_c)^{1/2}$.

A spatially varying order parameter, due to gradients and fields, results in an additional $|\nabla\psi|^2$ term added to (3-22) so that

$$F_s = F_n + \alpha|\psi|^2 + \frac{\beta}{2}|\psi|^4 + \frac{1}{2m} \left| \left(-i\hbar\nabla - \frac{e^*A}{c} \right) \right| \psi^2 + \frac{H^2}{8\pi} , \qquad (3\text{-}28)$$

where $\frac{H^2}{8\pi}$ is the change in the normal state energy due to the presence of H. Minimizing (3-28) with respect to ψ and A leads to the formation of the two Ginzburg Landau (GL) equations

$$\frac{1}{2m^*}\left[-i\hbar\nabla - \frac{e^*A}{c} \right]^2 \psi + \alpha\psi + \beta|\psi|^2\psi = 0 \qquad (3\text{-}29)$$

and

$$\frac{curlH}{4\pi} = \frac{j}{c} = \frac{e^*h}{2im^*c} (\psi^*\nabla\psi - \psi\nabla\psi^*) - \frac{e^*}{m^*c^2} \psi^*\psi A . \qquad (3\text{-}30)$$

The two GL equations describe the most energetically favorable superconducting state of the system.

38

In zero field (A=0 and ψ is real), equation (3-29) is written in one dimension as

$$\frac{-\hbar^2}{2m^*|\alpha|}\frac{d^2f}{dx^2} + f - f^3 = 0 \qquad (3\text{-}31)$$

where f is the normalized order parameter $f = \frac{\psi}{\psi_o}$ and ψ_o is the full order parameter deep inside the superconductor ($\psi_o^2 = \alpha/\beta$). The first term in (3-31) gives the spatial dependence of the order parameter. Thus one could define a characteristic length ξ, where from (3-27)

$$\xi^2(T) = \frac{-\hbar^2}{2m^*|\alpha(T)|} \propto \frac{1}{T_c\text{-}T}. \qquad (3\text{-}32)$$

This characteristic length is often called the GL coherence length and is different from Pippard's nonlocal electrodynamic coherence length ξ_o. The GL coherence length, ξ, gives the length scale necessary for the superconducting order parameter to saturate. The relation of the two coherence lengths is often written as[75]

$$\xi(T) = 0.74\xi_o\left(\frac{T_c}{T_c\text{-}T}\right)^{1/2}. \qquad (3\text{-}33)$$

Near T_c, ξ diverges with increasing temperature. Physically this means that the system needs a larger distance before obtaining full order, until at T_c, ξ completely diverges.

The penetration depth, λ can be obtained by taking the curl of j, which from (3-30) gives

$$\text{curl} j = \frac{-e^*}{m^*c}|\psi|^2 h. \qquad (3\text{-}34)$$

Comparing (3-30) with (3-14) and (3-15), λ can be written

$$\lambda = \left[\frac{m^*c^2}{4\pi e^{*2}|\psi|^2}\right]^{1/2}, \qquad (3\text{-}35)$$

so that the superconducting electron density n_s is related to $|\psi|$ as $n_s=|\psi|^2$. The temperature dependence of λ comes from the temperature dependence of $|\psi|^2$ which from (3-23) and (3-27) gives

$$\lambda \propto (T_c - T)^{-1/2}. \qquad (3-36)$$

From BCS theory, the temperature dependence of λ actually follows $(T_c - T)^{-1/4}$ rather than (3-36)[84]. However, near T_c, where the GL theory should be valid, (3-36) describes the temperature dependence of λ quite well. As temperature nears T_c, the penetration depth diverges indicating the loss of the Meissner effect at $T=T_c$.

Though both characteristic lengths in the GL theory diverge near T_c, their ratio remains finite. This ratio, often used to characterize the superconductivity of a material, is defined as the GL parameter, κ where

$$\kappa = \frac{\lambda(T)}{\xi(T)}. \qquad (3-37)$$

From (3-23), (3-26), (3-32) and (3-35), κ can be written

$$\kappa = \frac{mc}{2e\hbar}\left(\frac{\beta}{2\pi}\right)^{1/2}. \qquad (3-38)$$

Far from T_c, where the GL equations break down, κ varies with temperature. However the change in κ throughout the whole temperature range is small[85]. So throughout the thesis, κ will be assumed to be independent of temperature.

If the order parameter, the spatial variable, vector potential and the internal field were written in terms of reduced variables;

40

$$\psi = \psi_0 f, \quad r = \lambda(T)\rho, \quad \frac{2e}{\hbar c}\xi(T)A = \mathcal{A}, \quad \frac{2e}{\hbar c}\xi(T)\lambda(T)h = \hbar, \quad (3\text{-}39)$$

then the GL equations can be written

$$-\frac{\nabla^2}{\kappa^2}f_0 + \frac{1}{f_0{}^3}(\text{curl}\,\hbar)^2 = f_0 - f_0{}^3 \qquad (3\text{-}40)$$

and

$$f_0{}^2\hbar = \frac{2}{f_0}\text{grad}f_0 \times \text{curl}\,\hbar - \text{curlcurl}\,\hbar. \qquad (3\text{-}41)$$

where f_0 is the amplitude of f, and $\hbar$ follows the Maxwell equation

$$\hbar = \text{curl}\mathcal{A}. \qquad (3\text{-}42)$$

Surface energy and Type II superconductivity

London initially introduced the concept of surface energy by noting that for a superconductor in the intermediate state, the exclusion of H in the superconducting regions requires an interface surface energy whose contribution is greater than the gain in energy from the diamagnetism[86]. The concept of surface energy was later used to understand the properties which affect the two types of superconductors (I and II). To qualitatively explain how surface energy differentiates the two types of superconductors, one must look at the energy contributions at a superconductor-to-normal interface, where the order parameter and the magnetic induction change. Since below T_C, the normal state is energetically higher than the superconducting state, there is an increase in the free energy within the coherence length. On the other hand, since it takes energy to keep the applied field out of the superconductor, there is a decrease in the free energy within the penetration depth. As the applied field increases, the energy decrease due to the

magnetic penetration increases in magnitude until it becomes relatively larger than the energy increase due to the change in ψ. At a field defined as H_{c1}, it becomes energetically favorable to create a vortex filament with a normal core and magnetic flux within the sample. This energy relation depends upon the relative size of λ and ξ, or the size of κ. As κ increases $(\lambda > \xi)$ the energy contribution from λ becomes greater than ξ and thus this vortex nucleation will become more probable and will occur at lower applied fields. Thus the type II nature of the superconductor depends upon the surface energies and the size of κ. A more quantitative explanation is given below.

For an infinite superconductor having the boundary conditions, $B = H_c$ and $\psi = 0$ at $z = -\infty$, and $B = 0$ and $\psi = \psi_0$ at $z = \infty$, assuming that both ψ and B in the sample varied continuously, the surface energy can be taken as the difference between the energy of the above system and one having full condensation energy everywhere which is given by the volume integral of $\dfrac{H_c^2}{8\pi}$. Also, the reduction of the magnetic energy due to the penetration of the field is taken into account, $MH_c = \dfrac{h - H_c}{4\pi} H_c$. Thus the surface energy is written as[86]

$$E = \int_{-\infty}^{\infty} dz \left\{ \alpha |\psi|^2 + \frac{\beta}{2} |\psi|^4 + \frac{1}{2m} \left| \left(-i\hbar\nabla - \frac{2eA}{c} \right) \psi \right|^2 \right.$$

$$\left. + \frac{h^2}{8\pi} - \frac{hH_c}{4\pi} H_c + \frac{H_c^2}{8\pi} \right\} \qquad (3\text{-}43)$$

or in reduced form, after much algebra, as

$$E = 2\lambda(T)\,\frac{H_c^2}{8\pi}\int_{-\infty}^{\infty}dz\left\{\frac{1}{2}(1-f^4) + h^2 - \sqrt{2}\,h\right\} = 2\lambda(T)\,\frac{H_c^2}{8\pi}\,I \quad (3\text{-}44)$$

where the boundary conditions are $f = 0$ at $z = -\infty$ and $\frac{df}{dz} = 0$ and f

$= 1$ for $z = \infty$. Whether the surface energy, E, will be negative or

positive depends on the sign of $I = \int_{-\infty}^{\infty}dz\left\{\frac{1}{2}(1-f^4) + h^2 - \sqrt{2}\,h\right\}$. The

surface energy can be made zero by taking $h = \frac{1}{\sqrt{2}}(1-f^2)$ so that

the two reduced GL equations $(3\text{-}40)$ and $(3\text{-}41)$ give

$$-\frac{1}{\kappa^2}\frac{d^2f}{dz^2} + \frac{2}{f}\left(\frac{df}{dz}\right)^2 = f - f^3 \quad (3\text{-}45)$$

and

$$-\frac{2}{\sqrt{2}}f\frac{d^2f}{dz^2} + \frac{2}{\sqrt{2}}\left(\frac{df}{dz}\right)^2 = \frac{2}{\sqrt{2}}(1-f^2) \quad (3\text{-}46)$$

where the correction $h = \frac{1}{\sqrt{2}}(1-f^2)$ has been used to eliminate the

variable h. The two GL equations have only a single unknown

function f, and are consistent with each other only if $\kappa = \frac{1}{\sqrt{2}}$. So

the energy is zero for $\kappa = \frac{1}{\sqrt{2}}$, and for $\kappa > \frac{1}{\sqrt{2}}$, I is found to be

negative, while for $\kappa < \frac{1}{\sqrt{2}}$, I is found to be positive[86]. Therefore, κ

$= \frac{1}{\sqrt{2}}$ separates the superconductors having positive and negative

surface energy, classified as type I and II respectively.

Since the condensation energy of the system can be

represented by the area under a magnetization curve, a

43

thermodynamic critical field H_c can be defined for a type II superconductor as the maximum field for a type 1 magnetization curve whose condensation energy is the same as that of the type II superconductor as shown in Figure 3-1 (b). Both H_{c1} and H_{c2} are intrinsic characteristic parameters of the system and depend upon both the strength of the condensation energy (represented by the thermodynamic critical field H_c) and the Ginzburg Landau parameter κ. For a larger value of H_c one will get larger H_{c1} and H_{c2}. On the other hand even with the same value of H_c, a larger κ system will have higher H_{c2} and lower H_{c1}. Since κ is determined by the two characteristic lengths λ and ξ, these values as well as the thermodynamic critical field can be obtained by finding the upper and lower critical fields of the system.

Upper Critical Field H_{c2}

Near H_{c2}, the superconducting order parameter is very small so that the higher order terms in the GL equations become negligible. Then the GL equations take on a linearized form of

$$\frac{1}{2\,m}\left[-i\hbar\nabla -\frac{2\,e}{c}\,A\,\right]^2 \psi = -\alpha\psi. \qquad (3-47)$$

Also, the second GL equation shows that the correction due to the supercurrents is of the order ψ^2 so that at small ψ, it can be ignored and to a first approximation $h = H$ so that

$$\nabla \times A = H. \qquad (3-48)$$

Equation (3-47) is in the form of Schrödinger's equation for the motion of charge 2e and mass m in a field. For such a system the

44

Figure 3-1

(a)

Type I
Superconductor

(b)

Type II
Superconductor

Figure 3-2

(a)

(b)
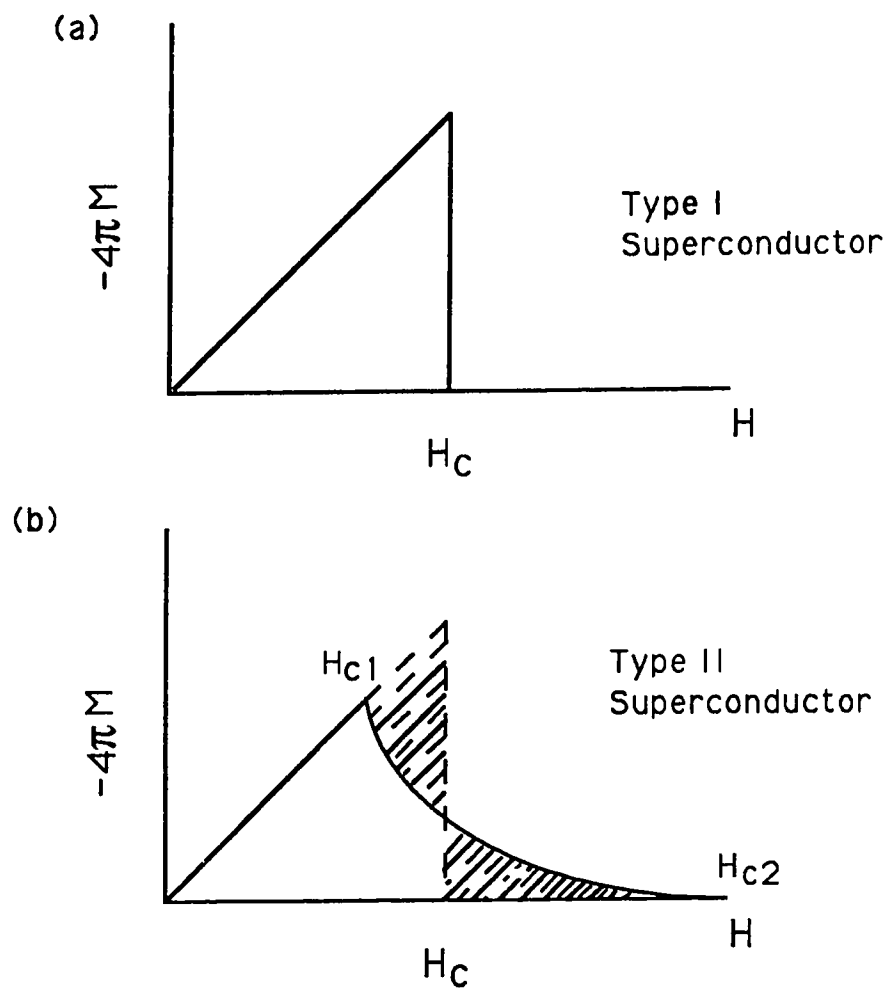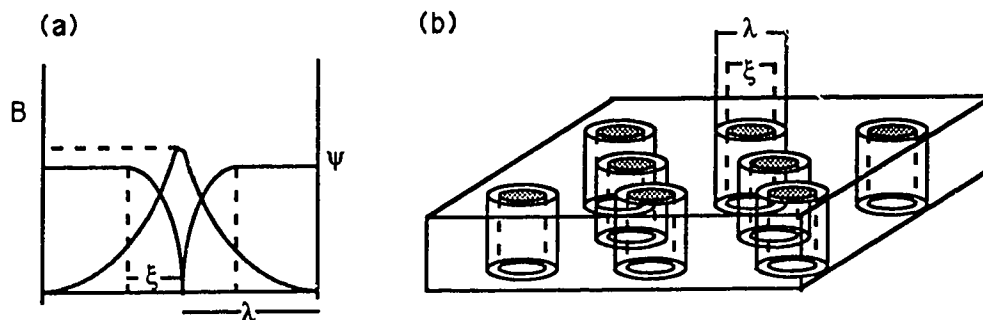
particle moves along the field direction H with an orbital motion

perpendicular to H, having a frequency

$$\omega = \frac{2eH}{mc}.$$
(3-49)

If $|\psi|$ is taken to be a bounded function, the eigenvalues of (3-47)

are

$$-\alpha_n = \frac{m v_z^2}{2} + \left(n + \frac{1}{2}\right)\hbar\omega.$$
(3-50)

Since we are observing the highest field where superconductivity

can exist, this corresponds to $n = 0$ and $v_z = 0$ so that from (3-49)

and (3-50)

$$H_{c2} = \frac{-\alpha m c}{\hbar e}.$$
(3-51)

From the GL equations (3-26) and (3-38) we find that

$$H_{c2} = \sqrt{2}\ \kappa\ H_c.$$
(3-52)

Assuming a constant κ, the temperature dependence of H_{c2} follows

the linear temperature dependence of H_c. From (3-26), (3-32),

(3-38) and (3-51), H_c and H_{c2} can be written

$$H_c = \left(\frac{ch}{2e}\right)\left(\frac{1}{2\pi\sqrt{2}\lambda\xi}\right) = \left(\frac{\Phi_0}{2\pi\sqrt{2}\lambda\xi}\right)$$
(3-53)

and

$$H_{c2} = \left(\frac{2e}{ch}\right)\left(\frac{1}{2\pi\xi^2}\right) = \left(\frac{\Phi_0}{2\pi\xi^2}\right)$$
(3-54)

where Φ_0 is the flux quantum $\Phi_0 = 2 \times 10^{-7}$ G cm^2 as shown in

Appendix I.

For a Type II superconductor between H_{c1} and H_{c2} (often

called the mixed state), the superconducting regions surround lines

of flux (where field penetrates) and form multi-connected

46

filaments. In the vortex structure, each filament consists of a core having radius approximately equal to the coherence length and screens out the field for distances greater than the penetration depth, as shown in Figure 3-2 (a). Since the filaments experience a Lorentz force, they position themselves in a lattice formation to obtain the lowest free energy, as shown in Figure 3-2 (b). From GL equations near H_{c2}, each filament is found to contain one flux quantum for any κ. This is also true near H_{c1} for an isolated filament. Thus one can assume that the filaments contain one flux quantum each throughout the entire range of the mixed state[87]. Thus as field is increased in the mixed state the total flux contained in the vortex filament remains the same and it is the density of filaments in the material that increases.

The Lower Critical Field H_{c1}

The lower critical field, H_{c1} is identified as the field where the first vortex filament nucleates in the system and is determined from the net energy of the system. H_{c1} occurs when it is energetically favorable to create a vortex having a normal core and a field, compared to remaining completely superconducting and diamagnetic. To find H_{c1}, the free energy can be calculated such that the system has the same energy whether a flux line is created in the system or not. The free energy expression for this relation is written

$$F_s = F_s + \varepsilon_1 L - \frac{H_{c1} \int h dr}{4\pi} \qquad (3\text{-}55)$$

where L is the length of the vortex line in the sample. The second term in the right hand side represents the energy of creating the vortex where ε_1 is the vortex line energy per unit length. The third term gives the decrease in the energy due to the field penetration. Since at H_{c1}, the creation of the first vortex is assumed, equation (3-55) is rewritten

$$F_s = F_s + \varepsilon_1 L - \left(\frac{H_{c1}\Phi_o L}{4\pi} \right) \tag{3-56}$$

or

$$H_{c1} = \frac{\varepsilon_1 4\pi}{\Phi_o} . \tag{3-57}$$

By finding ε_1 one can find the expression for H_{c1}. For a system with large κ, since ξ can be assumed to be small, the core contributions to ε_1 is often ignored[75]. Th n the contributions to the vort line energy comes from the field energy and the kinetic energy currents and can be written

$$\varepsilon_1 = \frac{1}{8\pi} \int (h^2 + \lambda^2 |curlh|^2) dS \tag{3-58}$$

or by using a vector identity and the divergence theorem,

$$\varepsilon_1 = \frac{1}{8\pi} \int (h + \lambda^2 curlcurlh) \cdot hdS + \frac{\lambda^2}{8\pi} \oint (h \times curlh) \cdot ds. \tag{3-59}$$

For the region outside the core where we are looking, London's equation (3-14) combined with the Maxwell equations gives

$$\lambda^2 \ curlcurlh + h = 0 \tag{3-60}$$

and states that the first integral in (3-59) can be ignored[79]. The second integral is taken over the surface of the core of radius ξ and the gives a solution

$$\varepsilon_1 = \frac{\lambda^2}{8\pi} 2\pi\xi \ h(\xi) \ |curlh(\xi)| = \frac{\lambda^2}{8\pi} 2\pi\xi \ h(\xi) \frac{dh}{dr} . \tag{3-61}$$

To find the expression for h, one can state that within the core, one can rewrite (3-60) to take account of the presence of the core by inserting a two dimensional delta function $\delta(r)$ such that

$$\lambda^2 \text{ curlcurl} h + h = \Phi_0 \delta(r). \qquad (3-62)$$

The solution to (3-62) within the region $\xi \ll r \ll \lambda$ is

$$h(r) \sim \frac{\Phi_0}{2\pi\lambda^2} \left\{ \ln\frac{\lambda}{r} + \text{const} \right\}. \qquad (3-63)$$

Equation (3-63) and (3-61) can be combined to give the line energy per unit length,

$$\varepsilon_1 = \left(\frac{\Phi_0}{4\pi\lambda}\right)^2 \ln\kappa. \qquad (3-64)$$

Equation (3-64) gives the energy for creating a vortex line, which when combined with (3-57), gives the expression for H_{c1} as

$$H_{c1} \quad \left(\frac{\Phi_0}{4\pi\lambda^2}\right) \ln\kappa \qquad (3-65)$$

or

$$H_{c1} \sim \frac{H_c}{\sqrt{2}\kappa} \ln\kappa. \qquad (3-66)$$

Equations (3-65) and (3-66) express the lower critical fields in terms of the characteristic parameters, H_c, λ, Φ_0, and κ. Equation (3-65) gives the strong relationship between H_{c1} and λ. As λ increases H_{c1} is found to decrease. This makes sense since the larger the penetration depth the more negative the surface energy. Also from (3-66) a direct relationship between H_c and H_{c1} is seen, where a change in H_c will lead directly to a change in H_{c1}.

Part II: Anisotropic superconductivity

Before the high T_c superconductors, some of the low T_c superconductors such as niobium were found to be slightly

49

anisotropic[88-90]. Further, the existence of layered superconductors such as transition metal dichalcogenides[91-93], made necessary the analysis of anisotropic superconductivity long before the discovery of high T_C superconductors. Thus the anisotropic theories that were developed for these systems can be used to analyze the anisotropy in the high T_C superconductors.

Both the anisotropy in the superconducting order parameter as well as in the non-superconducting, normal state parameters can affect the superconducting properties. Anisotropy of the order parameter can result from anisotropy of the variables found in equation (3-11), as well as from non-phonon superconducting interactions having directional dependence in the coupling parameter. Exotic, non-phonon coupling, often associated with non-singlet pairing, has been considered in materials such as the heavy fermion superconductors[94-96]. Examples of anisotropic normal state parameters include the anisotropy in the electronic structure[90] of the material as well as the localization of the superconductivity to certain regions within the material[93]. Even with an isotropic order parameter, anisotropic superconductivity may arise from the anisotropy in the normal state parameters. Since high T_C superconductors seem to be affected by the anisotropy of the normal state electronic structure, the analysis in this chapter will be focused on the anisotropy stemming from these normal state characteristics. This does not mean anisotropy in the order parameter does not exist in the high T_C systems, but that since there is as yet no strong evidence supporting such a

phenomenon, such a complex analysis will not be covered in the thesis.

Two methods commonly used to analyze anisotropic superconductivity arising from the normal state electronic anisotropy are the anisotropic Ginzburg-Landau model[97] and the Lawrence-Doniach (LD) model[98,99]. The anisotropic GL theory[97] considers the anisotropy of the superconductivity to arise from the anisotropy in the electronic effective mass. This analysis is useful for systems having an anisotropic electronic structure but where the superconductivity exists throughout the bulk of the sample. Lawrence and Doniach[98,99], analyzed the standard GL theory for a system which localized the superconductivity to discrete two dimensional layers with Josephson coupling between the layers. This analysis is useful for materials having strongly localized two dimensional behavior in the superconductivity. The anisotropic GL theory is often described as a three dimensional (3D) anisotropic model while the LD theory is often denoted as a coupled two dimensional (2D) model. Since each method of analysis is very extensive, it is difficult to cover both models within the context of this thesis. The experimental results of this thesis will be analyzed using the anisotropic GL theory.

Anisotropic Ginzburg-Landau Theory

Soon after Ginzburg and Landau calculated their macroscopic model for superconductivity, Ginzburg[97] extended the theory to consider the effect of electronic anisotropy on the superconducting

parameters. He stated that any anisotropy in the effective mass of the charge carriers will affect the GL equations and their corresponding characteristic parameters. To investigate this effect, Ginzburg replaced the effective mass scalar, m, in the GL free energy (3-28) with a 3x3 mass tensor m_{ij} so that

$$F_s-F_n = \sum_{ij} \frac{1}{2m_{ij}}\left(-i\hbar\frac{d}{dx_i}\psi - \frac{2e}{c}A_i\psi\right)\left(i\hbar\frac{d}{dx_j}\psi* - \frac{2e}{c}A_j\psi*\right)$$
$$+ \alpha|\psi|^2 + \frac{1}{2}\beta|\psi|^4 + \frac{H^2}{8\pi}, \qquad (3-67)$$

which when minimized with respect to $\psi*$ gives

$$\sum_{ij} \frac{1}{2m_{ij}}\left(-i\hbar\frac{d}{dx_i} - \frac{2e}{c}A_i\right)\left(i\hbar\frac{d}{dx_j} - \frac{2e}{c}A_j\right)\psi + \alpha\psi + \beta\psi|\psi|^2 = 0. \qquad (3-68)$$

Later Tilley[88] found this effective mass anisotropy to have an effect on the upper critical field, resulting in anisotropic H_{c2} values for niobium. For a field applied along one of the principal directions of the crystal, H_{c2} was found to depend on the effective mass such that

$$H_{c2} = \frac{c|\alpha|}{e\hbar} (m_1m_2)^{1/2}, \qquad (3-69)$$

where m_1 and m_2 are the principal values of the components of m_{ij}, orthogonal to the applied field. Tilley also analyzed[100] the solution to equation (3-68), for the region just below H_{c2}, where the linearized GL equations apply. If the effective mass tensor defines an ellipsoid with the principal tensor axes being along the principal crystal axes. then one can assume the non-diagonal terms, $1/m_{ij}$ to be zero[100]. By considering the field to be along the third axis such that the vector potential is taken along the second

axis with a magnitude of $H_0 x_1$, then the general solution to the anisotropic GL equations can be written

$$\Psi = \sum_{n=-\infty}^{\infty} C_n \exp(inkx_2)\, \psi_n(x_1) , \qquad (3-70)$$

$$\psi_n(x_1) = \exp\left\{-\left(\frac{1}{2}v-i\omega\right)\left(x-\frac{n\hbar c k}{2eH_0}\right)^2\right\}$$

where $1/m_{12} = 1/m_{21} = 0$ and $A = H_0 x_1 \hat{e}_2$. The condensation energy can be written

$$F_s-F_n = \alpha|\psi|^2 + \frac{1}{2}\beta|\psi|^4 + \frac{1}{2m_1}\left|-i\hbar\frac{d\psi}{dx_1}\right|^2 \qquad (3-71)$$

$$+\frac{1}{2m_2}\left|\left(-i\hbar\frac{d}{dx_2} - \frac{2}{c}\frac{e}{c}H_0 x_1\right)\psi\right|^2$$

which when minimized with respect to ψ gives

$$\frac{\hbar^2}{2m_1}\left(\frac{d^2\psi}{dx_1^2}\right)+\frac{1}{2m_2}\left(\hbar\frac{d}{dx_2} - \left(\frac{2ie}{c}\right)H_0 x_1\right)^2\psi$$

$$+ |\alpha|\psi - \beta|\psi|^2\psi = 0. \qquad (3-72)$$

By rescaling the spatial variable x_2 by the effective mass ratio so that

$$x_2 = \left(\frac{m_1}{m_2}\right)^{1/2} x_2' , \qquad (3-73)$$

equations (3-71) and (3-72) can be rewritten as

$$F_s-F_n = \alpha|\psi|^2 + \frac{1}{2}\beta|\psi|^4 +\frac{1}{2m_1}\left|-i\hbar\frac{d^2\psi}{dx_1^2}\right|^2 \qquad (3-74)$$

$$+\frac{1}{2m_1}\left|\left(-i\hbar\left(\frac{d}{dx_2'}\right) - \left(\frac{2e'}{c}\right)H_0 x_1\right)\psi\right|^2$$

and

$$\frac{1}{2m_1}\frac{d^2\psi}{dx_1^2} + \frac{1}{2m_1}\left(\hbar\frac{d}{dx_2'} - \left(\frac{2ie'}{c}\right)H_0 x_1\right)^2\psi + |\alpha|\psi - \beta|\psi|^2\psi = 0, \quad (3-75)$$

53

where $e' = (m_1/m_2)^{1/2} e$. Equations (3-74) and (3-75) are now in the same form as their corresponding isotropic GL equations. This is quite significant since it states that the basic difference between the isotropic and the anisotropic GL equations is that the scalar magnitude of the anisotropic coordinate is corrected by the effective mass ratio, as given by (3-73). Since only the length scale of the coordinate in the GL equations changes due to an anisotropic effective mass, all the parameters that are independent of the coordinate, (such as T_c and H_c) will remain unchanged, while all spatially dependent parameters (such as λ and ξ) will be modified by the effective mass ratio.

Tilley further stated[100] that the only place where the GL free energy depends on m and e is in the gradient term in the equation (3-28). The characteristics of the gradient term in the GL equations can be described by the two characteristic lengths, ξ and λ. Thus the anisotropy in the effective mass can be expressed by these two lengths or more simply, by their ratio κ[100]. So for an anisotropic superconductor, where the field is perpendicular to m_1 and m_2, κ from equation (3-38) can be written[101]

$$\kappa = \frac{m_1 c}{2e'\hbar}\left(\frac{\beta}{2\pi}\right)^{1/2} = \frac{(m_1 m_2)^{1/2}}{2e\hbar}\left(\frac{\beta}{2\pi}\right)^{1/2}. \quad (3-76)$$

In terms of the characteristic lengths, κ is written

$$\kappa = \left(\frac{\lambda_1 \lambda_2}{\xi_1 \xi_2}\right)^{1/2}, \quad (3-77)$$

where λ_i and ξ_i represent the characteristic lengths from the superconducting charge carriers whose effective mass is given by m_i in equations (3-35) and (3-32) respectively.

54

Since the high T_C superconductors, in general, have uniaxial symmetry, the anisotropic GL theory will be considered for an uniaxial system. For such a system, the effective mass along two of the principal axes will be equal, while for the third axis, it will be different ($m_1 = m_2 \neq m_3$). Transport measurements on high T_C systems, which found the resistivity in the c direction to be much higher than the resistivity in the a,b plane, indicate that $m_c \gg m_a$, m_b. Thus equation (3-77) becomes,

$$\kappa^c = \frac{\lambda^c_{a,b}}{\xi_{a,b}} \quad \text{and} \quad \kappa^{a,b} = \left(\frac{\lambda^{a,b}_{b,a}\lambda^{a,b}_c}{\xi_{b,a}\,\xi_c} \right)^{1/2} , \quad (3\text{-}78)$$

where the superscript denotes the field direction and the subscript denotes the direction of λ or ξ in which λ or ξ measures the variation of H or ψ. Since all the mass anisotropy is incorporated into κ, both the relationship between H_{c2} and H_c given by (3-52), and the relation between H_{c1} and H_c given by (3-66) still holds, but where κ is now represented by κ^i in (3-78) so that

$$H_{c2}^i = \sqrt{2}\,\kappa^i\,H_c \quad \text{and} \quad H_{c1}^i \sim \frac{H_c}{\sqrt{2}\kappa^i}\,\ln\kappa^i . \quad (3\text{-}79)$$

To represent (3-79) in terms of the characteristic lengths, equations (3-54) and (3-65) can be rewritten into the anisotropic forms[91,92,102]

$$H_{c2}^c = \frac{\Phi_0}{2\pi\xi_{a,b}^2} , \quad H_{c2}^{a,b} = \frac{\Phi_0}{2\pi\xi_{a,b}\xi_c} \quad (3\text{-}80)$$

and

$$H_{c1}^c \sim \left(\frac{\Phi_0}{4\pi\lambda^c_{a,b}{}^2} \right)\ln\kappa^c , \quad H_{c1}^{a,b} \sim \left(\frac{\Phi_0}{4\pi\lambda^{a,b}_{b,a}\lambda^c_{b,a}} \right)\ln\kappa^{a,b}. \quad (3\text{-}81)$$

55

From equation (3-79), since the anisotropic term in H_{c2} and H_{c1} comes from κ^i given by (3-76), the anisotropic ratio in H_{c2} and H_{c1} can be written in terms of the effective mass anisotropy[65],

$$\frac{H_{c2}^c}{H_{c2}^{a,b}} = \left(\frac{m_{a,b}}{m_c}\right)^{1/2} , \qquad \frac{H_{c1}^c}{H_{c1}^{a,b}} = \left(\frac{m_c}{m_{a,b}}\right)^{1/2} \frac{\ln\kappa^c}{\ln\kappa^{a,b}} \qquad (3-82)$$

where

$$\frac{\kappa^c}{\kappa^{a,b}} = \left(\frac{m_{a,b}}{m_c}\right)^{1/2} . \qquad (3-83)$$

From the equations (3-32), a change in the effective mass is found to affect the coherence length by $(m^*)^{-1/2}$ such that ξ decreases with an increasing m^*, resulting in a larger H_{c2}. For the high T_c systems, since $m_c \gg m_{a,b}$, ξ_c is expected to be smaller than $\xi_{a,b}$ and from (3-80), H_{c2}^c should be smaller than $H_{c2}^{a,b}$. Similarly, a change in the effective mass is found to affect the penetration depth by $(m^*)^{1/2}$ so that λ increases with increasing m^*. The relative anisotropy of the penetration depth is quite complicated, since it depends upon both the field and supercurrent orientation with respect to the anisotropic axis. The anisotropy of the magnetic penetration depth can be analyzed using the anisotropic London equations, as will be discussed in the next section.

Anisotropic London Equations

The effect of uniaxial anisotropy on the magnetic penetration depth was analyzed by Kogan[103], as well as by Balatskiĭ, Burlachov and Gor'kov[104], who calculated how anisotropy affected the London equation (3-14). These calculations are found to be useful in understanding the magnetic properties for the anisotropic high T_c

superconductors[22]. Both models considered the GL equation (3-30) in the form

$$j_i = \frac{e^*}{m^*} |\psi|^2 \left(\hbar \nabla \phi - \frac{e^*}{c} A \right) = \frac{e^* n_s}{m^*} \left(\hbar \nabla \phi - \frac{e^*}{c} A \right) \qquad (3\text{-}84)$$

where ϕ is the phase of the superconducting order parameter. Since Kogan[103] based his analysis on the effects of the anisotropic GL equations on the London penetration depth, his anisotropic parameter was defined as the effective mass, $m = m_{ij}$. Balatskiǐ et al.[104] on the other hand were analyzing the anisotropic London equations for the heavy fermion systems having an anisotropic order parameter, and thus they defined their anisotropic parameter as the density of superelectrons, $n = n_{ij}$. Using the London equation (3-14) and (3-15) with Maxwell's equation (3-16), Kogan rewrote equation (3-17) into the form

$$h + \left(\frac{c^2}{n_s 4\pi e^{*2}} \right) \nabla \times (m_{ij} \nabla \times h) = 0 \qquad (3\text{-}85)$$

while Balatskiǐ et al. wrote it as

$$h + \left(\frac{m^* c^2}{4\pi e^{*2}} \right) \nabla \times (n_{s_{ij}}^{-1} \nabla \times h) = 0 \qquad (3\text{-}86)$$

where m_{ij} and $n_{s_{ij}}$ are the anisotropic forms of the effective mass and the superelectron density respectively. Though the basic cause of the anisotropy in Kogan's and Balatskiǐ et al.'s models is different, the resulting mathematical forms of (3-85) and (3-86) are the same. Since the anisotropic GL equations have been used extensively for this thesis, the anisotropic London's equations will be calculated using the effective mass as the anisotropic parameter as in equation (3-85).

For the high T_c systems, having uniaxial anisotropy where $m_c \gg m_{a,b}$, by assuming the anisotropic axis to be along the third direction, the mass tensor can be written $m_1=m_2 = m_{a,b} < m_3 = m_c$. Two specific cases can now be considered: firstly where the field is oriented along the c direction and secondly, where the field is oriented in the a,b plane. For the first case, since the field can be written $h = h\hat{e}_3$, one can write the curl of h as

$$\nabla \times h = \left(\frac{dh}{dy}\hat{e}_1 , -\frac{dh}{dx}\hat{e}_2\right). \qquad (3-87)$$

The change in the internal field will occur in the x,y plane so that

$$\nabla \times (m_i \nabla \times h) = \left(-\frac{d^2h}{dx^2} - \frac{d^2h}{dy^2}\right) m_{a,b} \hat{e}_3 = 0 , \qquad (3-88)$$

or from (3-85)

$$h + \left(\frac{c^2}{n_s 4\pi e*^2}\right)\left(-\frac{d^2h}{dx^2} - \frac{d^2h}{dy^2}\right) m_{a,b} \hat{e}_3 = 0. \qquad (3-89)$$

Equation (3-89) is a two-dimensional, second-order differential equation representing the field change in the x,y or a,b plane. From symmetry, the two dimensional equation can be separated into two, one-dimensional equations. Along the x axis, equation (3-89) becomes

$$h(x) + \left(\frac{c^2}{n_s 4\pi e*^2}\right)\left(-\frac{d^2h}{dy^2}\right) m_{a,b} \hat{e}_3 = 0 , \qquad (3-90)$$

for which the solution is of the form

$$h(x) = h_o e^{-\sqrt{A}x} , \qquad A = \frac{n_s 4\pi e*^2}{m_{a,b}c^2} . \qquad (3-91)$$

Due to uniaxial symmetry, when H is along the uniaxial axis (z or c axis), the field change along the y axis will be the same as (3-91)

such that

$$h(y) = h_o \, e^{-\sqrt{A}\,y}. \qquad (3\text{-}92)$$

As the field penetrates into the superconductor, it is dampened exponentially with a penetration depth of

$$\lambda^c_{a,b} = \left(\frac{m_{a,b}c^2}{n_s 4\pi e^{*2}}\right)^{1/2} , \qquad (3\text{-}93)$$

along x,y or a,b. Thus when the field is along the anisotropic axis, the penetration depth is axially symmetric and is found to be similar to that of an isotropic superconductor.

When the field is applied in the a,b plane, by assuming the field is along the x or a axis, the field can be written as $h = h\hat{e}_1$, so that the curl of h becomes

$$\nabla \times h = (\frac{dh}{dz}\hat{e}_2 , -\frac{dh}{dy}\hat{e}_3). \qquad (3\text{-}94)$$

For this field orientation, the change in the internal field will occur in the y,z plane such that (3-85) becomes

$$h + \left(\frac{c^2}{n_s 4\pi e^{*2}}\right)\left(- m_c\frac{d^2h}{dy^2} - m_{a,b}\frac{d^2h}{dz^2}\right)\hat{e}_3 = 0. \quad (3\text{-}95)$$

Equation (3-95) like (3-89) is a two-dimensional, second-order differential equation. Dividing (3-95) into y-and z-dependent parts gives the two solutions

$$h(y) = h_o \, e^{-\sqrt{B}\,y} , \qquad B = \frac{n_s 4\pi e^{*2}}{m_c c^2} \qquad (3\text{-}96)$$

and $\qquad h(z) = h_o \, e^{-\sqrt{A}\,z} , \qquad A = \frac{n_s 4\pi e^{*2}}{m_{a,b} c^2} . \qquad (3\text{-}97)$

From (3-97), the penetration depth along the z or c axis is found to

59

be the same as (3-93),

$$\lambda_c^{a,b} = \lambda_{a,b}^c \qquad (3-98)$$

while from (3-96) the penetration depth along y is given by

$$\lambda_{b,a}^{a,b} = \left(\frac{m_c c^2}{n_s 4\pi e^{*2}}\right)^{1/2} . \qquad (3-99)$$

So when the field is oriented perpendicular to the anisotropic axis (z or c axis), it is the penetration depth *orthogonal* to this axis and the field that is anisotropic. This is because the penetration of the field depends upon *the current running orthogonal* to it, and since the current along the c or z axis is the anisotropic current, it is the penetration along the a,b or x,y plane that is anisotropic and is of the form (3-99). For the high T_c superconductors, since $m_c > m_{a,b}$, the penetration from (3-99) should be bigger than the penetration from (3-93).

There are several interesting effects that arise from the effective mass anisotropy. Firstly, the characteristic lengths become anisotropic due to the anisotropy of the supercurrent effective mass. Furthermore, anisotropic characteristic lengths will affect the shape of the vortex line in the mixed state, making their cross section ellipsoidal[100] in shape. Finally V. G. Kogan[103] as well as Balatskiĭ, Burlachkov and Gor'kov[104] found that since there is a hard and an easy axis for the supercurrent flow, when a field greater than $H_{c1}(T)$ is applied at some angle to the anisotropic axis, the vortex will not align in the same direction as the applied field. This results in the appearance of a transverse magnetic moment

for such field orientations. As these consequences arising from the mass anisotropy are complex problems, they will only be discussed in the following chapters if they relate to the experimental discussions.

Part III: Critical State in Superconductivity

Until now, the discussions have been primarily centered around the intrinsic properties that characterize an ideal type II superconductor. However non-intrinsic characteristics such as the existence of impurities, defects and inhomogeneities may affect the superconducting properties as well. Defects and impurities, in general, tend to decrease the order parameter in the regions around them. Thus it is understandable that with enough defects and impurities, the superconducting phase can be degraded or even destroyed[105,106]. However, even a small fraction of defects will still affect the magnetic properties of the superconductor.

One such effect is the influence of defects and impurities on the mixed state of a type II superconductor, resulting in an irreversible magnetization. In other words, once the superconductor is in the mixed state, the magnetization will not retrace itself when the applied field and/or the temperature is changed and returned. This hysteretic behavior is often said to come from an attractive interaction of the vortices with the defect sites that prevents the movement of the vortices, even in the presence of a non-equilibrium field distribution or an induced current. Superconducting materials having this behavior were

often called "hard" superconductors. The dynamics of this condition are given by the critical state as will be discussed.

Anderson Model and Flux Pinning

In 1962, Anderson introduced a microscopic description of the effect of defects on the dynamics of flux vortices[107]. Anderson states that the defect sites are generally regions where the condensation energy is lower than in the pure material, such that they would act as free energy barriers for a vortex line. In other words, since there is an increase in energy with the creation of a normal core within the vortex, it is energetically favorable for the vortex core to be situated at a region already having a smaller energy condensation. Thus defect sites act as potential wells or barriers on the vortex lines and pin them in place. The magnitude of the potential well (i.e. the pinning energy) can basically be written as

$$F_p = (F_n - F_s) \, d^3 = \left(\frac{H_c^2}{8\pi} \right) d^3 \, , \qquad (3\text{-}100)$$

where d^3 is the volume of the vortex interacting with the pinning site. Equation (3-100) may be considered to give the maximum amount of energy that the pinning site may induce on a vortex. More commonly, the pinning energy will be some fraction of the above energy and is given as

$$F_p = p \left(\frac{H_c^2}{8\pi} \right) d^3 \, , \qquad (3\text{-}101)$$

where p < 1. The magnitude of p will depend upon several factors including the amount of decrease in the condensation energy at the pinning site, as well as the relative size of the pinning site with respect to the vortex. This pinning energy is often written as U_0 in some of the more recent studies flux pinning[28].

The consequence of these pinning sites is that they trap vortices that enter them, leading to a non-uniform flux distribution within the superconductor. It is only when a Lorentz force, greater than the pinning force, is exerted on the vortex that it will become depinned and free itself from the pinning site[79]. This condition, often called the critical state, is described by the condition

$$f_p(r) = f_L(r), \qquad (3-102)$$

where f is the force exerted on a vortex located at the position r. The standard Lorentz force equation for a current and a field

$$F = J \times \frac{B}{c} \qquad (3-103)$$

can be written for vortex as

$$f = j \times \frac{\Phi_0}{c}, \qquad (3-104)$$

where f is the force on a single vortex[79] j is the current density and Φ_0 is the flux quantum. This force, if not opposed by a pinning force would move the vortex line transverse to the field. Such a movement of the vortices would induce an electric field,

$$E = B \times \frac{v}{c}, \qquad (3-105)$$

where v is the velocity of the travelling vortex. The presence of the electric field results in a power dissipation even when the material is in its superconductive state.

63

This Lorentz force occurs in two ways, one from a current and the other from a non-uniform field distribution within the sample. In the first case, if the local field produced from an applied current, as described by Ampere's law, is lower than H_{c1}, the current and associated fields will be in the penetration layer at the surface of the superconductor due to the Meissner effect. However when the local field becomes greater than H_{c1}, part of the magnetic field will enter the bulk in the form of vortices. A Lorentz force will act on the vortices such that they will move towards the current and eventually annihilate in the center[75,86]. Thus for an ideal, type II superconductor, any current greater than H_{c1} would result in a power dissipation. However, if the current was applied to a superconductor containing flux pinning sites, the current must become large enough that the Lorentz force becomes greater than the pinning force in order to make them move. This depinning current is often called the critical state critical current and depends upon non-intrinsic properties, such as the density of defects in the material.

The second case, where a non-uniform field distribution creates a Lorentz force, occurs only if there are pinning s in the superconductor. When a magnetic field that is greater than $H_{c1}(T)$ is applied to a superconductor, magnetic vortex lines will begin to nucleate, enter the sample and try to form a uniform lattice structure. However, existing flux pinning sites will prevent the vortices from moving into the sample, resulting in the accumulation of pinned vortices in the outer region of the

64

superconductor. This in turn creates a field gradient due to the non-uniform flux distribution in the material. From Maxwell's equation (3-16), the field gradient can be related to the currents travelling around the bulk of the superconductor. The interaction of this current with the vortex field produces a Lorentz force on the vortices directed into the center of the superconductor. When the Lorentz force is large enough (i.e. the field gradient is sharp enough) to satisfy equation (3-102), the vortices will overcome the pinning barrier and enter the sample until the Lorentz force is once again lower than the pinning force. Thus a field greater than H_{c1}, applied to a hard superconductor will result in the creation of a negative field gradient penetrating into the sample. The size of this field gradient will give the critical state critical current necessary to satisfy the critical state equation (3-102).

The critical currents obtained in the two cases are related to each other, since they both must satisfy the critical state equation (3-102). For application purposes, flux pinning plays a very important role since with higher pinning energies, higher currents can be applied to the superconductor without experiencing energy losses. Thus many of the preliminary studies on the critical state[29,107-109] were done before the discovery of the high T_c superconductors, to understand the magnetic behavior of hard superconducting materials such as Nb-Zr and Nb-Sn.

Bean Model of the Critical State

One of the first analyses done to describe the magnetic behavior resulting from the critical state was the Bean critical state model[29,108]. Bean assumed the pinning energy, (3-101) of the critical state to be independent of applied magnetic field, in which case the pinning force will be constant for any local internal field within the superconductor. Thus the Lorentz force necessary to overcome the pinning force will also be independent of the local internal field. In this model, a linear field gradient into the superconductor is considered such that the critical state critical current, j_c has a constant value.

By considering an infinite cylindrical superconductor where the field is oriented along the length of the cylinder, the three dimensional Maxwell's equations can be reduced to one dimension due to radial symmetry and the independence of any quantity along z. If the sample was cooled in zer field to a temperature below T_c and a field much greater than $H_{c1}(T)$ was applied, the flux lines would enter and distribute themselves to satisfy the critical state equation (3-102). Since the Bean model assumes a field-independent pinning energy, the field profile along the radius of the cylinder would be linear as shown in Figure 3-3(a). The magnetic induction describing the amount of flux that has entered the material is represented by the shaded region below the field gradient line shown in Figure 3-3(a), while the diamagnetic region is represented by the unshaded portion above the field gradient line. As the applied field increases, the diamagnetic portion will

Figure 3-3

(a)

(b)

(c)
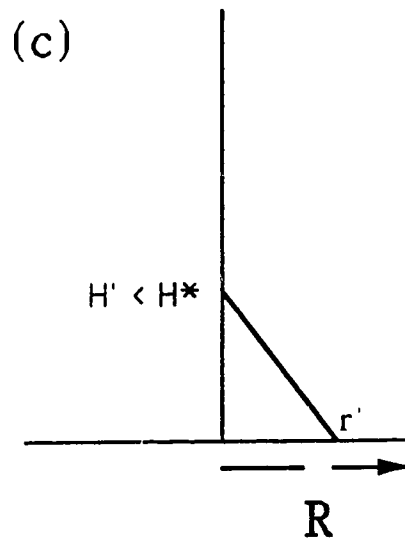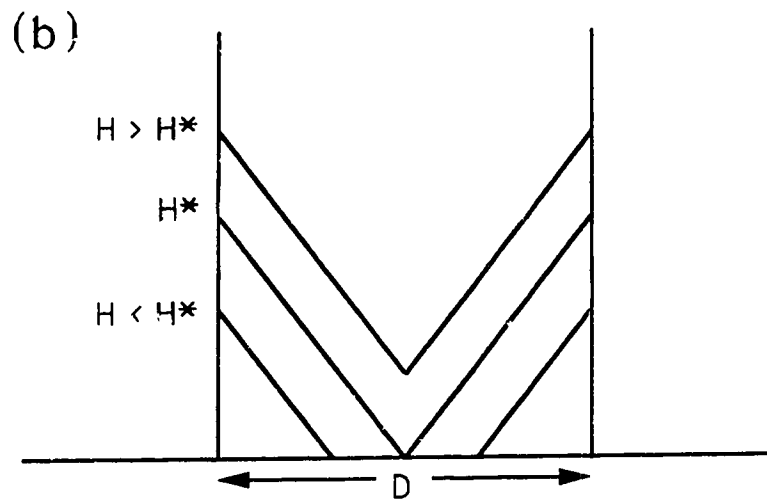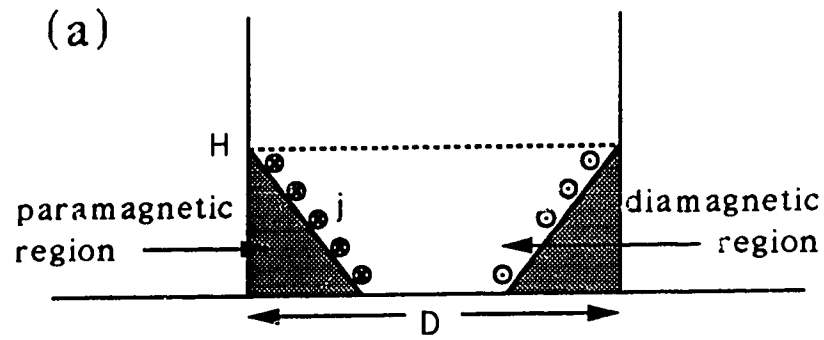
decrease as shown in Figure 3-3(b) until at a certain applied field, H*, the flux has fully penetrated the sample. For fields above H*, the amount of diamagnetism does not change with increasing H, as shown in Figure 3-3(b).

Bean analyzed the magnetization effect for the above model by calculating the average internal magnetic induction using the equation

$$B = \frac{\int \mathcal{H} dv}{\int dv}, \quad (3-106)$$

where $\mathcal{H}$ is the local magnetic field in the superconductor. The linear field profile assumed by the Bean Model simplifies the geometry of the integration. For a cylinder, due to radial symmetry, the local fields need to be integrated only along the radius of the cylinder as shown on Figure 3-3(c). For a field of H' < H*, where the flux penetrates to the point r' as shown in Figure 3-3(c), $\mathcal{H}$ is found to be

$$\mathcal{H} = \begin{cases} \left(\dfrac{H^*}{R}\right) r + (H'-H^*) & r' < r < R \\ 0 & r < r' \end{cases} \quad (3-107)$$

Since $\int \mathcal{H} dv = L2\pi \int \mathcal{H} r dr$ in cylindrical coordinates where L is the length of the cylinder, then by integrating (3-107) from r=0 to R, equation (3-106) can be written,

$$B = \begin{cases} \dfrac{H^2}{H^*} - \dfrac{H^3}{3H^{*2}} & H < H^* \\ \dfrac{2}{3} H^* & H = H^* \\ H - \dfrac{H^*}{3} & H > H^* \end{cases} \quad (3-108)$$

The value of B for H = H* is found by setting H equal to H* in the H < H* term. Similarly, B for H > H* is found by taking the diamagnetic portion from the H = H* term (i.e. H* - 2/3 H*) and subtracting it from H. The corresponding magnetization expressions are written

$$-4\pi M = \begin{cases} H - \dfrac{H^2}{H^*} + \dfrac{H^3}{3H^{*2}} & H < H^* \\ \dfrac{H^*}{3} & H \geq H^* \end{cases} \qquad (3-109)$$

From Maxwell's equation (3-16), H* (in G) is found to be related to the critical state critical current j_c (in A/cm^2) by the equation[108]

$$\frac{H^*}{R} = \frac{-4\pi j_c}{10} \qquad (3-110)$$

where R is the radius of the sample (in cm) and c=10. The dimensional analysis of equation (3-110) and the explanation of why c=10 is given in appendix II. The second derivative of (3-109) for H < H* is negative, implying that the magnetization curve has a downward curvature within this region. This downward curvature in the magnetization is due to the decrease in the diamagnetic shielding with increasing field.

Equation (3-109) and (3-110) gives a direct relationship between the strength of the flux pinning and the corresponding magnetization behavior. Since the strength of the pinning is represented by the critical current j_c, stronger flux pinning giving a larger j_c will result in a higher H* for a sample of given radius R as shown by equation (3-110). The magnitude of 'H* will then affect the behavior of the magnetization curve given by (3-109).

Figure 3-4

$-4\pi M$

H

H* = 15

H* = 20

H* = 25
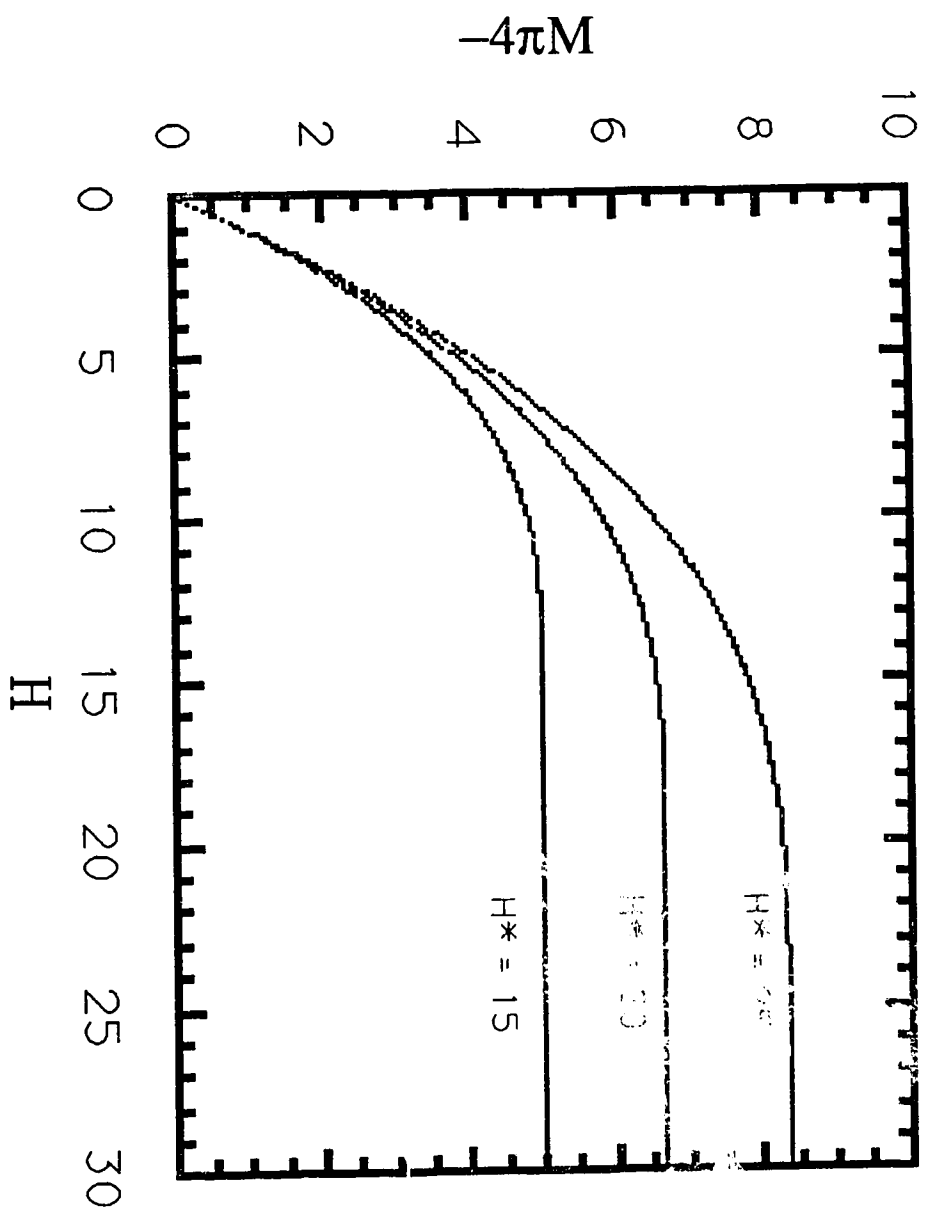
Figure 3-4 represents the way in which a change in H* affects the magnetization curve. The figure shows that with increasing H*, the curvature of magnetization becomes broader. This is because with increasing pinning energy (which increases j_c and H*), a larger Lorentz force must be applied to the vortex before the critical state, given by (3-102), is reached and thus fewer vortices can enter the material at a given applied field.

The Bean model not only describes the magnetization behavior for a hard superconductor, but also explains the hysteretic behavior observed in the magnetization curve with decreasing field. As the applied field is decreased, it becomes lower than the internal field within the outer regions of the hard superconductor. The resulting Lorentz force is now directed outward in these regions. Since the critical state given by equation (3-102) must still be satisfied, Bean's model states that the magnetic field profile becomes a complicated combination of regions having increasing and decreasing field profiles as shown in Figure 3-5. With decreasing field, the trapped flux within the superconductor makes the magnetization irreversible. Thus hysteresis found in the magnetization curve is another indication that flux pinning is occurring in the superconductor.

It must be understood that Bean does not explain the source of the linear field profile, but only shows that field independent flux pinning may give such an effect. The Bean model is more a mathematical analysis of the magnetization resulting from a linear field profile than a physical derivation of flux pinning. Therefore

7 1

Figure 3-5

(a)

H prior to
decrease

H after
decrease

D

(b)

D
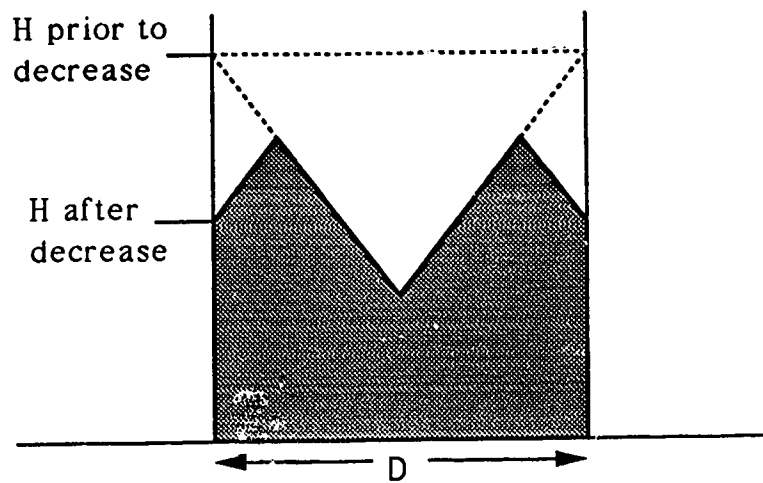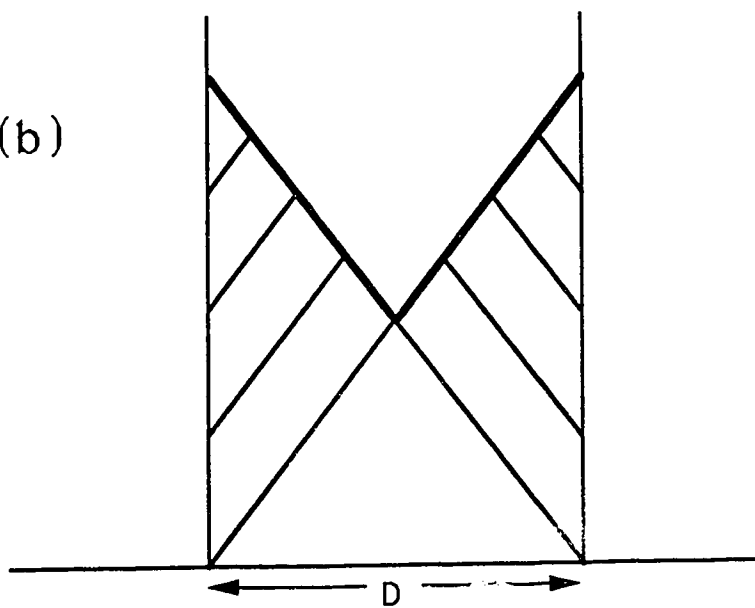
the model is strictly valid only under assumptions that Bean makes within his model. Realistically, there is no reason that flux pinning should result in a linear field profile. In fact, high field magnetization measurements made on high T_c superconductors for $H \gg H^*$ show that the magnetization decreases with increasing field; a characteristic not describable by the Bean model. Further Bean does not include any temperature dependence in his model, making it difficult to analyze the validity of the Bean model with temperature change. Thus there are several limitations that one should be aware of when using the Bean model. However, due to the simplicity of the model, it becomes quite useful when rough calculations of the magnetic critical current become necessary.

Ch. 4 <u>Basic Experimental Procedures</u>

Magnetic measurements are useful when investigating the anisotropy in these high T_c superconductors. For critical current measurements, the extremely small size of the samples makes transport measurements impossible. Instead, estimates of the critical currents can be obtained from magnetization measurements using the Bean critical state model. Also, since many of the intrinsic characteristic superconducting properties are related to the internal magnetic field (such as H_{c1}, H_{c2}, H_c and λ) magnetic measurements become crucial when investigating these properties.

The small size of the single crystals of $YBa_2Cu_3O_{7-\delta}$ makes the absolute magnetization signal very small. A typical mass of a single crystal $YBa_2Cu_3O_{7-\delta}$ is approximately 100 µg and the density is 6.398 g/cm^3. Thus in order to observe a sample magnetization of 1 emu/cm^3, the measuring instrument must be able to read an absolute magnetic moment of 1.6×10^{-5} emu. For such a small signal, the high sensitivity of a SQUID (superconducting quantum interference device) magnetometer becomes very useful. Typical sensitivity of a SQUID magnetometer is 1×10^{-9} emu, and if background signals are kept to a minimum, a signal of 5×10^{-8} emu can be measured[110].

The experiments that will be discussed in the following chapters were performed using two commercial SQUID magnetometers; a SHE VTS SQUID magnetometer with a 1 T magnet

and a Quantum Design MPMS SQUID magnetometer with a 5.5 T magnet. Both magnetometers use a continuous flow of He^4 gas near 4 K to cool the sample and are capable of measuring magnetization from room temperature to 4 K. In the SHE system, the sample is cooled directly by the He^4 vapor while in the Quantum Design system, there is an intermediate chamber which is cooled by the He^4 gas, which in turn the sample through heat conduction via a small pressure of He chamber.

The actual SQUID detection of the sample for both machines is performed using a superconducting flux transformer[111]. The background signal is kept to a minimum by arranging the pickup coils in a coil, counter-coil arrangement. In the SHE system the pickup coils are arranged so that the coil and counter-coil of equal turns are placed axially along the magnetic field as shown in Figure 4-1 (a). For each measurement, the sample passes through the coil and r-coil giving two signals of equal magnitude but with opp gn. The magnetic moment from the sample is obtained by adding the magnitud of the maximum signal from each coil and dividing by two. The Quantum Design system is a second order gradiometer where a counter coil of 2n windings is placed in the middle of two sets of coils having n windings as shown in Figure 4-1 (b). This coil arrangement not only will null any constant background signal but also any background signal that has a linear gradient along the axis of the coils. The sample is moved through the coil arrangement and the signal is fit to a

Figure 4-1
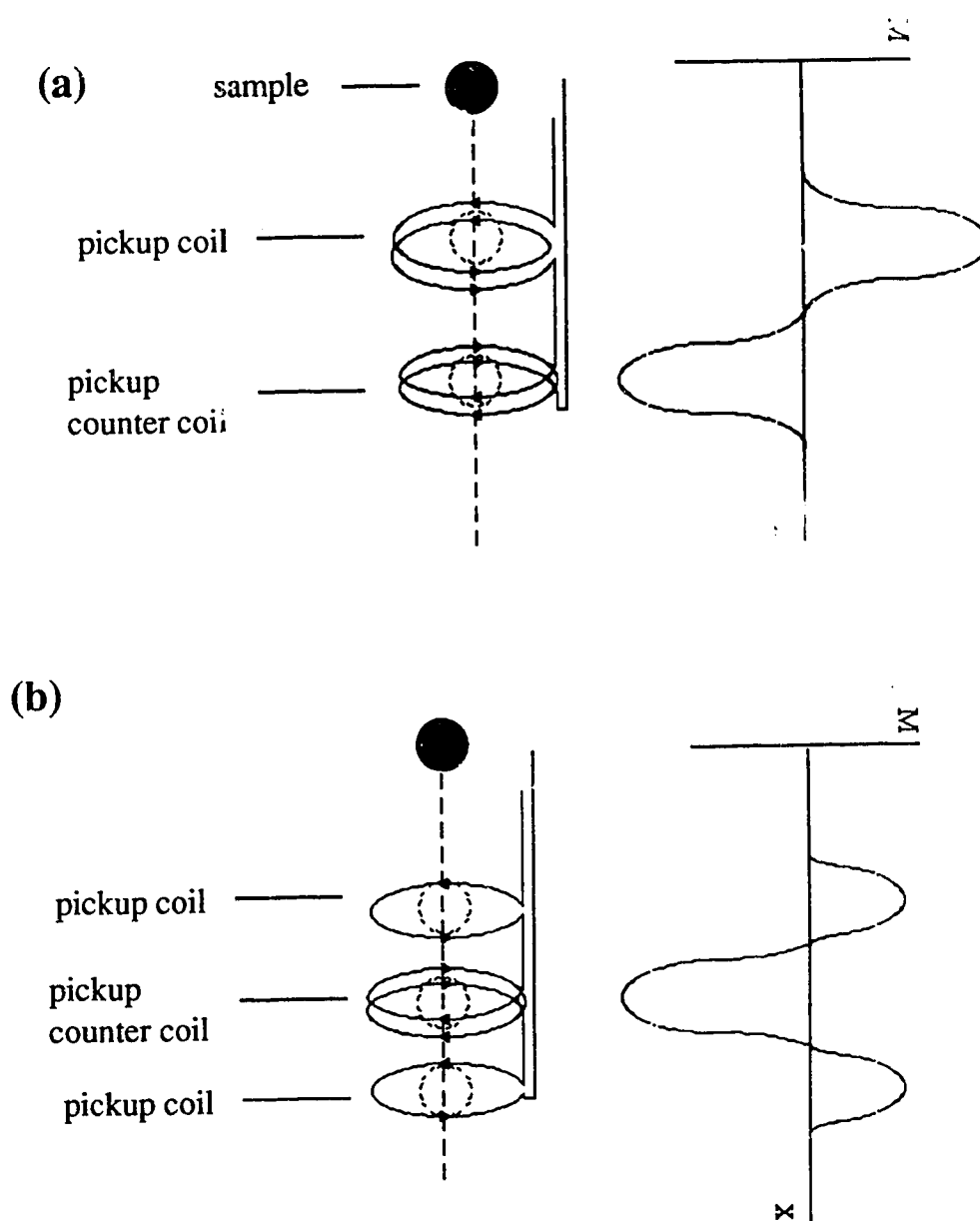
second gradient function to obtain the actual magnetic moment of the sample.

The signal of the sample holder was kept to a minimum by using materials having a small magnetic moment. The sample holder for the SHE SQUID consisted of a thin mylar sheet suspended by 40 gauge Cu wire. The mylar sheet was arranged either horizontally or vertically, depending upon whether the field was oriented along the c axis or in the a,b plane of the specimen. For the Quantum Design SQUID a thin quartz rod (~1.0 mm diameter) was placed such that the rod always passed through the center of all three coils throughout its entire travel. This arrangement was used so that the signal from the sample holder itself would also be nulled out. This method could not be used on the SHE SQUID because the distance from the lower pickup coil to the bottom of the sample chamber was shorter than the distance between the pickup coils. Since all the measurements taken using the Quantum Design SQUID were for the field in the a,b plane the platelike samples were easily attached to the side of the quartz rod using Apiezon N grease. Finally to minimize the effects of any gradients in the applied field from the magnet, the scanning length was kept to the smallest possible value that passed the sample through all the pickup coils. This length was 2 inches for the SHE SQUID and 5 cm for the Quantum Design SQUID.

All the measurements investigating the flux pinning behavior in the single crystals of $YBa_2Cu_3O_{7-\delta}$, were taken with the SHE SQUID magnetometer since the Quantum Design SQUID

77

magnetometer was not yet available at that time. Thus the maximum possible field that could be applied was 10 kG. For each of the magnetization measurements the sample was cooled in zero field to the desired temperature. After the temperature was stabilized, the magnetization measurements were taken for increasing field. After the maximum field of 10 kG was reached, corresponding magnetization measurements were taken for decreasing field in order to observe the magnetic hysteresis. In order to minimize any time dependent effects in the magnetization measurements, each measurement was taken exactly 15 minutes after the field was set. The value of H* given in the Bean model in Ch. 3 was determined from the maximum in the magnetization curve. For fields greater than H* the magnetization values were used to estimate the critical current j_c from the equations (3-109) and (3-110). For fields below H* Bean's assumption that j_c is field independent was taken to obtain a rough estimate for j_c.

Both the SHE SQUID magnetometer and the Quantum Design SQUID magnetometer were used to investigate the lower critical field in single crystals of $YBa_2Cu_3O_{7-\delta}$. Detailed magnetization measurements were taken to observe the field of flux entry most accurately. The data were then fed into a computer program which performed a linear least squares fit to the data. The number of points used to fit the line could be easily changed. The program displayed both the slope of the line, as well as the standard deviation. Finally, the program could subtract the magnetization data from the linear fit to obtain the data for the deviation curve.

The remnant field of the superconducting solenoid was minimized by degaussing the magnet at $T > T_c$ prior to each run. To degauss the magnet, a series of ramps were performed where each field ramp was followed by a field ramp in the opposite direction to half the field of the previous ramp (i.e. Hmax, -1/2 Hmax, 1/4 Hmax, ...). This series of field ramps was performed until the applied field was less than 1 G. Using this degaussing procedure the remnant field from the magnet was reduced to less than 1 G. The magnitude of the remnant field was determined by extrapolating the linear diamagnetic portion of the magnetization curves to zero. Every entry field value was corrected for the remnant field by subtracting the extrapolated estimate of the remnant field from the "as read" entry field. Further explanations of the experimental procedures for both the flux pinning experiment and the lower critical field experiment will be discussed in the following chapters.

Ch. 5 <u>Flux Pinning and Critical Currents in</u> YBa$_2$Cu$_3$O$_{7-\delta}$

Anisotropy in flux pinning, magnetization and critical currents

Some of the deepest investigations of high T$_c$ superconductors have been directed towards their possible technological applications. One such example is the fabrication of superconducting wires using these materials. However, a major drawback appeared when transport critical currents in polycrystalline samples were found to be very low compared to those in good A15 superconductors[112]. A major factor for the low critical currents arose from the poor connective nature of the superconductivity due to the granularity of the sintered polycrystalline samples. With the availability of single crystals[18-20], it has become possible for critical currents to be measured without the grain boundary problems inherent in the polycrystalline materials. However the small size of the single crystals makes direct measurement of transport critical currents on them impossible. Fortunately, using the critical state model discussed in Ch. 3, magnetization measurements can be used to get a rough estimate of the magnetic critical currents and their dependence on temperature and field.

In this chapter, magnetization measurements are discussed that have been performed to characterize the flux pinning behavior of bulk YBa$_2$Cu$_3$O$_{7-\delta}$[27]. The discussions in this chapter

will cover the anisotropy of the flux pinning and the magnetization critical currents due to the presence of flux pinning sites in the crystals. The magnetic critical currents of the single crystals will be compared with those of polycrystalline samples. Further discussions will cover the effects of neutron irradiation[113] on the enhancement of magnetization and flux pinning behavior. It should be noted that these are some of the preliminary measurements that were performed to observe the flux pinning effects in single crystals of $YBa_2Cu_3O_{7-\delta}$.

The single crystals of $YBa_2Cu_3O_{7-\delta}$ used for these measurements were prepared by Dr. J. Z. Liu using the self flux method[20]. Some details on single crystal growth of $YBa_2Cu_3O_{7-\delta}$, using the self flux method are discussed in appendix III. The crystals were found to be near cubic parallelepipeds with the dimensions being approximately 0.3 - 0.5 mm along the a,b axes and 0.25-0.3 mm along the c axis. The mass of the samples was found to be approximately 200 μg. X-ray measurements on several crystals showed an orthorhombic unit cell[20] with cell parameters being a = 3.82 Å, b = 3.88 Å and c = 11.67 Å.

The transition temperatures of the single crystals were measured in a special SQUID magnetometer designed to be operable in very low fields (H < 0.5 G), where data can be taken continuously as a function of temperature and field[114]. The transition curves were obtained by cooling the sample in zero field to 4.2 K, applying a field of 10 G, and measuring the magnetization with increasing temperature[115]. T_c was defined to be the

temperature where the onset of diamagnetism in the shielding curve occurred. All the crystals showed bulk superconductivity with T_c at approximately 92 K. Figure 5-1 shows an example of a zero field cooled temperature dependent magnetization curve for a single crystal of $YBa_2Cu_3O_{7-\delta}$ in an applied field of 10 G along the c axis. From Figure 5-1, T_c is found to be approximately 92.0 K with a 10 K transition width. As these crystals displayed high transition temperatures straight from growth, no additional annealing in oxygen was done on them. The polycrystalline samples used for comparative studies were prepared by mixing powders of Y_2O_3, CuO, and $BaCO_3$ in their proper stoichiometric ratios, pressing the powder into pellets, reacting the pellets in flowing O_2 at 950 C for 24 hours and finally annealing in flowing O_2 at 700 C for 24 hours, followed by a furnace cool to room temperature[116]. The shape of the polycrystalline sample used for the experiment was roughly a 5 mm cube.

D. C. magnetization measurements were performed using a commercial SHE SQUID magnetometer. The samples were initially cooled below T_c in zero field and after temperature stabilization, magnetization measurements were taken in fields up to 10 kG. For H//c, the field was increased in steps of 200 G up to 10 kG, while for H//a,b, field steps of 200 G were taken up to 1.4 kG, after which 1 kG steps were taken for the higher fields. In order to avoid any drift in the applied field from the magnet, each measurement was taken fifteen minutes after the field was set. After the magnetization measurements were taken up to 10 kG,

Figure 5-1

YBa$_2$Cu$_3$O$_{7-\delta}$

H∥c   10 G

M (Arbitrary Units)

T (K)
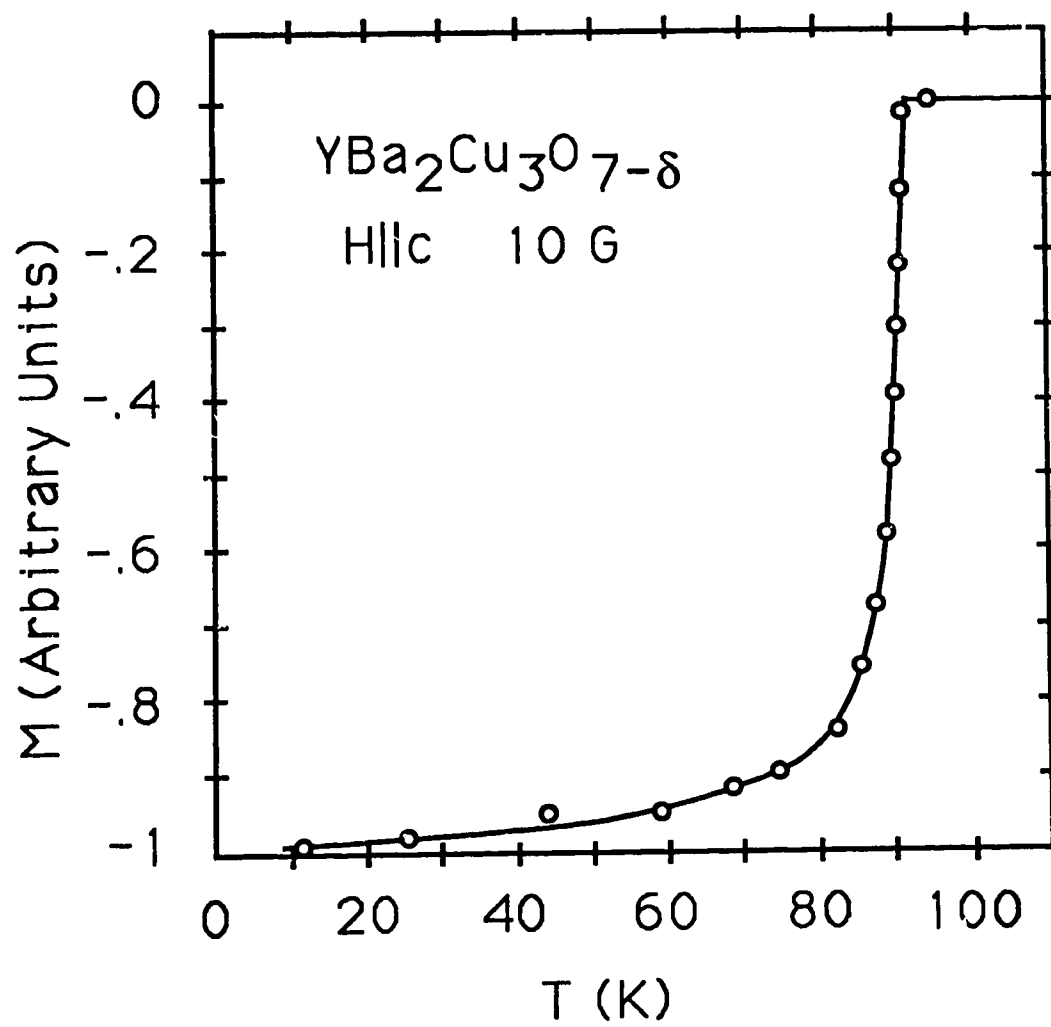
measurements were taken in decreasing fields to observe any hysteretic effects. Such measurements were done at temperatures of 5 K, 45 K, and 77 K.

The magnetization for fields in the a,b plane, and along the c axis for a single crystal of $YBa_2Cu_3O_{7-\delta}$ at 5 K is shown in Figure 5-2. The magnetization for H//c is found to be significantly larger than for H//a,b, suggesting anisotropy in the magnetic critical currents and flux pinning in the cubic shaped single crystal of $YBa_2Cu_3O_{7-\delta}$. The initial magnetization for fields along the c axis is only linear up to about 1 kG. Above 1 kG, the magnetization curve gradually deviates from linearity but continues to rise in diamagnetism up to 9 kG, as is typical of samples with strong flux pinning. Between 9 kG and 10 kG, the magnetization curve saturates, indicating constant diamagnetism in this field range. The magnetization curve for H//c shown in Figure 5-2, up to 10 kG, is similar in basic structure to the magnetization curve calculated from the Bean model as shown in Figure 3-4. The magnetization for fields in the a,b plane increases in magnitude up to approximately 1 kG. Beyond 1 kG, the magnetization curve is found to decrease in diamagnetism with increasing field. This decrease in the diamagnetic signal above 1 kG is not characteristic of the Bean model and indicates field dependent flux pinning in this field range for H//a,b. In the discussion of the Bean critical state model[108] in Ch. 3, a value H* was introduced to be the field where the system first encounters full field penetration as shown in Figure 3-3(b). From Bean's model, H* is characterized by the

84

Figure 5-2

$H\|c$

$H\|a,b$

Single Crystal $YBa_2Cu_3O_{7-\delta}$ $T = 5\,K$
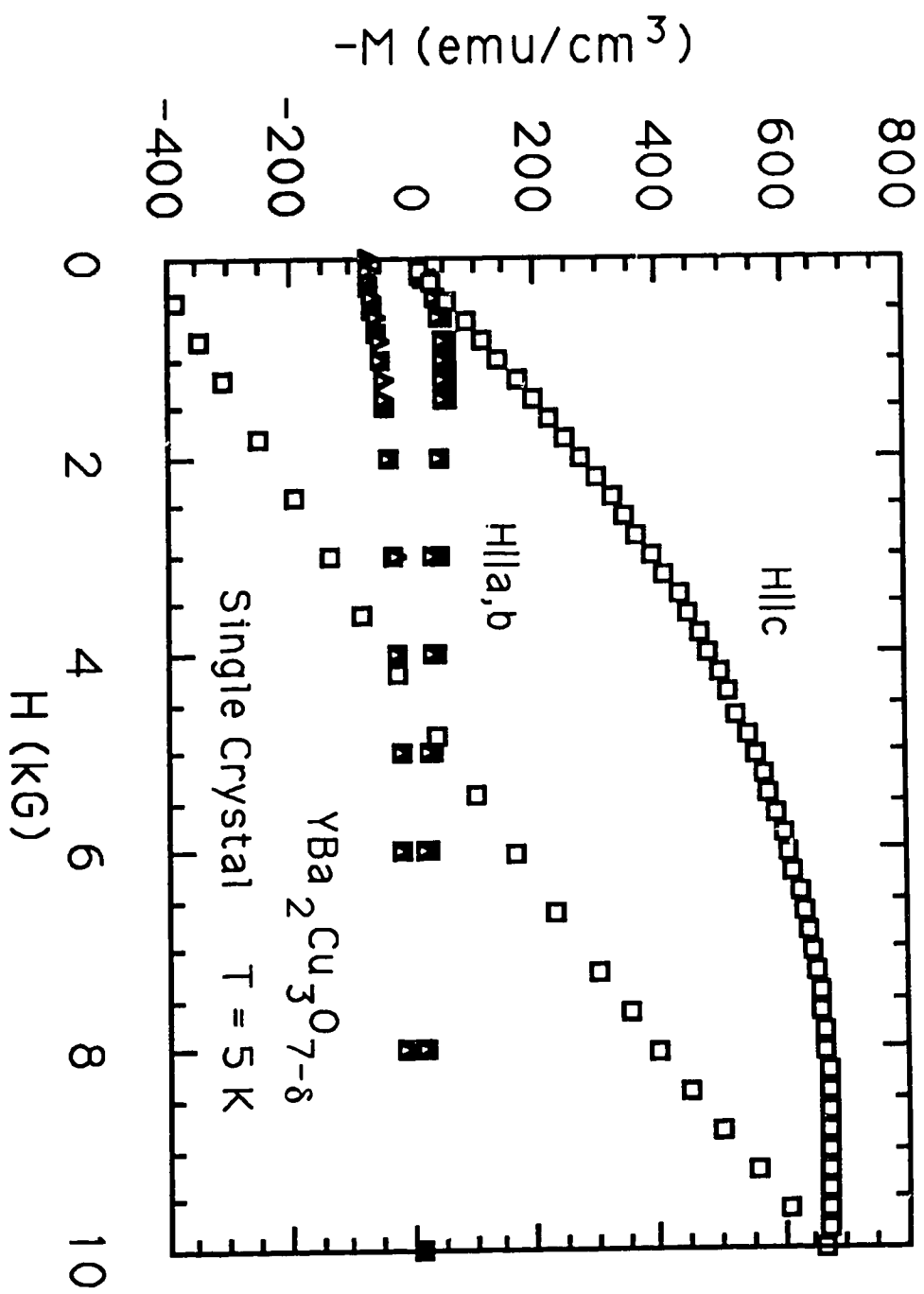
maximum in the diamagnetism found in the magnetization curve. From Figure 5-2, we can estimate H* to be approximately 9 kG for H//c and approximately 1 kG for H//a,b. For this nearly cubic shaped sample, the significantly smaller H* observed for H//a,b than for H//c also indicates a strong anisotropy in the flux pinning.

Irreversibility in the magnetization is also shown in Figure 5-2, resulting in magnetic hysteresis for all field orientations. This hysteretic behavior in the magnetization curve is further indication that flux pinning is present in the superconductor. In contrast to the large hysteresis observed in the magnetization for H//c, the magnetization for the H//a,b shows much less hysteresis. This lower hysteresis further confirms that there is significantly lower flux pinning for H//a,b than for H//c.

The magnetic critical current density j_c can be obtained from the magnetization curves using the Bean critical state model as discussed in Ch. 3. For these measurements, cylindrical approximations were taken to calculate the Bean critical magnetization current. From equations (3-109) and (3-110) the Bean critical magnetization current j_c (in A/cm^2) can be calculated from the magnetization M (in emu/cm^3) using the relation

$$j_c = \frac{30M}{R} \qquad (5-1)$$

for H ≥ H*, where R is the radius of the sample (in cm). Taking the radius as R = 1.5 mm, the critical magnetization current for the field along the c axis (i.e. for current in the a,b plane) is found to be 1.4 x 10^6 A/cm^2. The derived critical current is similar in

magnitude to that derived from magnetization measurements in thin films[117] of $YBa_2Cu_3O_{7-\delta}$. In Table 5-1, the critical magnetization currents for all field orientations at the different temperatures and fields are given. For fields in the a,b plane, the critical magnetization currents are much smaller and are strongly field dependent for fields above 1 kG as shown by Table 5-1. For fields less than 1 kG, J_c for H//a,b is a factor of 10 smaller than for H//c, falling to a factor of 50 smaller at 10 kG. Table 5-1 also shows the lower critical currents in the sample with increasing temperature for H//c.

Flux trapping and hysteresis for fields along the c axis decrease dramatically with increasing temperature as shown in Figure 5-3. The maximum values of the magnetization and the remnant flux are both a factor of 10 smaller at 45 K and a factor of 100 smaller at 77 K than at 5 K. This decrease in flux trapping is in agreement with the decreasing critical currents with increasing temperatures shown in Table 5-1. From Anderson's critical state model[107], equation (3-101) may be used to obtain the magnitude of the potential barrier of the pinning site. If we assume that the normal core of the flux vortex is cylindrical, the volume multiple of the pinning energy can be given as the cross sectional area of the vortex core times the dimension of the pinning site along the length of the vortices. Since the cross sectional area of the vortex can be written in terms of the coherence length, the flux pinning strength can be estimated from equation (3-101) to be

Table 5-1

T(K)	H(kG)	$j_c(A/cm^2)$			
		a	b	c	polycrystal
5	0 - 10			1.4×10^6	
5	1.0	1.2×10^5	1.1×10^5		
	4.0	7.3×10^4	6.0×10^4		1.4×10^4
	6.0	5.2×10^4	4.5×10^4		
	10.0	3.2×10^4	2.8×10^4		1.3×10^4
45	1.0			1.1×10^5	
	2.0				6.6×10^2
	4.0			9.4×10^4	
	8.0				6.2×10^2
	10.0			6.9×10^4	
77	1.0			1.1×10^4	
	2.0				2.3×10^2
	4.0			5.7×10^3	
	6.0				1.2×10^2
	10.0			4.3×10^3	

Figure 5-3

−M (emu/cm^3)

H (kG)

Single Crystal

YBa$_2$Cu$_3$O$_{7-\delta}$

H∥c

45 K

77 K
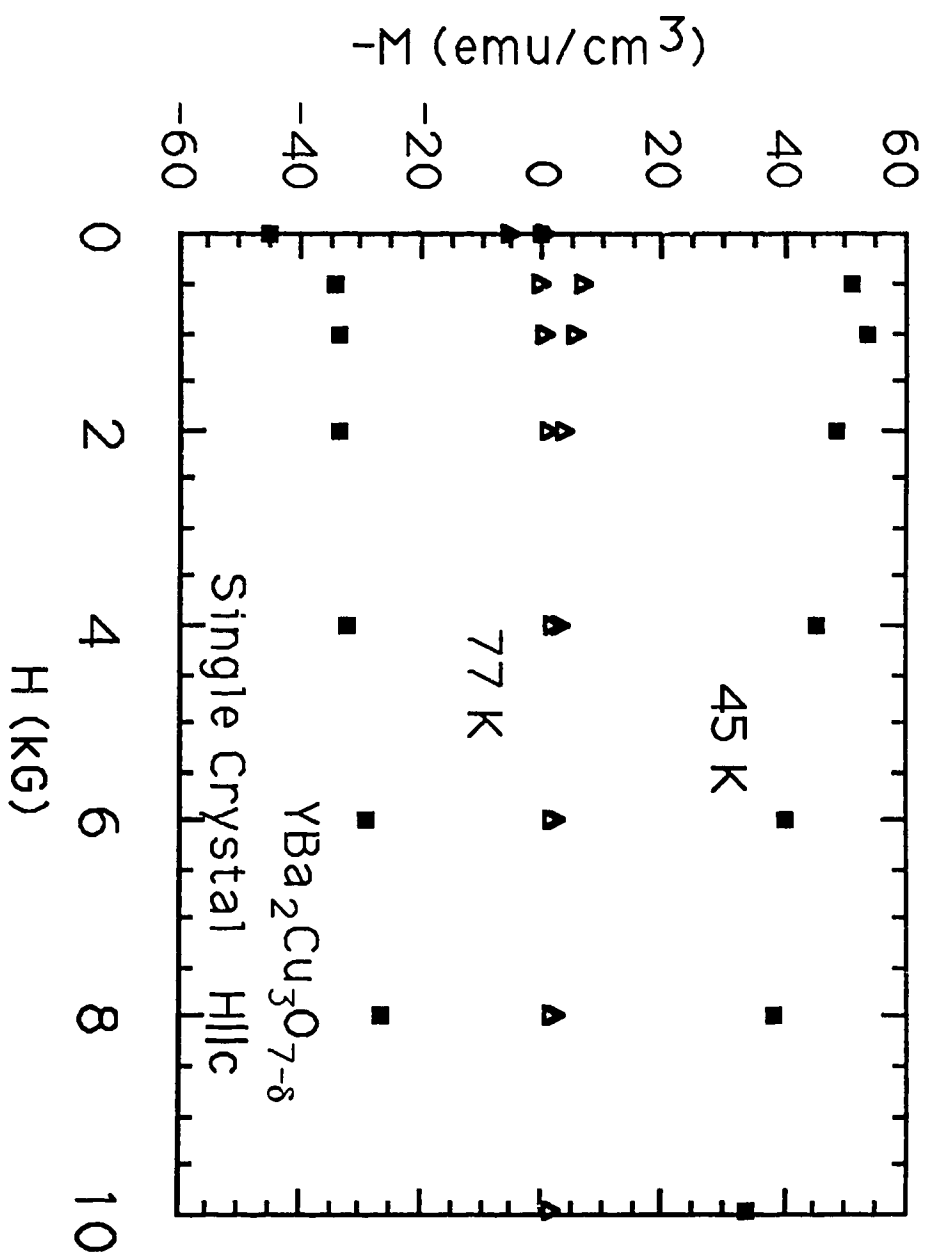
$$F_p = p \left(\frac{H_c^2}{8\pi} \right) \pi \xi^2 L \qquad (5\text{-}2)$$

where L is the dimension of the pinning site along the length of the vortex. Thus any change in the values of H_c or ξ will affect the flux pinning strength. Equation (5-2) indicates that the strong decrease in flux trapping at 45 K cannot be due to a degradation of the superconducting behavior since at $\frac{1}{2}$ T_c, the critical field, the coherence length, and the magnetic penetration depth have nearly achieved their limiting low temperature values. However with an increasing temperature there is an increase in the thermal energy $k_B T$, which is not considered in equation (5-2). This increase in the thermal energy will decrease the net potential barrier of the pinning site, resulting in a lower flux pinning potential with increasing temperature. Since at 77 K, the thermal activation is higher and the condensation energy lower, the hysteresis is found to become even smaller.

Magnetization measurements on polycrystals at 5 K, 45 K, and 77 K were carried out in order to compare their derived critical magnetization currents with that of the single crystal. The magnetization curve for the polycrystalline sample at 5 K resembles the single crystal curve for H//c but with a factor of 10 reduction in magnitude as shown by Figure 5-4. However, since the polycrystalline sample is a factor of ten larger in dimension than the single crystal, the derived critical magnetization current is two orders of magnitude smaller than that of the single crystal, as given in Table 5-1. At higher temperatures, the magnetization

90

Figure 5-4

$-M \ (emu/cm^3)$

H (kG)

○ 45 K   ▲ 77 K   ■ 5 K

$YBa_2Cu_3O_{7-\delta}$
Polycrystal

91
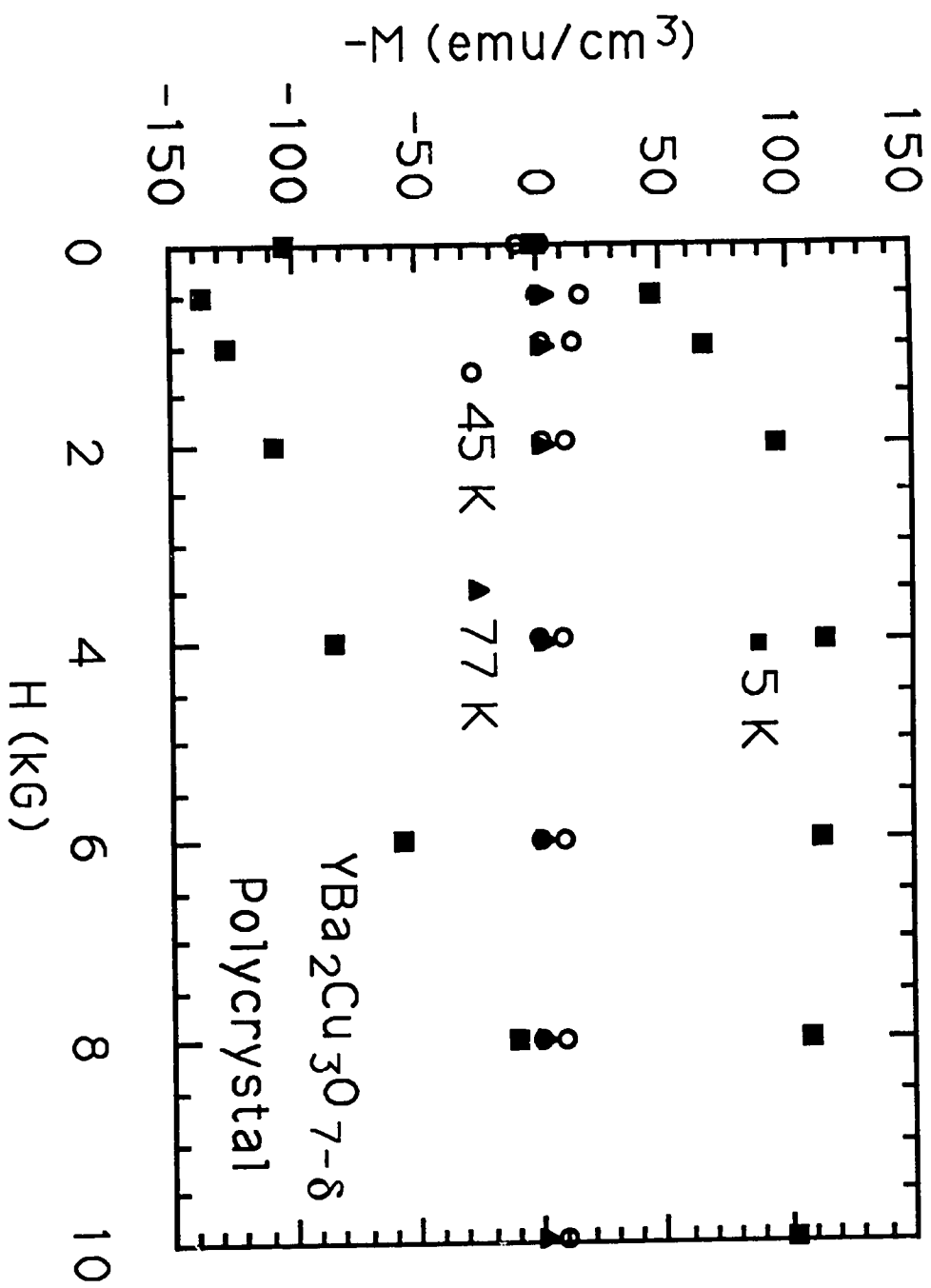
curves for the polycrystal become more nearly reversible and the critical magnetization currents decrease significantly as shown in Table 5-1. The derived critical magnetization currents for the polycrystal sample shown in Table 5-1 are in good agreement with those reported elsewhere[118,119]. These critical current values for the polycrystal are calculated with the assumption that the grain boundaries have not lost their superconductivity and that the supercurrents are travelling around the whole cross section of the polycrystal as shown in Figure 5-5(a). Assuming this to be true, the smaller magnitude of the critical current for the polycrystal suggests that the flux pinning energy is lower in the polycrystal than in the single crystal. The other assumption that can be made is that the grain boundaries have become normal, thus decoupling the supercurrent in the boundaries, such that they now only travel along the individual grains as shown in Figure 5-5(b). For such a case, the R value in equation (5-2) can be reduced to that of the individual grains and the critical currents are found to be larger. Since we do not know the actual dimensions of the individual grains for this sample, we cannot get a numerical value of the critical current, but an increase in the intra-grain critical current by a factor of one hundred is not out of the question. However even if the critical currents within the grains are high, this calculation assumes that the grain boundaries are no longer superconducting and that the currents cannot travel along the entire bulk of the polycrystal. Thus whichever assumption is taken, the polycrystalline samples are found to have a lower bulk

Figure 5-5

(a)
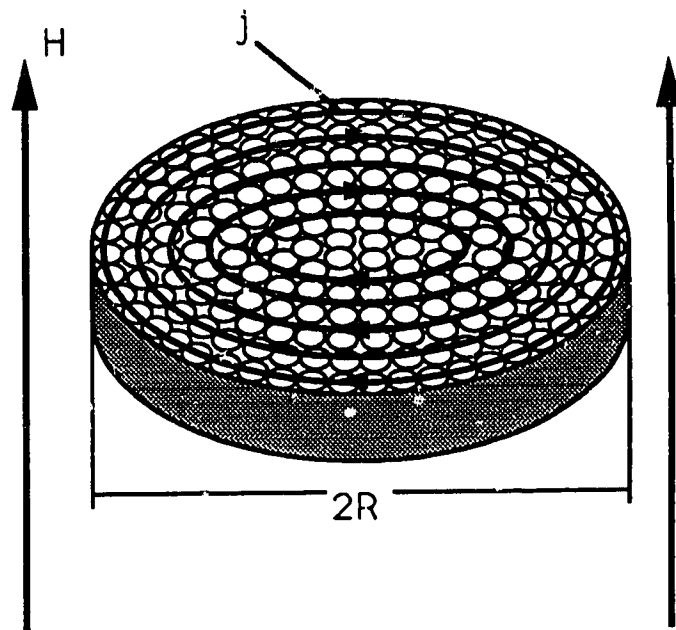
(b)
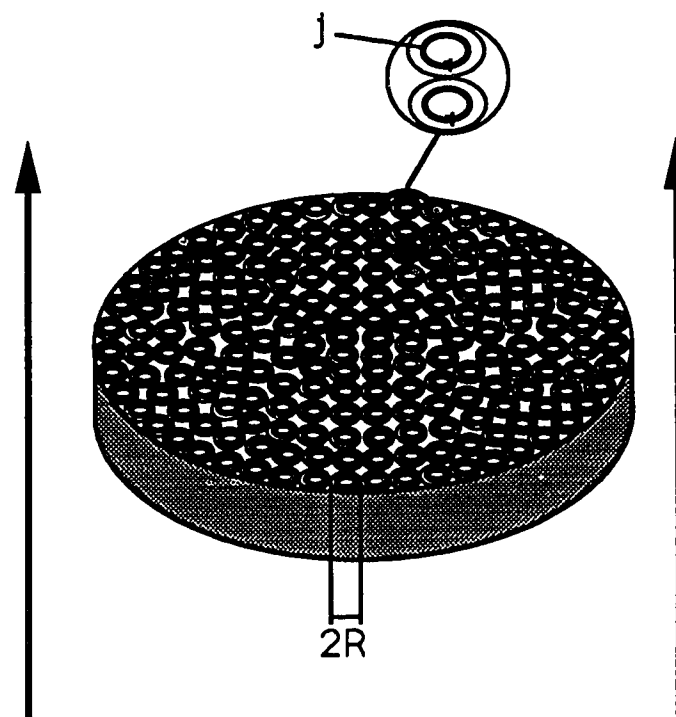
critical current than the single crystals. To eliminate the problem of the grain boundaries, one must either increase the critical current of the grain boundaries by increasing the inter-grain coupling or eliminate them altogether by making a long single crystal.

The anisotropy in the flux pinning can result from two basic effects, the anisotropy of the pinning defect dimensions and the anisotropy of the vortex filament. Since $YBa_2Cu_3O_{7-\delta}$ has uniaxial symmetry with the effective mass along the c axis much larger than the effective mass in the a,b plane, the coherence length along the c axis should be much smaller than that along the a,b plane. Upper critical field measurements by Welp et al. have found $\xi_{a,b}$ to be larger than ξ_c by a factor of six[21]. From equation (5-2), if we assume the pinning defect to be isotropic, the anisotropic pinning energy can be written as

$$F_p = p \left(\frac{H_c^2}{8\pi} \right) \pi \xi_{a,b}^2 L \quad \text{for} \quad H//c \qquad (5\text{-}3)$$

and

$$F_p = p \left(\frac{H_c^2}{8\pi} \right) \pi \xi_{b,a} \xi_c L \quad \text{for} \quad H//a,b.$$

Since ξ_c is smaller than $\xi_{a,b}$, F_p for $H//c$ should be larger than F_p for $H//a,b$. Our measurements, which show the critical currents for $H//c$ to be much larger than for $H//a,b$, are in agreement with the coherence length anisotropy and indicate that the anisotropic vortex dimensions may be affecting the flux pinning.

Aside from the anisotropic vortex dimensions, anisotropy in the pinning barrier dimensions also can cause pinning anisotropy.

94

An anisotropic pinning barrier would arise from an anisotropic modulation of the superconducting free energy at the defect site. A possible anisotropic pinning defect in the $YBa_2Cu_3O_{7-\delta}$ system is the twin boundary. For H//c, neglecting edge effects that curve the vortex line, the twin boundaries lie parallel to the vortices and thus can pin them along their entire length as they traverse the twinning plane. However, since the twin boundaries are <110> planes, unless the field was applied 45° to the a or b axis, the vortices will always cross the twinning planes as the vortices move through the crystal. If the field was oriented along the a or b axes (as in our experiment), then the pinning will be reduced due to two factors. Firstly, since the interaction of the vortex and the twin plane only occurs where the vortex crosses the plane, and not along the entire length of the vortex, the total pinning energy on the vortex will be smaller. Moreover, since the vortex is always crossing the twin as it travels, there is no true point of favorable energy anywhere in the path of the vortex. Thus in this orientation the twins would not act as good pinning sites. Thus twin planes may affect the overall characteristic of the flux pinning and its anisotropy in the $YBa_2Cu_3O_{7-\delta}$ system. Recent magnetization measurements by Welp et al.[120] and decoration experiments by Dolan et al.[121] suggest that twin boundaries do indeed pin vortices. Furthermore, transport measurements by Kwok et al.[122], magnetic torque measurements by Gyorgy et al.[123] and magnetization measurements by Liu et al.[124] have found indications that twin boundaries pin vortices more strongly when

95

the vortices lie parallel to the twin boundaries. Thus the twin boundaries in our sample also may be affecting the anisotropy in the flux pinning and the magnetic critical current.

To summarize, our measurements have shown that critical magnetization currents achievable in bulk material of the single crystal, far exceed those of sintered polycrystalline material. The current densities are sufficiently high for applications at low temperatures. However, the sharp decrease in the critical magnetization current with increasing temperature seems to be an inherent problem that is common to both polycrystalline samples and single crystals. Assuming this thermal degradation is unavoidable, our work suggests that a low temperature critical current of order 10^8 A/cm^2 is needed in order to achieve a working critical current of 10^6A/cm^2 at 77 K.

Enhanced critical magnetization currents through neutron irradiation

The inductive measurements on single crystal $YBa_2Cu_3O_{7-\delta}$ discussed in the previous section have given higher critical magnetization currents than previously observed from the polycrystals[27]. At higher temperatures however, the critical magnetization current values were found to be significantly smaller than those found at 5 K. Furthermore, the anisotropy found in the critical magnetization currents means that possibly there are restrictions in the orientation of the unit cell during fabrication. Thus enhancement in j_c and the reduction of the

96

anisotropy in the flux pinning would greatly improve the possibility of using $YBa_2Cu_3O_{7-\delta}$ for applications. To this end, the effects of fast neutron irradiation on $YBa_2Cu_3O_{7-\delta}$ have been investigated[113]. Since exposing the sample to neutron irradiation produces defects in the material, it may increase the flux pinning energy. Also, since the spatial separation of the pinning defects produced by the fast neutrons is roughly isotropic, investigations of the effect of neutron irradiation on the critical current anisotropy may be of interest.

The single crystal samples used in this experiment were prepared by the same technique as those used for our previous magnetization study[20]. The crystals ranged in mass from 175 µg - 497 µg with typical dimensions of 0.4 mm in the a,b plane and 0.2 mm along the c axis. The neutron irradiation was done at the H2 position of the Intense Pulse Neutron Source (IPNS) at Argonne National Laboratory. Three crystals were irradiated at 30° C with fast neutrons (E > 0.1 MeV) to fluences of 1.80×10^{17}, 2.98×10^{17}, and 8.16×10^{17} n/cm^2. Zero field cooled shielding measurements were taken by a special SQUID designed to operate at low fields, to determine T_c of the irradiated crystals. The field dependent magnetization curves were taken with a commercial SHE SQUID magnetometer at 6 K, 45 K and 77 K for fields along the c axis, and at 6 K for fields in the a,b plane. For all directions and temperatures, magnetization measurements were taken up to 10 kG.

Figure 5-6 shows the transition curve for the single crystals of $YBa_2Cu_3O_{7-\delta}$ irradiated at fluences of 8.16 x 10^{17} ncm^{-2} and 2.98 x 10^{17} ncm^{-2}. The T_c of these crystals were found to be above 91 K. The four crystals used in this study were not of equal quality. Although their transition temperatures were all above 91 K before irradiation, their shielding curves showed varying degrees of structure with decreasing temperature. Typically, the shielding curve showed a sharp superconducting transition at about 91.5 K followed by a shoulder at approximately 75 K and a second decrease at around 60 K.

Magnetization curves for the crystal with the highest neutron fluence are shown in Figures 5-7 for H//c and 5-8 for H//a,b. At 6 K, for the field along the c axis, the magnetization curve continues to increase for fields up to 10 kG as shown in Figure 5-7. At 10 kG, 71% of the applied flux is shielded from the sample. Of the flux that has entered at 10 kG, 67% remains trapped within the sample at zero field. In contrast, the magnetization of the unirradiated sample reported in the previous section[4] reached a maximum at 9 kG, indicating a smaller H* and lower flux pinning. Furthermore, the unirradiated sample shielded 65% of the applied flux at 10 kG and retained, at zero field, 55% of the flux that entered at 10 kG. Although higher field magnetization data are required to assess the full extent of the improvement in the irradiated sample, it is clear that neutron irradiation has increased the flux pinning and raised the critical magnetization current at 6 K. At 45 K and 77 K, the magnetization for the field along the

98

Figure 5-6

99

Figure 5-7

Figure 5-8

$-M(emu/cm^3)$

H(kG)

$8.16 \times 10^{17} n/cm^2$

H||a,b   T=6 K
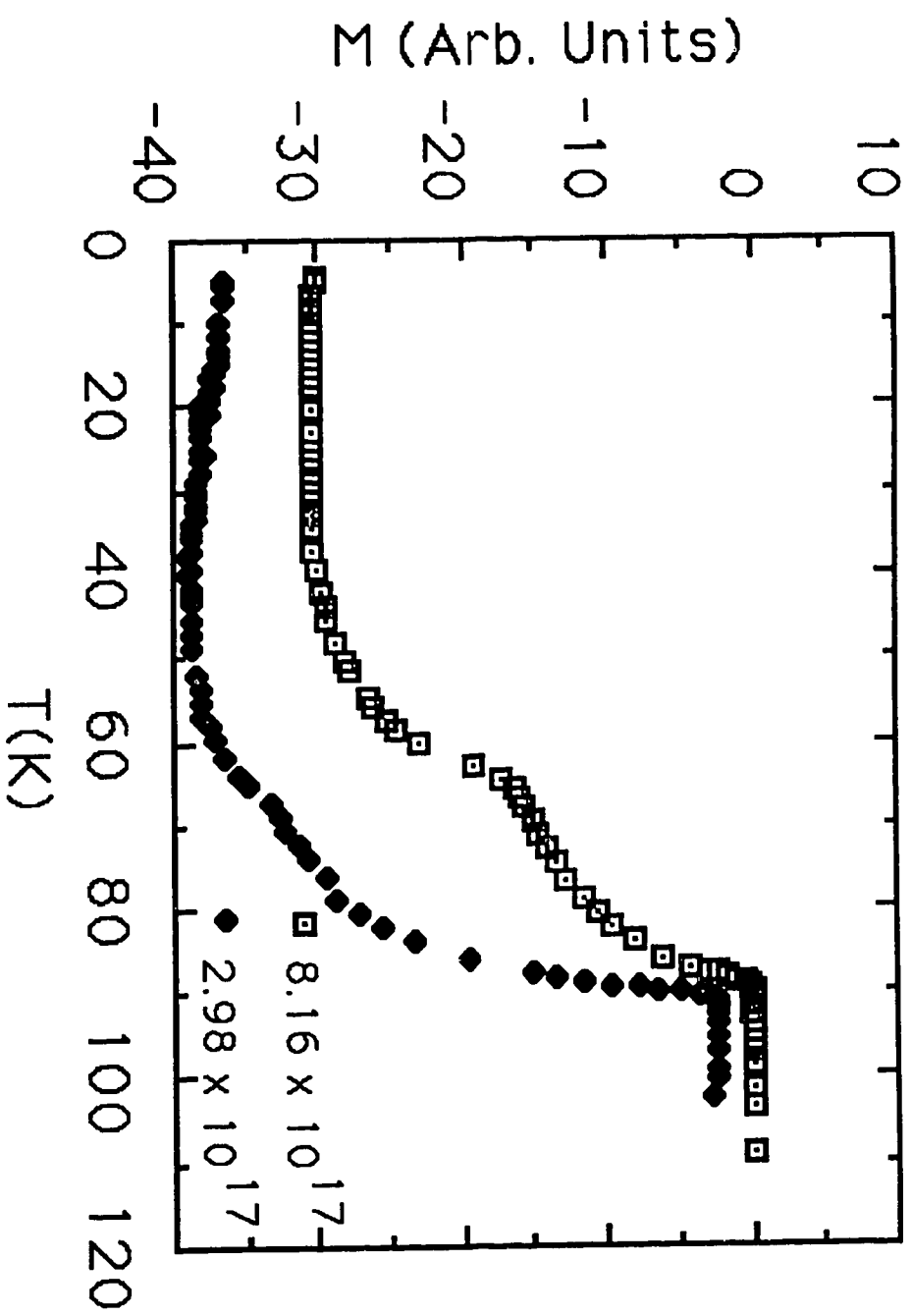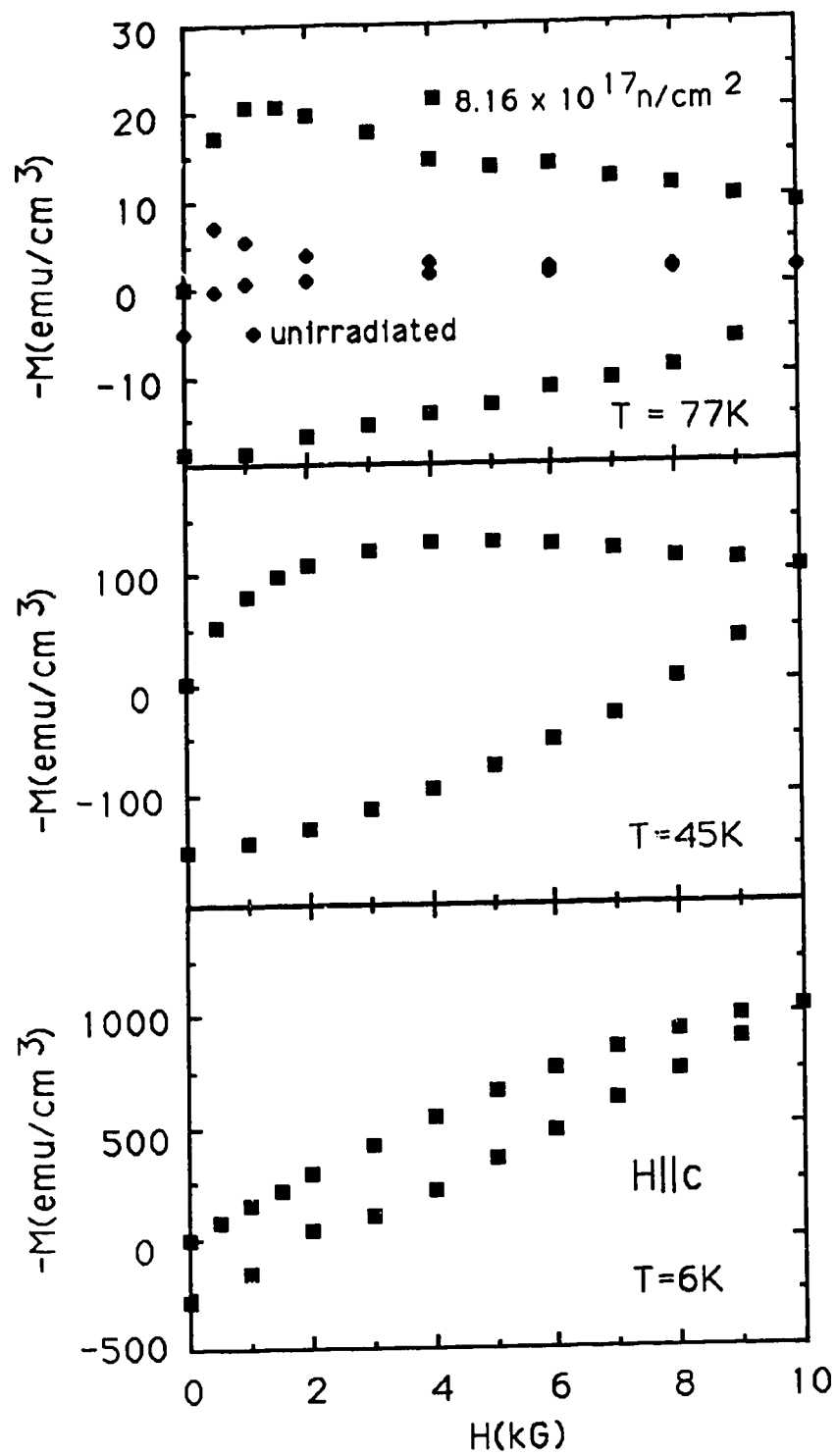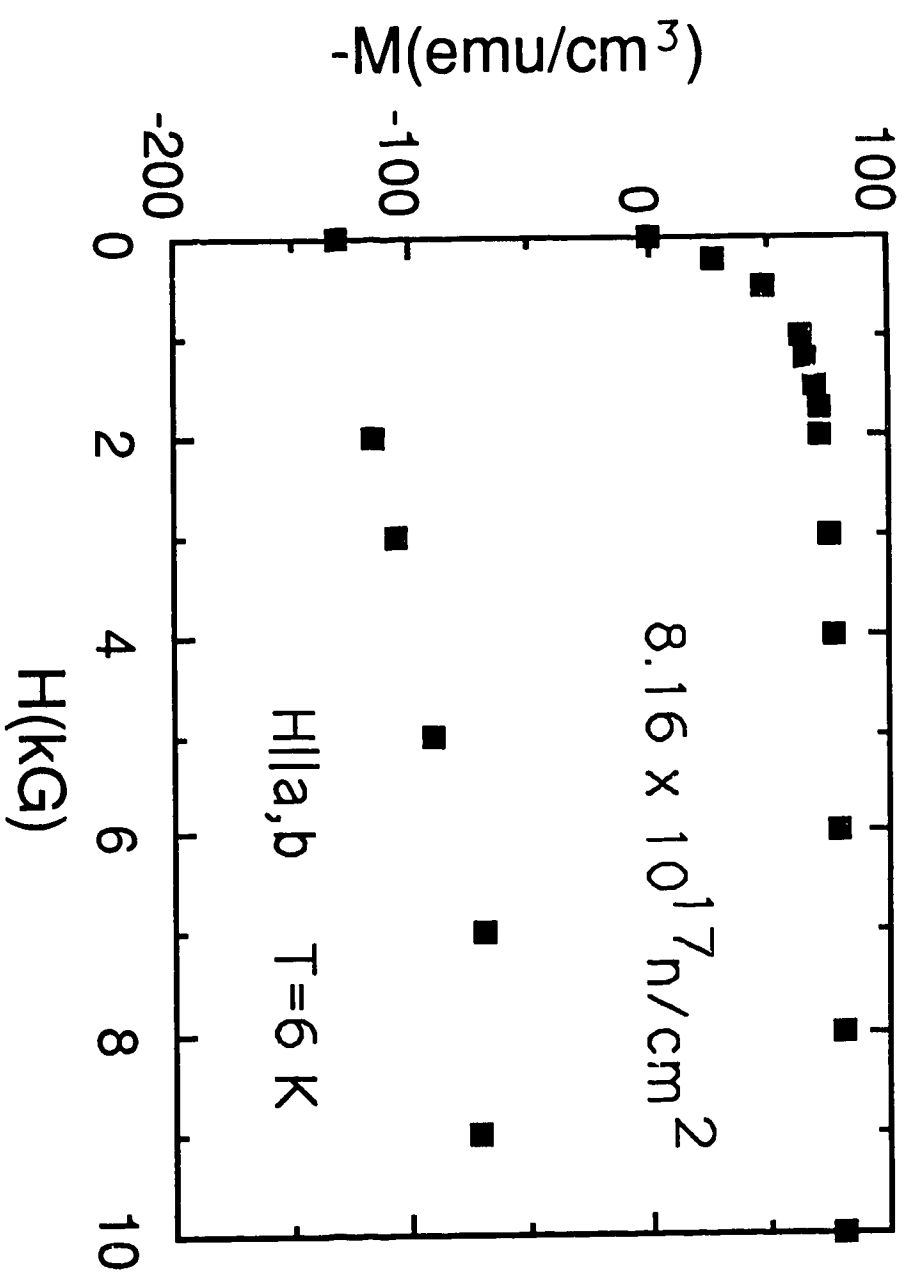
c axis reaches maxima at 3 kG and 1 kG respectively. Similar to the 6 K magnetization curve, the maxima at these temperatures occur at substantially higher fields compared to unirradiated samples. This indicates a higher H* and stronger flux pinning at these temperatures. In particular, at 77 K there is a significant hysteresis in the magnetization curve. This contrasts with the unirradiated sample whose magnetization curve at 77 K was nearly reversible above

4 kG.

The magnetization curve for fields in the a,b plane at 6 K showed a sharp increase for fields up to 2 kG followed by a gentle rise up to 10 kG as shown in Figure 5-8. This behavior is significantly different from that of the unirradiated sample where the magnetization reached a maximum below 1 kG and decreased by a factor of four between 1 kG and 10 kG. This difference in the magnetization curves further confirms an increase in flux pinning with neutron irradiation.

Since our samples have rectangular rather than circular cross sections, for these measurements the standard Bean formula (5-1) has been modified to accommodate the rectangular cross section[125]. This allows us to compare the critical magnetization currents for samples of different dimensions. For a sample of rectangular cross section $2a_1$ x $2a_2$ where $a_1 > a_2$ the magnetization is given by

$$M = \frac{a_2}{20} j_c (1 - \frac{a_2}{3a_1})$$
(5-4)

where a_1 and a_2 are in cm. In the limit $a_1 = a_2 = R$, this formula reduces to Bean's cylindrical form of (5-1). The calculations for obtaining equation (5-4) are shown in appendix IV.

The critical magnetization current derived from the magnetization curves on the irradiated and the unirradiated samples are shown in Figures 5-9 for H//c at 45 K and 77 K, and 5-10 for H//a,b at 6 K. At T = 6 K for H//c, since the magnetization curve did not reach a maximum below 10 kG, the Bean model could not be applied to obtain j_c. However, at 45 K and 77 K, j_c is found to increase with neutron fluence. At 10 kG, between the sample with the maximum irradiation and the unirradiated sample, there is a factor of 1.6 increase in j_c at 45 K and 2.4 increase at 77 K. The strong decrease in j_c with temperature observed in unirradiated samples is not as serious in the irradiated samples. In a field of 10 kG, the unirradiated sample showed a decrease in j_c of a factor of 16 between 45 K and 77 K. In the irradiated sample, this decrease is reduced to a factor of 11, 30% lower than in the unirradiated sample.

For H//a,b, both the magnitude and the field dependence of the critical magnetization currents are improved by irradiation as shown in Figure 5-10. In the sample with maximum irradiation, at 6 K, the magnetization is still increasing with field at 10 kG, making application of the Bean model questionable. Nevertheless, in order to make an approximate comparison, we use the Bean model on the slowly rising part of the magnetization curve only at 10 kG. The value of the critical magnetization current derived in

103

Figure 5-9

Figure 5-10

J_C (10^5 A/cm^2)

H (kG)

H||a,b T=6K

● 8.16 x 10^{17} ■ 1.80 x 10^{17}
◆ 2.98 x 10^{17} ◇ unirradiated

105
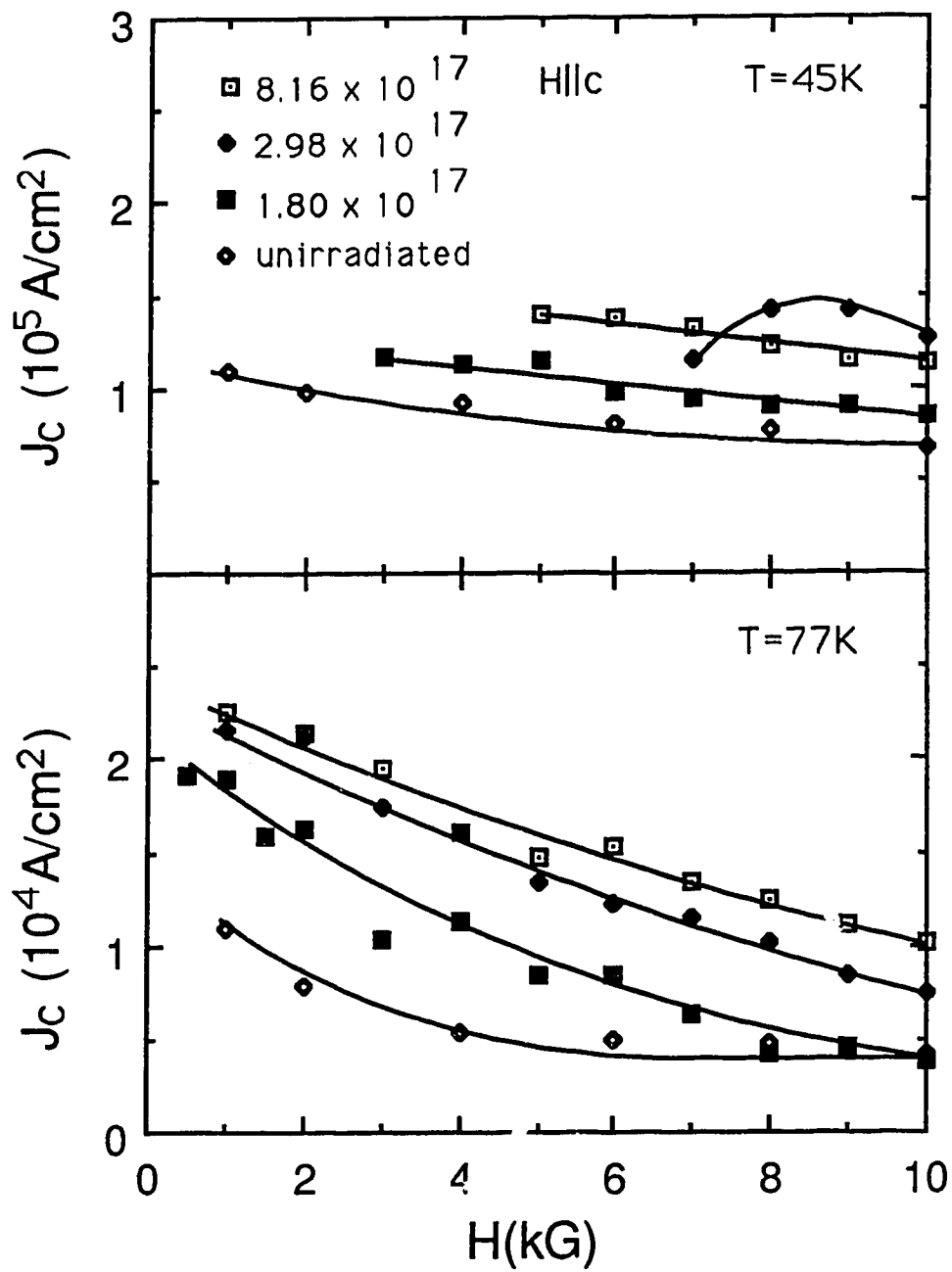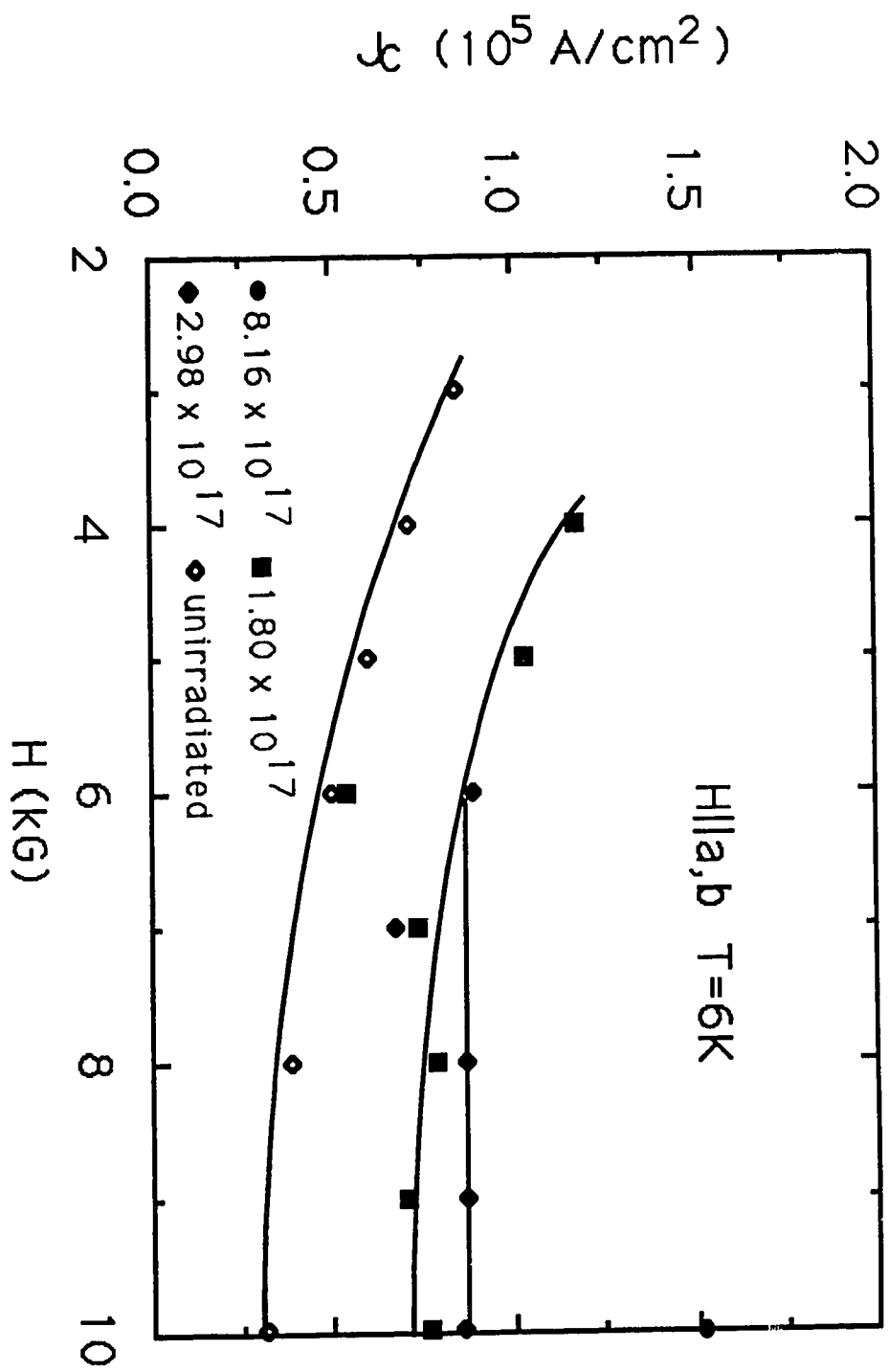
this way is therefore a lower limit. The field dependence of j_c in the irradiated sample is quite different from that of the unirradiated sample where a reduction of almost a factor of 4 occurs between 1 kG and 10 kG. At 10 kG the improvement of j_c with maximum irradiation is a factor of 5, the largest improvement observed in our experiment. This large increase for H//a,b compared to the smaller increase for H//c indicates that the strong anisotropy of j_c observed in unirradiated crystals is reduced by neutron irradiation.

The enhancement of the critical magnetization current can be expressed by the ratio of the j_c for the maximum irradiated crystal to the j_c of the unirradiated crystal[126,127], which will be defined as the dimensionless value $j_c{}^*$. Table 5-2 gives the enhancement ratio $j_c{}^*$ for the field of 10 kG along the c axis and in the basal plane at 45 and 77 K. From Table 5-2 it can be seen that in all cases there has been a enhancement in the critical magnetization current. It is also found that at the higher temperature of 77 K the critical magnetization enhancement due to irradiation is higher than at 45 K for both the basal plane and the c axis.

There is a slight decrease in superconducting transition temperature with irradiation as shown in Figure 5-11, where T_c has been defined as the onset of diamagnetism. The average decrease obtained from the initial slope of a least squares fit to the data is 2.6 $K/10^{18}$ n cm^{-2}. This is to be compared with 1.7 $K/10^{18}$ n cm^{-2} for polycrystalline $YBa_2Cu_3O_{7-\delta}$ at similar fluences[128] and 2.1 $K/10^{18}$ n cm^{-2} for polycrystalline

106

Table 5-2

T (K)	$j_c(H\|\|c)$, A/cm^2		$j_c(H\|\|a,b)$, A/cm^2	
	Irradiated Sample	Unirradiated Sample	Irradiated Sample	Unirradiated Sample
45 K	1.1×10^5	6.9×10^4	1.5×10^4	9.3×10^3
77 K	1.0×10^4	4.3×10^3	1.8×10^3	6.5×10^2

T (K)	Enhancement Ratio	
	$H\|\|a,b$	$H\|\|c$
45 K	1.6	1.6
77 K	2.8	2.4

Figure 5-11

108
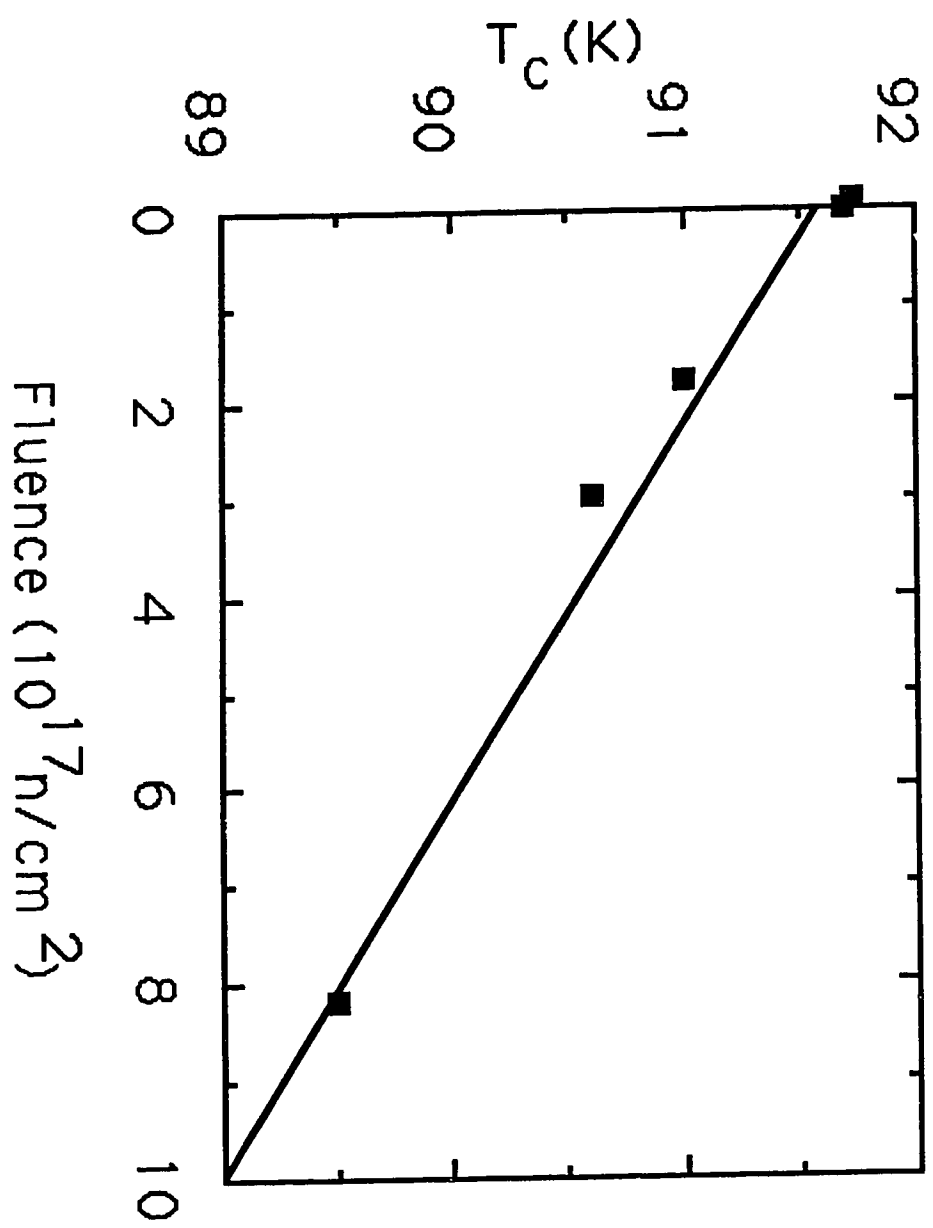
$La_{1.85}Sr_{0.15}CuO_4$[129]. In all cases the slope was obtained from a small number of points making precise comparisons difficult. The percentage decrease in the transition temperature of $YBa_2Cu_3O_{7-\delta}$ with neutron fluence is comparable but slightly less than that typically observed in the A15 superconductors[105,130]. This indicates that higher neutron fluences may possibly be used without much degradation in T_c.

The structure in the shielding curves illustrated in Figure 5-6 indicates that the temperature dependence of the shielding characteristics varies from sample to sample, especially in the temperature range above ~45 K. Thus some of the irregularities in the critical magnetization currents of the irradiated samples in this temperature range may be related to variations in the shielding properties among the samples.

Though more research is necessary, the data show that neutron irradiation may be a viable method for improving the strength of the flux pinning and raising the critical magnetization current of $YBa_2Cu_3O_{7-\delta}$. The larger increase in the critical magnetization current at 77 K compared to 45 K makes neutron irradiation an attractive method for increasing the critical current for applications intended to operate at liquid nitrogen temperatures. The fact that the largest improvements in the critical magnetization currents were observed for fields along the a direction suggests that the anisotropy in the critical magnetization currents observed in unirradiated crystals may not be intrinsic. The systematic increase of the critical magnetization current with

neutron fluence indicates that further significant increases can be achieved with higher fluences without severely depressing the transition temperature.

Recent experiments have been conducted by Sauerzopf [131], Wiesinger and Weber[132] to continue with the irradiation work that is given in this chapter. They modified the experimental procedures in two significant ways. Firstly, the neutron fluence was increased to 10^{18} n/cm^2 to investigate the effect of higher neutron dosage on the flux pinning. Secondly, their investigations on neutron irradiation were done using only one single crystal of $YBa_2Cu_3O_{7-\delta}$ so that sample dependent variables did not have to be considered. Magnetization measurements on the sample irradiated in fluences up to 2 x 10^{18} n/cm^2 showed significant increases in the magnetization hysteresis and critical currents in temperatures up to 40 K and fields up to 80 kG. The critical current enhancement ratio j_c^* at T = 40 K was found to be 15 for H//c at 2 T and 20 for H//a,b at 6 T. Extrapolation of the H = 2 T along c data to 77 K leads to an enhancement ratio of ~ 75 at that temperature. Finally, the anisotropy in j_c was found to decrease with neutron irradiation. The increase of the critical magnetization current with neutron irradiation on the one sample indicates these increases are independent of sample properties, and is in agreement with our results. Neutron irradiation experiments done on single crystal $YBa_2Cu_3O_{7-\delta}$ by van Dover et al.[133] have also showed critical current enhancement to be 100 at 77 K for H = 0.9 T along c, in agreement with the results by Sauerzopf et al.[131,132]

These measurements further display the viability of neutron irradiation for increasing critical currents in the $YBa_2Cu_3O_{7-\delta}$ system.

Ch. 6 <u>The lower critical field of</u> <u>YBa₂Cu₃O₇₋δ</u>

Strong incentives for studying the anisotropy in the superconductivity of $YBa_2Cu_3O_{7-\delta}$ emerged with the indications of strong anisotropy in the electronic structure of the high T_c superconductors[50-59] and the recent availability of high quality single crystals of $YBa_2Cu_3O_{7-\delta}$[18-20]. For a type II superconductor, two important characteristics that can be investigated are the upper and lower critical fields. As discussed in Ch. 3, by determining these two parameters for a material, one can estimate many of the other superconducting characteristics such as its penetration depth, coherence length, thermodynamical critical field and the GL parameter. Further, by investigating the anisotropy in these parameters one can get insight into if and how the anisotropy is affecting the superconducting properties (such as the geometry of the vortex).

This chapter contains discussions of measurements of the lower critical field, determined from highly detailed magnetization measurements on single crystals of $YBa_2Cu_3O_{7-\delta}$. In early sections of this chapter the magnitude and anisotropy of H_{c1} at low temperatures[22] will be discussed and from these values, magnitude of the magnetic penetration depth λ will be estimated. Further sections of this chapter will cover measurements of the temperature dependence of the lower critical field and compare them to other H_{c1} measurements as well as direct measurements

112

of λ. The final sections of the chapter will cover the investigation of the a-b anisotropy of H_{c1}, measured on an untwinned crystal of $YBa_2Cu_3O_{7-\delta}$ as well as the investigations on the effects of twin boundaries on the measurements of H_{c1}.

Low temperature measurements of H_{c1}

The isothermal magnetization curve for an ideal type II superconductor is shown in Figure 6-1(a). At H_{c1} there is a sudden break in the diamagnetism as flux vortices enter the superconducting material, resulting in a kink in the magnetization curve. Thus for an ideal type II superconductor, the value of H_{c1} can be easily determined by the location of this kink. However for a hard, type II superconductor, the flux pinning sites prevent the vortices from fully entering the sample, such that the distinctive kink in the magnetization curve at H_{c1} is replaced by a gradual deviation of the increasing diamagnetic signal from linearity, as shown in Figure 6-1(b). Without the easily distinguishable kink present in the magnetization curve, an accurate determination of H_{c1} in a hard superconductor becomes a much more difficult task. As was discussed in Ch. 4, the $YBa_2Cu_3O_{7-\delta}$ system was found to have strong flux pinning[27], indicating that the determination of H_{c1} would be difficult for this material. One method for obtaining H_{c1} is to best determine the field of first flux entry (or entry field), where the magnetization first deviates from linearity. In order to do so, detailed magnetization measurements can be taken on the superconductor, to fields well beyond its linear diamagnetic

Figure 6-1

(a)   Ideal Type II Superconductor
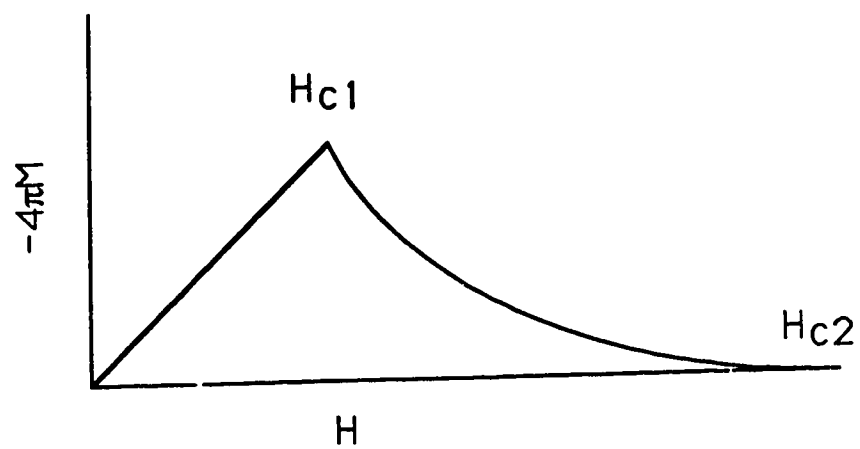
(b)   With Flux Pinning
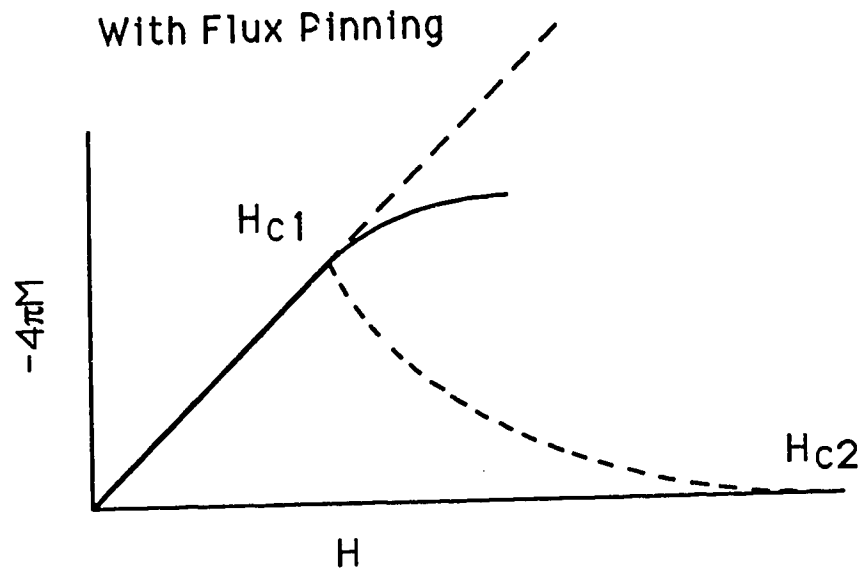
region. A linear least squares fit can then be made to the low field, diamagnetic portion of the data. By subtracting each magnetization measurement from this linear fit, any deviation of the measured magnetization curve from linearity will give a non-zero value for the difference. Using this method a small deviation can be observed directly, independent of the magnitude of the magnetization curve, so that the point of first flux entry can be determined with the highest possible resolution from the measurement.

Single crystals of $YBa_2Cu_3O_{7-\delta}$ used for this experiment[22] were of the same type as those described in Ch. 4.[20] Substantial twinning found in these crystals prevented the determination of anisotropy in H_{c1} within the a,b plane. Thus the H_{c1} anisotropy discussed in this section will only cover that between H//c and H//a,b. The a,b anisotropy of H_{c1} will be discussed in later sections of the chapter. To investigate the sample dependence in these measurements, three types of single crystal $YBa_2Cu_3O_{7-\delta}$ were selected: one as-grown, the second as-grown and annealed at 550 °C for 72 hours in pure oxygen, and the third as-grown and irradiated with fast neutrons (E > 0.1 eV) to a fluence of 8.16×10^{17} n/cm^2. Magnetization measurements were taken using a commercial SHE SQUID magnetometer at a low temperature of 11 K in fields up to 3 kG, on a relatively fine grid of fields with increments of 10 G for fields in the a,b plane and 50 G for fields along the c axis. Since the deviation curve must be observed with

the highest possible resolution, the high sensitivity of the SQUID makes it ideal for performing these measurements.

The magnetization curve for the field along the c axis in the as-grown crystal is shown in Figure 6-2. The magnetization curve is found to gradually deviate from linearity, indicating strong flux pinning in this sample. From Figure 6-2 the first deviation from linearity observable from the magnetization curve is found to be at approximately 1 kG. To obtain the highest sensitivity in determining the entry field, a deviation plot of ΔM vs H was constructed by subtracting the linear fit to the low field points from the measured magnetization data. The deviation plot created from the data in Figure 6-2 is shown in Figure 6-3. It can be seen that the first deviation from linear behavior occurs at 425 ± 50 G, a much lower field than is evident in Figure 6-2. Indeed, at an applied field of 1500 G, the deviation from linearity is only 10 G, a value that is barely detectable directly from the magnetization curve. These figures show the advantage of using the deviation curve over the magnetization curve when determining the field of first flux entry.

For fields in the a,b plane, a comparison of the deviation curve for two crystals is shown in Figure 6-4. One curve represents the magnetization of the as grown single crystal while the other curve represents the magnetization for the annealed crystal. From Figure 6-4, the deviation from linearity is found to be sharper for the annealed crystal as compared to the as-grown crystal, suggesting lower flux pinning in the annealed crystal.

116

Figure 6-2

YBa$_2$Cu$_3$O$_{7-\delta}$
H||c
T=11K

Figure 6-3

$YBa_2Cu_3O_{7-\delta}$
$H\|c$
$T=11K$

118

Figure 6-4

ΔM (emu/cm^3)

YBa$_2$Cu$_3$O$_{7-\delta}$
H||a,b
T=11K

☐ as grown
■ annealed

H(G)
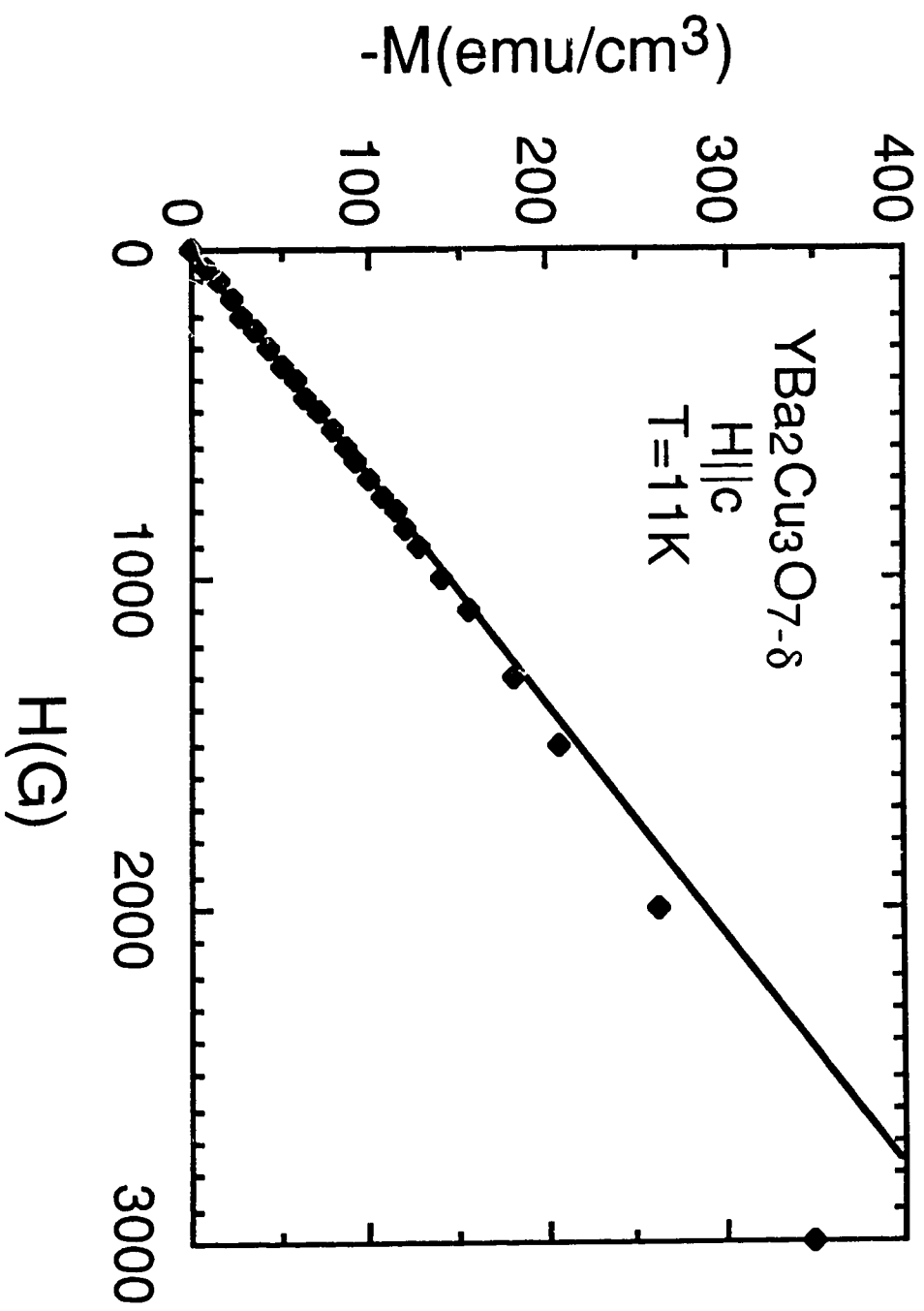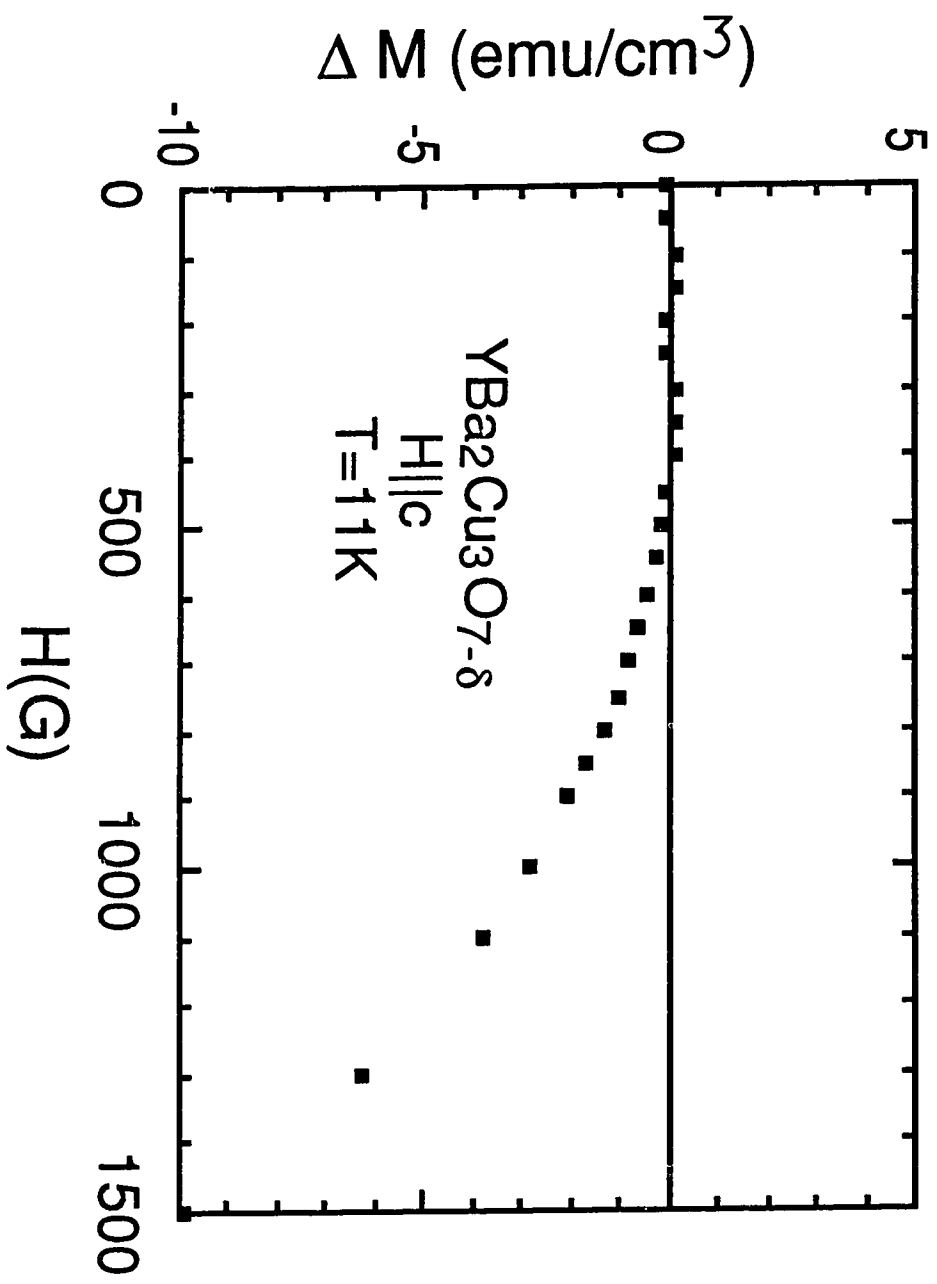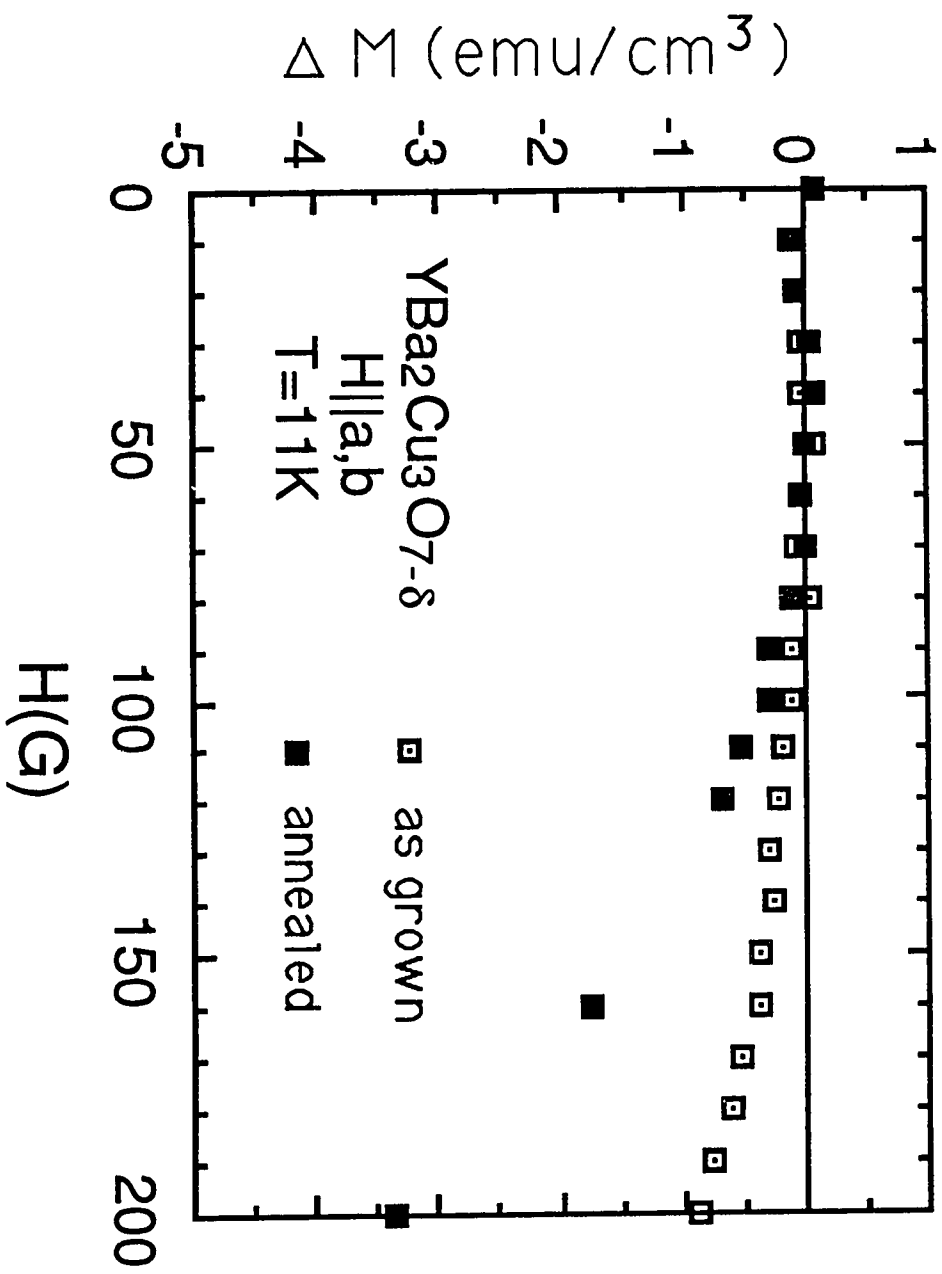
However, both samples exhibit the first departure from linearity at nearly the same field, indicating that the entry field is independent of sample hardness.

The values of H_{c1} can be determined from the entry fields obtained from the magnetization curves by correcting for demagnetization effects. How demagnetization effects, which arise from the sample's geometry, influence the magnetization measurements can be understood by considering an ellipsoidal superconductor shown in Figure 6-5. If an ellipsoidal superconductor in the Meissner state is oriented such that the large cross-sectional area is perpendicular to the applied field as shown in Figure 6-5(a), then the local internal fields become much larger than the applied field, which results in a large demagnetization effect. If this same ellipsoid was reoriented so that the small cross-sectional area was perpendicular to the field as shown in Figure 6-5(b), the local internal fields become closer in magnitude to the applied field and the demagnetization effects become less severe. The magnetic induction for a material having demagnetization effects is written as

$$B = H + 4\pi M(1-n), \qquad (6-1)$$

where H is the applied field, M is the magnetization and n is the defined to be the demagnetization factor $(0 < n < 1)^{134}$. Since $B = 0$ for a superconductor exhibiting full diamagnetism, n can be obtained from the initial slope of the magnetization curve by

$$\frac{M}{H} = -\frac{1}{4\pi(1-n)}. \qquad (6-2)$$

Figure 6-5

Effect of shape on n

(a)

$n \to 1$

(b)

$n \ll 1$
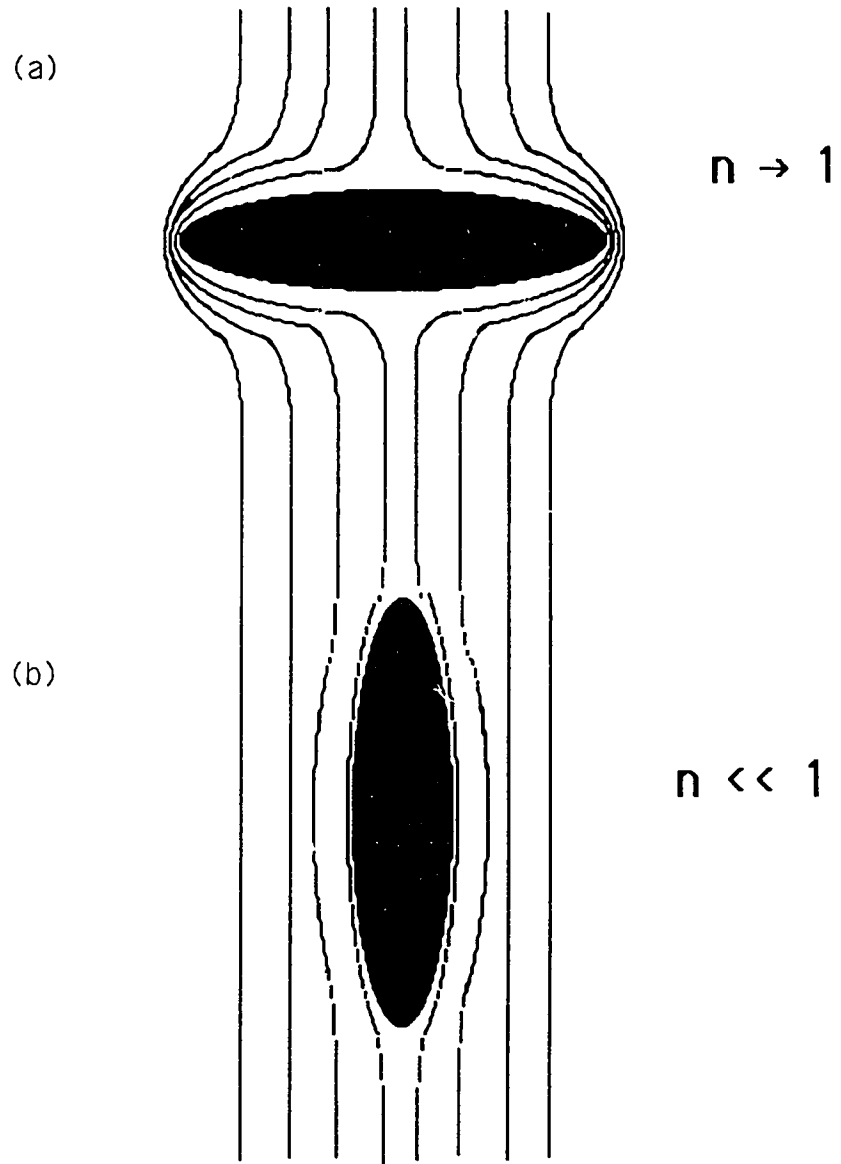
Since from (6-2), it is evident that n influences the change in the magnitude of the magnetization with the applied field, the field of first flux entry becomes dependent upon n as well. The intrinsic value of H_{c1} can be obtained from the n dependent entry field H_e, by the relation

$$H_{c1} = \frac{H_e}{(1-n)}. \qquad (6-3)$$

By determining the value of n from the linear slope of the magnetization curves using equation (6-2), H_{c1} values can be determined from the entry field and n using equation (6-3). The data for the three crystals are summarized in Table 6-1, giving weighted average values of H_{c1} of 120 ± 14 G for fields in the a,b plane and 690 ± 90 G for fields along the c axis. This gives an anisotropy in H_{c1} of approximately 5.

From the anisotropic GL theory, discussed in Ch. 3, the anisotropy in the lower critical field should be comparable to the anisotropy in the upper critical field, since they both are related to the effective mass by the equations in (3-82). Temperature dependent magnetization measurements on single crystals of $YBa_2Cu_3O_{7-\delta}$ by Welp et al.[21] have shown H_{c2} to be anisotropic with the temperature dependent slopes near T_c $\left.\frac{dH_{c2}}{dT}\right|_{T_c} = -19$ kG/K for H//c and $\left.\frac{dH_{c2}}{dT}\right|_{T_c} = -105$ kG/K for H//a,b. From these slopes, low temperature extrapolations of the H_{c2} curves were estimated by Welp et al. to be 6470 kG for H//a,b and 1220 kG for H//c[21]. These H_{c2} values indicate the anisotropy in the upper

Table 6-1

	H_e (G)		n		H_{c1} (G)	
	lla,b ± 10	llc ± 50			lla,b ± 14	llc ± 90
As-Grown Sample	95	425	.31 (lla,b)	.45 (llc)	137	772
Annealed Sample	85	375	.31 (lla,b)	.47 (llc)	108	707
Irradiated Sample	90	325	.27 (lla,b)	.46 (llc)	123	601
weighted average	90	375			~120	~690

123

critical field to be approximately 5, in rough agreement with the H_{c1} anisotropy.

From Ch. 3, equations (3-52) and (3-66) can be conveniently combined into a single equation for κ,

$$\frac{H_{c1}}{H_{c2}} = \frac{\ln\kappa}{2\kappa^2} \qquad (6-4)$$

where κ for a uniaxial superconductor takes the two values given by equation (3-78) for the two field orientations. Using H_{c2} values from Welp et al. and the measured values for H_{c1}, κ values from equation (6-4) are found to be $\kappa^{ab}=400$ and $\kappa^c = 60$. It was mentioned in Ch. 3 that the value of $\kappa = \frac{1}{\sqrt{2}} \sim 0.71$ separated the magnetic characteristics of a superconductor into type I and type II. The extremely large κ values found in $YBa_2Cu_3O_{7-\delta}$ indicate the superconductivity to be extremely type II in nature. The thermodynamical critical field H_c, calculated from equation (3-66) using the estimates of κ, were found to be approximately 11 kG to 14 kG.

The magnetic penetration depth can be estimated from the values of H_{c1} using the anisotropic equations in (3-81). From the values of H_{c1} and the estimates of κ, the penetration depth was found to be anisotropic having the values of 8200 Å or 970Å. Measurements by muon spin rotation[135,136] (μSR) give values of λ as ~1400 Å for fields in the a,b plane and 5000-8000 Å for fields along c, in rough agreement with the result obtained from the H_{c1} values. As stated in Ch. 3 the geometry of the anisotropic penetration depths is somewhat complicated. There are different

penetration depths defined for the field along the c axis and in the a,b plane because the supercurrent direction responsible for shielding the field is different. The geometry of the various field directions, current directions and field penetrations are illustrated in Figure 6-6. For fields in the c direction, the penetration in the b direction is determined by the shielding currents flowing in the a direction, while for fields along the b direction the penetration in the c direction is also determined by the currents flowing in the a direction. Since both penetration depths are influenced by the currents flowing in the a direction, the two penetration depths should have equal characteristics so that

$$\lambda_{a,b}^{c} = \lambda_{c}^{b,a}. \qquad (6-5)$$

However, for fields along the b direction the penetration depth along the a direction is determined by the currents flowing in the c direction. The anisotropic currents that flow along the c axis make this penetration depth anisotropic so that

$$\lambda_{a,b}^{c} \neq \lambda_{a,b}^{b,a}. \qquad (6-6)$$

Thus when the field is along the a,b plane it is the penetration depth in the a,b plane that is anisotropic and not the penetration depth along the c direction. The penetration depths influenced by the smaller equilibrium shielding currents along the c direction (which will be denoted as j_c) have the larger value of 8200 Å while the penetration depths influenced by the larger equilibrium

125

Figure 6-6
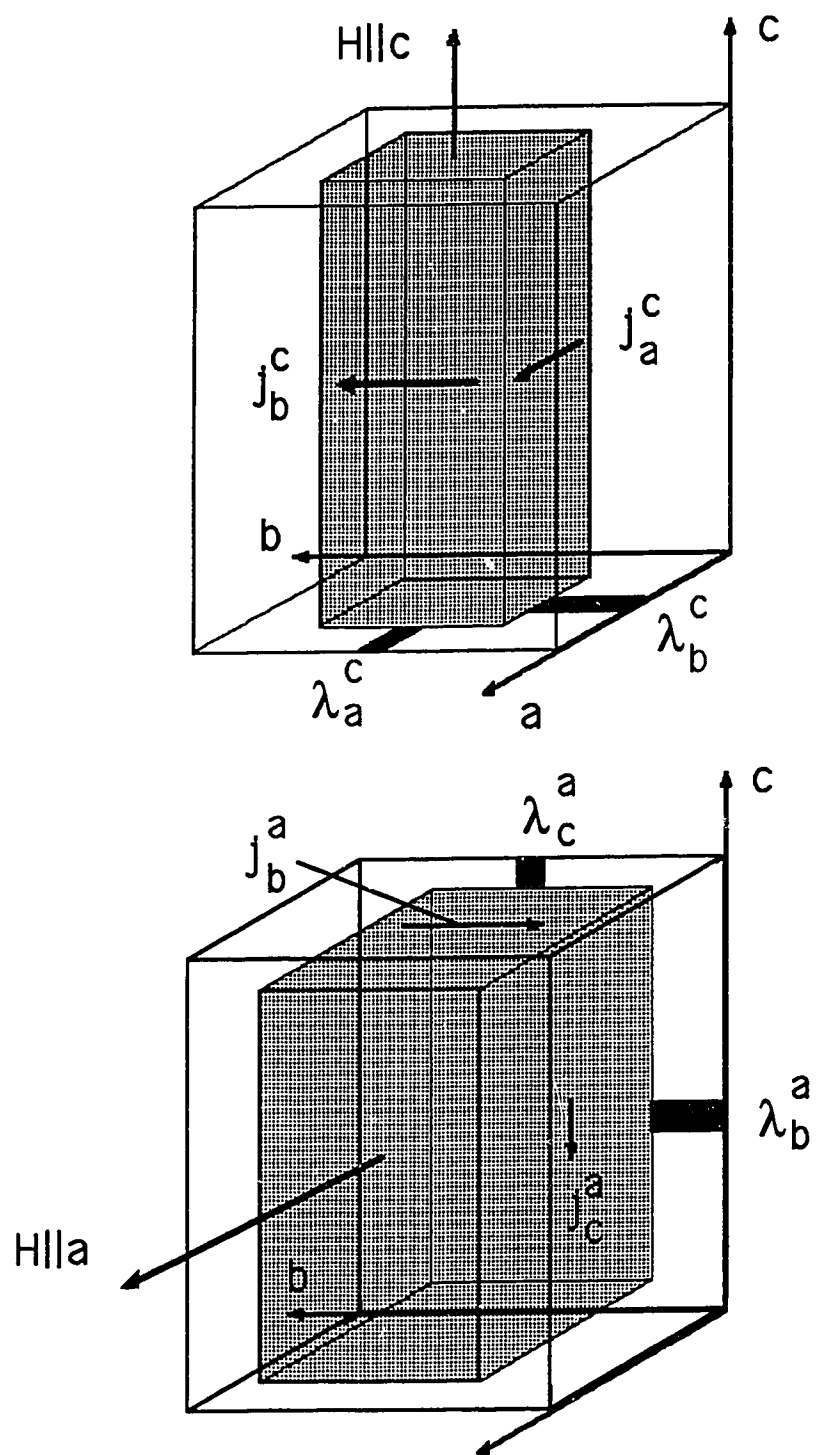
shielding currents along a,b (which will be denoted as $j_{a,b}$) have the smaller value of 970 Å. The equilibrium supercurrent density flowing at H_{c1} can be roughly estimated from Maxwell's equation by taking the approximation $\frac{H_{c1}}{\lambda} \sim \frac{dH}{dx} = \frac{4\pi}{c} j$. The results in Table 6-2 show a large anisotropy of as much as a factor of 50, demonstrating that even perfect samples with no pinning sites would contain "hard" and "easy" axes for supercurrent flow. The intrinsic anisotropy in maximum supercurrent flow is qualitatively consistent with the effective mass anisotropy inferred from the critical fields.

In summary, the lower critical field of $YBa_2Cu_3O_{7-\delta}$ at low temperatures was found to be anisotropic, with the anisotropy being roughly consistent with those from the upper critical field within the anisotropic GL theory. The estimated magnetic penetration depth had the anisotropic values of 970 Å when influenced by $j_{a,b}$ and 8200 Å when influenced by j_c. These values are in agreement with the anisotropy found from direct measurements of λ from muon spin rotation[135,136]. These large penetration depths may lead to sample size limitations of the shielding and Meissner effects in thin film and polycrystalline samples. Also due to the extremely large values of κ found in this material, the normal cores of the vortices are often assumed to occupy only a small volume fraction of the magnetic fields and screening currents, and thus will not be significant when performing calculations. Recently Hao and Clem[137] have raised

Table 6-2

	H ∥ c	H ∥ a,b
H_{c1}	690 ± 90 G	120 ± 14 G
H_{c2}	1220 kG	6470 kG
$\xi_{a,b}$	16 Å	
ξ_c	3 Å	
κ	60	400
$\lambda_{b,a}$	970 Å	8200 Å
λ_c		970 Å
$J_{c1,b,a}$	6×10^7 A/cm^2	1×10^7 A/cm^2
$J_{c1,c}$		1×10^6 A/cm^2

questions regarding such assumptions since the extremely large λ values which suggests small screening currents may result in a small energy contribution of similar magnitude to that from the normal core. Finally, the anisotropic values found for ξ and λ indicate that a single vortex in this material is ellipsoidal in shape. Such anisotropy in the characteristic lengths and the equilibrium shielding currents may result in unusual effects to be observed in the magnetic behavior of this superconducting material.

Temperature dependence of flux entry and H_{c1}

To further investigate the characteristics of the lower critical fields in the $YBa_2Cu_3O_{7-\delta}$ system, the experiment discussed in the previous section can be extended to determine the H_{c1} values at higher temperatures[138]. Such an experiment is useful since the measurements can then be compared to the temperature dependence of H_{c1} for traditional superconductivity, to see if there is any unusual behavior arising from the anisotropic electronic structure.

The crystals available for this experiment had much improved sample quality compared to the those used in the previous experiments. The crystals were larger and were platelike in shape. Typical dimensions of these new samples were approximately 1 to 3 mm along the side and approximately 0.5 mm thick, where the c axis was found to be along the 0.5 mm dimension. The crystal used for this experiment had closely spaced <110> type twin boundaries. Figure 6-7 is a zero field

Figure 6-7

YBa₂Cu₃O₇₋δ
H||c 1 G
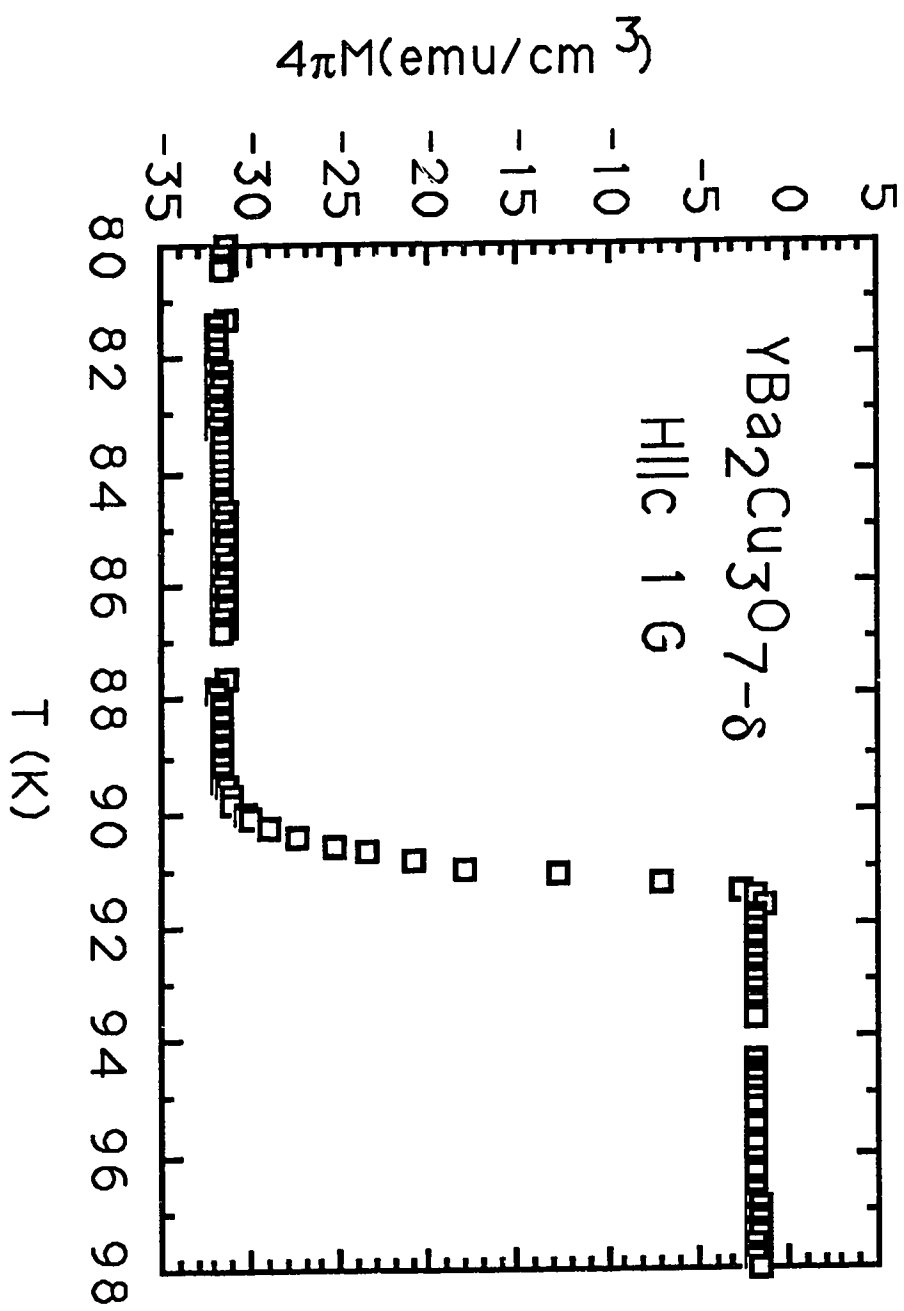
cooled shielding curve for one of the samples measured in a field of 1 G along the c axis. The superconducting transition is found to be sharp with $T_c > 92$ K and a transition width ≤ 1 K. The transitions found in these new samples are slightly higher and much sharper than those observed in the previous samples, indicating the better quality of these new samples. Their improved quality and larger size made them the logical choice for performing the temperature dependent H_{c1} measurements.

The platelike shape of the crystal proved useful when measuring H_{c1} for fields in the a,b plane. The new samples are very thin along the c axis making demagnetization effects in these samples much smaller compared to the previous samples for H//a,b. However when the field is oriented along the c axis, the determination of H_{c1} becomes extremely sensitive to the severe demagnetization factors that arise from the platelike nature of the crystals. With such strong demagnetization effects arising for this field orientation, any errors in the demagnetization factors (such as from the sample corners) may severely influence the determination of H_{c1}. Further, it has been suggested that the large demagnetization effects may cause unusual field distributions to occur in the sample, such as the local fields being directed in the a,b plane even when the applied field is along the c axis[139]. Due to the severe demagnetization effects occurring for H//c, the measurements involved in this experiment have been performed only for fields in the a,b plane, where demagnetization factors are small (n ~ 0.1).

The magnetization measurements were taken using a commercial Quantum Design SQUID magnetometer in fields up to 400 G, for temperatures ranging from 6 to 85 K in 5 K steps. Detailed magnetization measurements were taken on a fine grid of 1 to 5 G for low fields and 10 to 50 G, once the curvature in the magnetization became evident. A deviation plot of ΔM vs H was again constructed from the measured magnetization curves by subtracting a linear fit to the low field magnetization data. The entry field was chosen as the first applied field where an observable trend in the deviation of the magnetization from linearity occurred.

The magnetization curve of the single crystal of $YBa_2Cu_3O_{7-\delta}$ for H//ab is shown in Figure 6-8 at 10, 45 and 80 K. The magnetization curves were found to gradually deviate from linearity at all temperatures due to flux pinning present in the sample. At low temperatures this deviation from linearity is slight and difficult to observe. As the temperature is increased, the deviations become sharper and more evident as the pinning energy decreases and thermal energy increases. Figure 6-8 also shows that the magnitude of the entry field is found to decrease with increasing temperature.

The linear region of the magnetization curves, shown in Figure 6-8, is found to superimpose on one another illustrating the relative stability of the slope and the demagnetization factor with changing temperature. The demagnetization factor, which only depends upon the geometry of the sample, is temperature

132

Figure 6-8
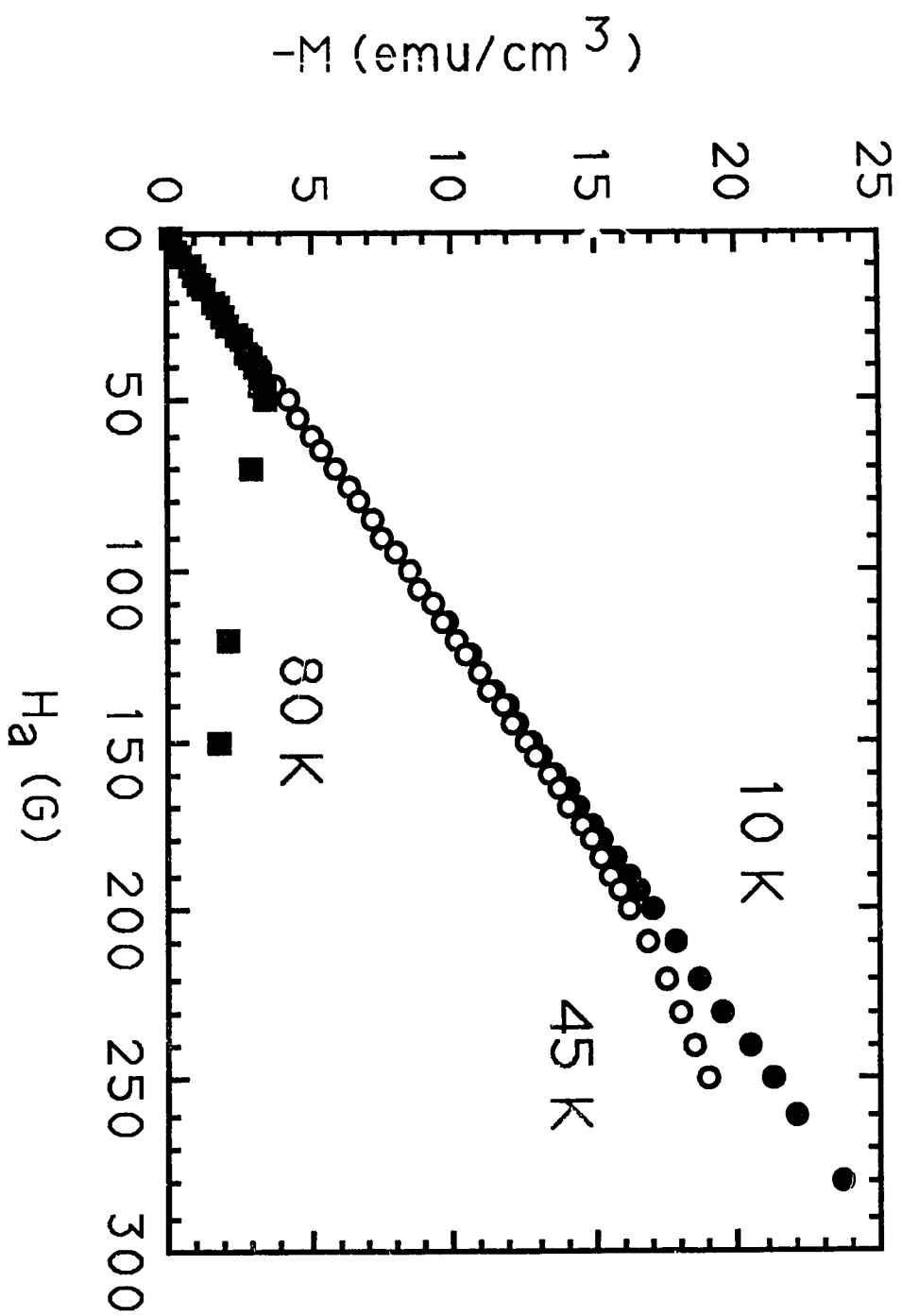
independent as expected. The variation with temperature in the slope of the linear part of the magnetization curves was less than 0.5 % at low temperatures (T < 70 K). At higher temperatures, the error in the slope increased due to the decreasing number of points in the linear portion of the magnetization curve that could be used to obtain a least squares fit. However even for these temperatures, the slope varied by less than 2% from the low temperature value. Demagnetization constants were obtained experimentally from the slope of the magnetization curve using equation (6-2). Using the calculated slope of the magnetization curves, the demagnetization factor for the sample was found to be approximately 0.1. This value is in agreement with the calculated values of n ~ 0.09 obtained from ellipsoid approximations[140].

Figure 6-9 shows the deviation curves from Figure 6-8, after the linear fit extrapolation of the low field data was subtracted from them. The number of points used to obtain the fit was determined by gradually increasing the number of points in the fit until the standard deviation in the fit started to rise dramatically. This occurred in the field range where the magnetization deviates from linearity. Approximately 60 to 70 % of this maximum number of points were used for the linear fit in order to keep the deviation in M from affecting the linear fit. Neither the fit to the linear region nor the value of H_e were found to be very sensitive to the number of points chosen to fit the linear region. For example at 10 K, a fit with the points up to 70 G or 170 G resulted in only a 25% change in the standard deviation of the linear fit,

Figure 6-9
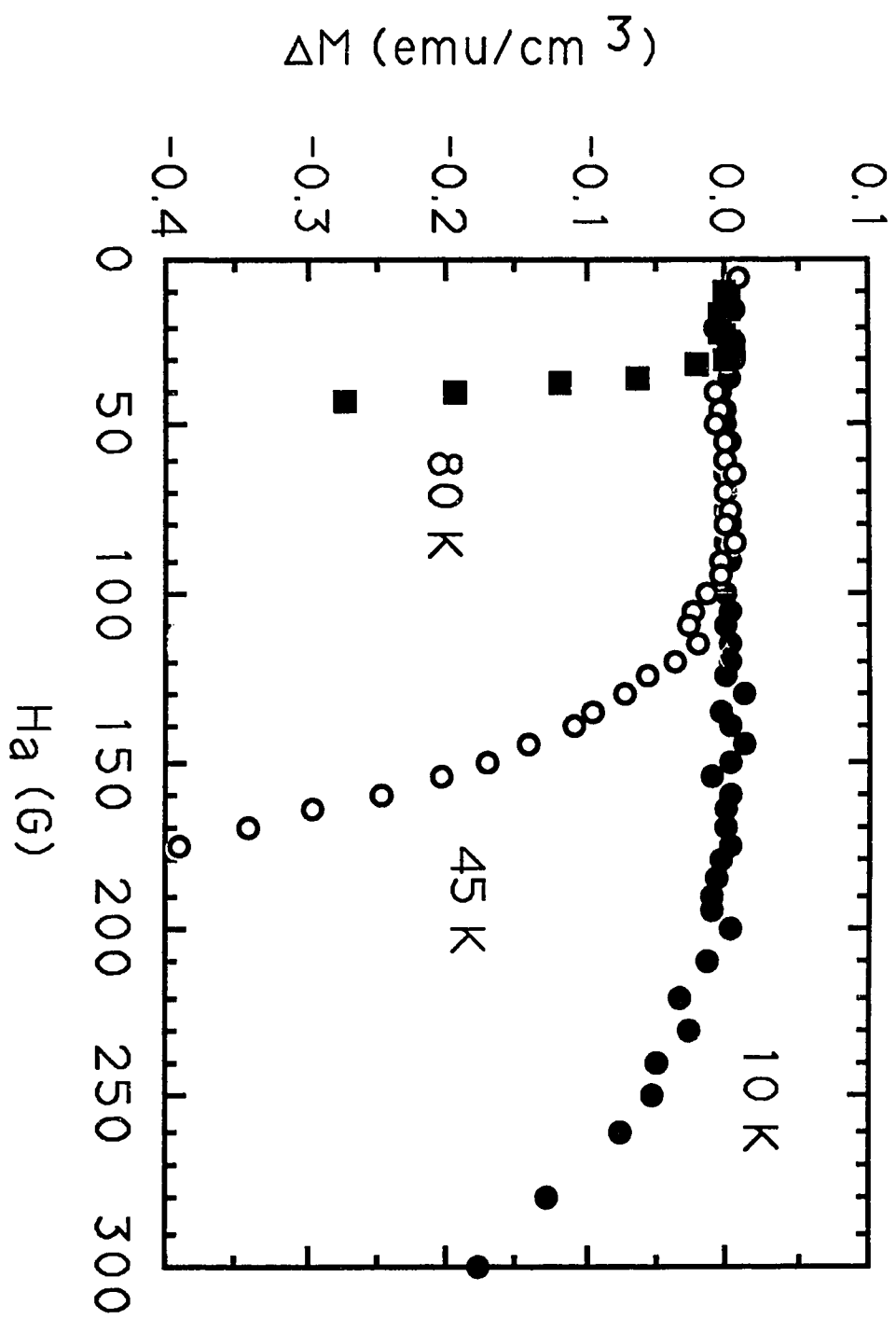
less than 0.5 % change in the slope $\Delta M/\Delta H$ and no observable change in the estimated value of H_e. Figure 6-9 reveals that H_e actually occurs at much lower fields than those inferred directly from the magnetization curve in Figure 6-8. Beyond the entry field ΔM falls much more sharply with increasing temperature, again indicating weaker flux pinning at higher temperatures.

The values of H_{c1} at several temperatures, calculated from the entry fields using equation (6-3) are shown in Figure 6-10. Error bars are given to represent the error in determining the entry field H_e from Figure 6-9. At higher temperatures, the error in determining H_e decreases, because the decreased pinning strength allows the flux to enter the sample more easily, and ΔM shows a more rapid downturn at H_e. From GL theory, equations (3-36) and (3-65) together state that the temperature dependence of H_{c1} should be linear near T_c. Near T_c, the temperature dependence of H_{c1} from this experiment is found to be linear, in agreement with the GL theory, with a slope of -2.4 G/K. Lower critical fields obtained from M vs T measurements by Krusin Elbaum et al.[23] found similar linearity in $H_{c1}(T)$ for T > 40 K with a temperature dependent slope of ~3 G/K for H//a,b. At lower temperatures where GL equations are no longer valid, the expected behavior of H_{c1} can be determined from equation (3-65) and the empirical temperature dependence of λ, which approximately has the form[84]

$$\lambda(T) = \lambda(0)\left[1 - \left(\frac{T}{T_c}\right)^4\right]^{-\frac{1}{2}}. \qquad (6\text{-}7)$$

Figure 6-10
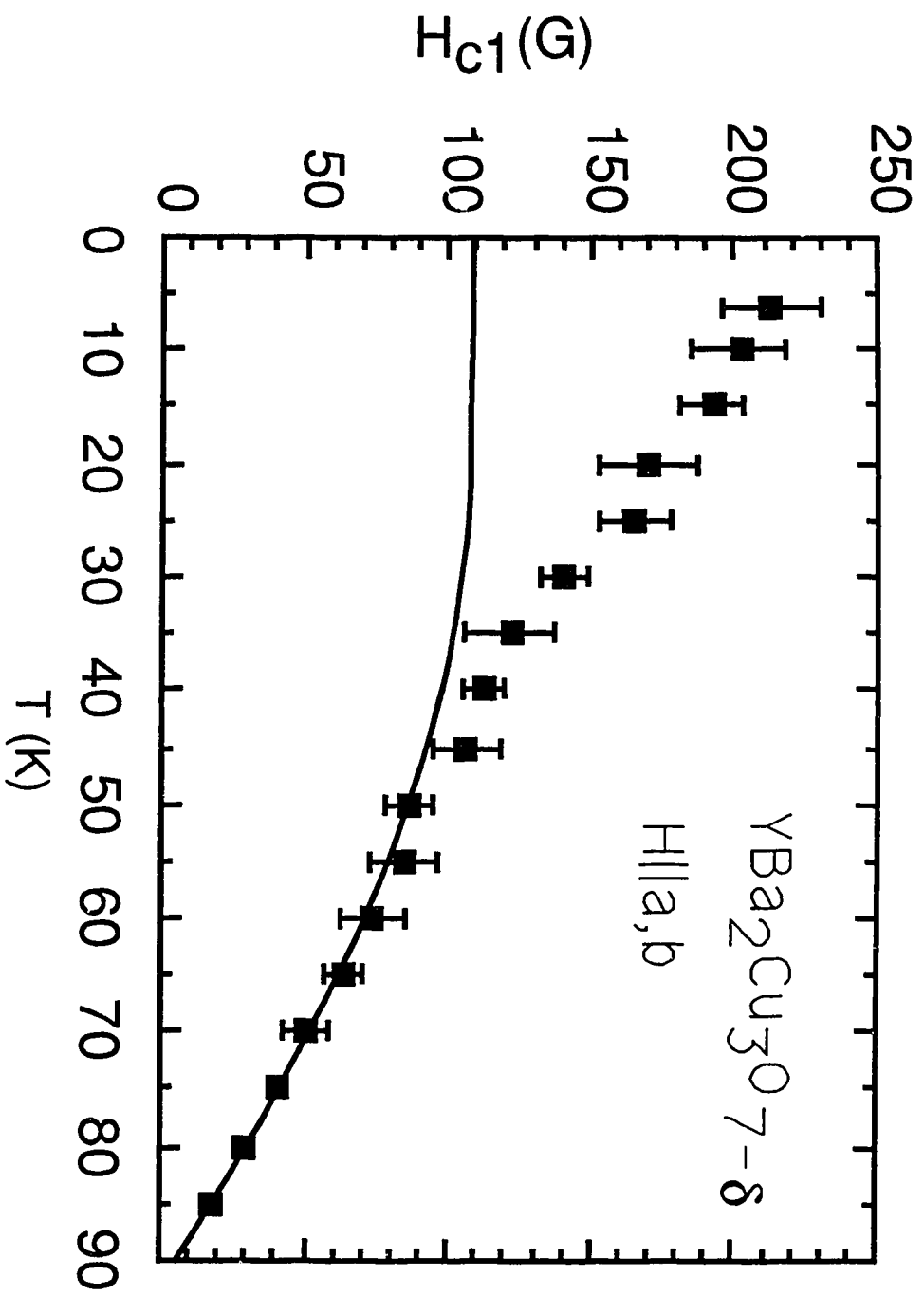
If κ is assumed to be temperature independent, the temperature dependence of H_{c1} can then be written as

$$H_{c1}(T) = H_{c1}(0)\left[1 - \left(\frac{T}{T_c}\right)^4\right].\qquad(6\text{-}8)$$

The fit of this form to the measured value of H_{c1} at $T = 65$ K for H//ab is shown by the solid line in Figure 6-10. At high temperatures, the fit to the data is quite good but below 40 K there is a definite departure of the data from conventional behavior. The measured values of H_{c1} for H//ab at low temperatures do not saturate but instead increase steadily with decreasing temperature.

Such linear behavior in the temperature dependence of H_{c1} has been observed through other measurements[23,141], such as those from M vs T measurements by Krusin Elbaum et al.[23] for $T > 40$ K, as shown in Figure 6-11 (a), to obtain $H_{c1}(T)$. However, several other measurements of H_{c1} have shown anomalous behavior in the H_{c1} temperature dependence at intermediate temperatures between 0 K and T_c (usually near $\frac{1}{2}T_c$).

Measurements which found such anomalous behavior, such as those by Ströbel et al.[142] shown in Figure 6-11(b), were found to fit well to two saturating curves[142-145]. Finally, temperature dependent H_{c1} measurements by Sridar et al.[146] using RF penetration have found saturation at low temperatures, similar to the behavior expected from a traditional superconductor. Yet, their value for H_{c1} at low temperatures was found to be similar in

138

Figure 6-11

(a)
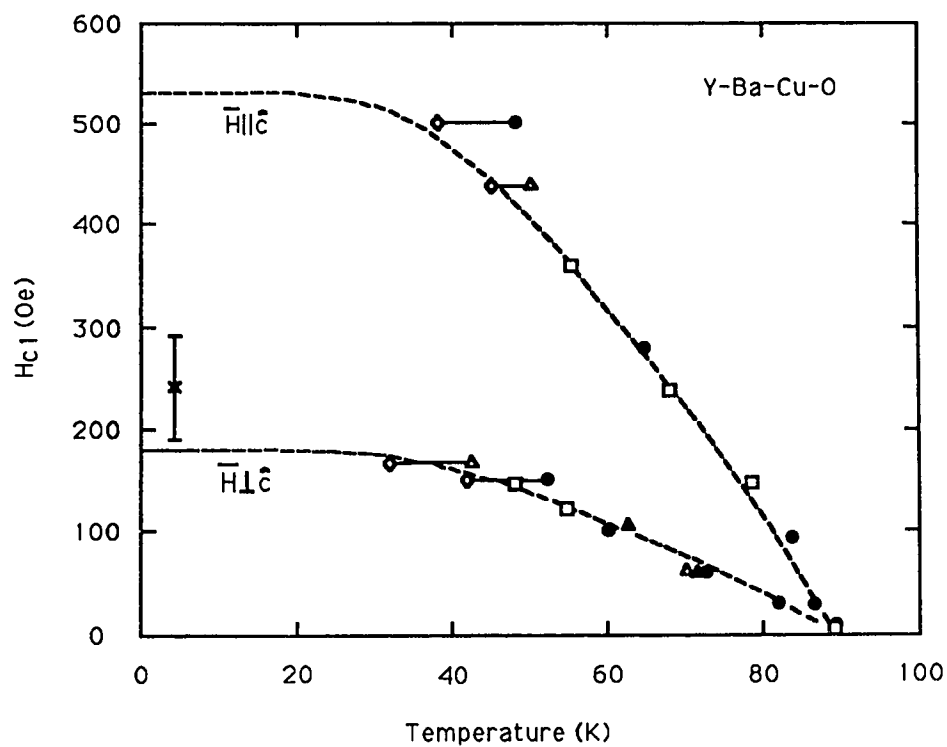
(b)
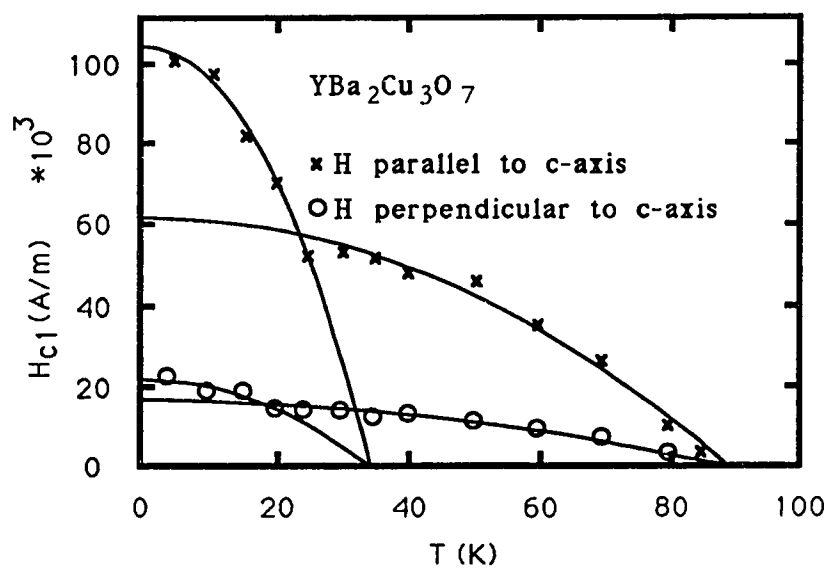
magnitude to many of the other measurements that found unusual temperature dependent behavior in their values of H_{c1}. The temperature dependence of H_{c1} resulting from the different types of measurements has been listed in Table 6-3. Table 6-3 illustrates the degree of disagreement that is present regarding the temperature dependence of H_{c1} at present.

Using equation (3-65), and assuming κ to be temperature independent, an anomalous temperature dependence of H_{c1} can be directly related to an anomalous temperature dependence of λ. Experiments that have been performed to observe the magnetic penetration depth directly in $YBa_2Cu_3O_{7-\delta}$, such as μSR[135,136], RF penetration[146] and zero field cooled magnetization measurements[147] have shown the temperature dependence of λ to follow basically the behavior of traditional superconductivity. Figure 6-12, in which the temperature dependence of λ obtained from μSR measurements by Pümpin et al.[136] is plotted, shows that it follows the expected empirical form, with $\frac{1}{\lambda^2}$ saturating at low temperatures. Thus the standard temperature dependence of λ conflicts with the anomalous temperature dependence found in many H_{c1} measurements, including the present one. The conflicting behavior observed in different the H_{c1} measurements, as well as between H_{c1} and λ measurements suggests that further research is necessary to establish the true behavior and to understand the reasons for the discrepancies.

140

Table 6-3

H_{c1} in $YBa_2Cu_3O_{7-\delta}$:

Measurement	$H_{c1}^c(G)$	$H_{c1}^{ab}(G)$	T dep
MvsH:			
Strobel et al.[139]	1190	220	double curve
Adrian et al.[141]	2500	600	double curve
Kartsovnik et al.[138]	>1400	200	linear
MvsT:			
Krusin-Elbaum et al.[23]	550	200	linear to 40K
RF penetration:			
Sridar et al.[143]	- -	220	saturation at low T

FIGURE 6-12
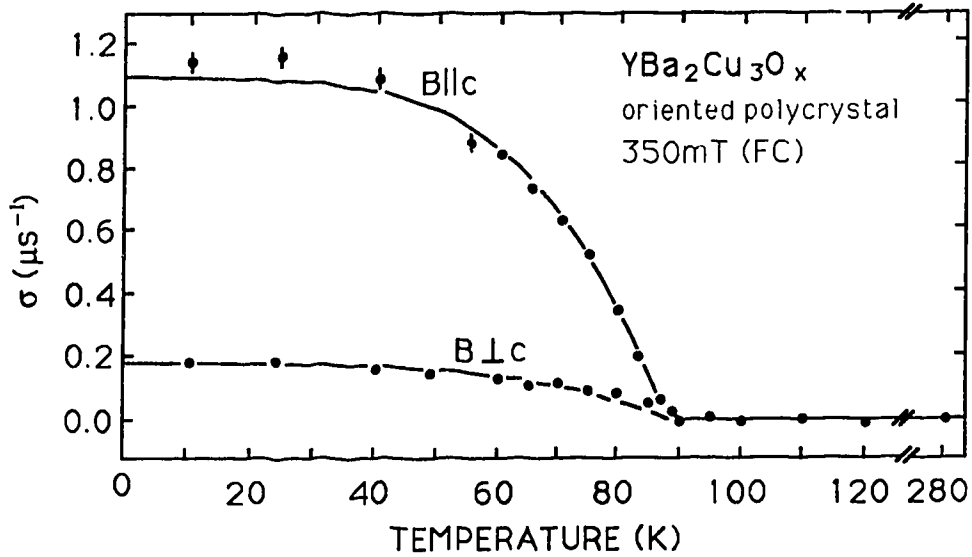
σ - μSR depolarization rate

According to Pümpin et al. [Ref 134], the field distribution in a superconductor is given as

$$\langle \Delta B^2 \rangle = 2\sigma^2/\gamma_\mu^2$$

where γ_μ is the gyromagnetic ratio of the muon.

The magnetic penetration depth is related to this field distribution by

$$\lambda^4 = 0.0371\Phi_0^2/\langle \Delta B^2 \rangle$$

where Φ_0 is the flux quantum. Thus the temperature dependence of σ can be related to the temperature dependence of $1/\lambda^2$.

The a-b anisotropy and twin boundary effects on the measurements of H_{c1}

As discussed in Ch. 2, the selective occupation of the O1 oxygen sites in the unit cell of $YBa_2Cu_3O_{7-\delta}$ gives rise to two characteristics unique to this material, namely the existence of CuO chains along the b axis, and the formation of <110> type mirror twin boundaries. The existence of the CuO chains raises questions with regard to their effects on the normal and superconducting properties of the $YBa_2Cu_3O_{7-\delta}$ system. Band structure calculations[51] indicate that conductivity comes from both the unique CuO chains, as well as the CuO_2 planes more commonly found in the high T_c superconductors. Transport and magnetic measurements on oxygen deficient samples of $YBa_2Cu_3O_{7-\delta}$[148,149], found T_c to decrease with decreasing oxygen content in the O1 site, indicating that the CuO chains influenced the superconductivity of the $YBa_2Cu_3O_{7-\delta}$ material. However, due to the existence of domains separated by <110> twin boundaries[24,34-37], where the a and b axes interchanged between the domains, measurements could not be taken uniquely along the a and b axes. Thus experiments performed to investigate directly the effects from the CuO chains have been extremely rare. Recently however, single crystals consisting of a single domain and no twin boundaries have become available through certain post-growth annealing procedures[38]. Transport measurements on these untwinned crystals have found the normal state conductivity along the b axis (or CuO chains) to be lower than along the a axis, indicating

metallic behavior from the CuO planes[151,152]. Such crystals were ideal for investigating the nature of the contribution of the CuO chain to the superconductivity in the $YBa_2Cu_3O_{7-\delta}$ system.

In this section measurements of the temperature dependence of the entry field and lower critical field in untwinned single crystals of $YBa_2Cu_3O_{7-\delta}$ are presented[150]. This section will cover results regarding the a-b anisotropy in the lower critical field and compare them to results from other investigations on the effect of CuO chains on superconductivity. The temperature dependence of H_{c1} for the untwinned crystal will be compared with that of the twinned crystal to observe if there are any effects from the twin boundaries on the measurements of H_{c1}. Finally measurements of H_{c1} taken on a crystal that has twins along only one of the <110> directions will be discussed.

The measurements in this section involve three single crystals of $YBa_2Cu_3O_{7-\delta}$, each having different twin characteristics. All the samples were platelike with the c axis normal to the plate and with dimensions approximately 1.0 - 3.0 mm in the plane of the plate and approximately 0.5 mm thick. The $H_{c1}(T)$ measurement of one of the crystals, which had twin boundaries running along both <110> type directions (designated hereafter as the dual boundary sample) was discussed in the previous section. Another crystal had twins running along only one of the <110> directions (designated as the single boundary sample). The difference in the twin boundary arrangement between the dual and single boundary samples is shown schematically in

144

Figure 6-13

Dual Boundary Sample
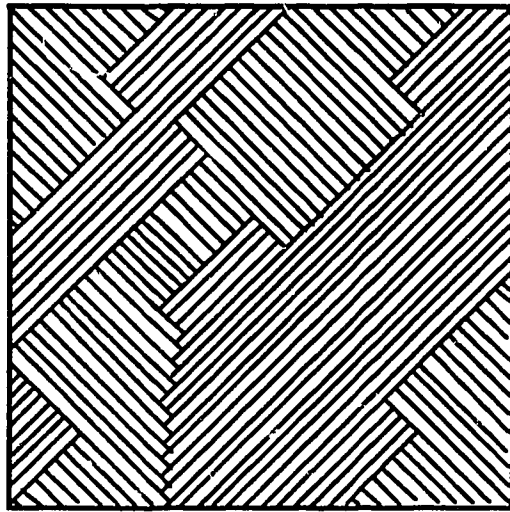
Single Boundary Sample
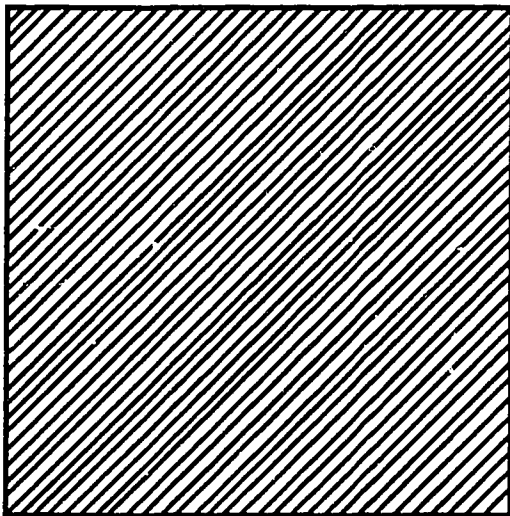
Figure 6-13. The third crystal had the twins mechanically removed through the special annealing process[38]. All the crystals were of high quality with $T_c \geq 92$ K and had sharp resistive and inductive transitions.

The untwinned crystal was obtained through a post-growth annealing process developed by U. Welp[38]. The basis for this annealing process comes from that fact that the b axis, in $YBa_2Cu_3O_{7-\delta}$, is slightly longer than the a axis due to oxygens present at the O1 site. If a force is applied along one of the crystallographic axes in the a,b plane, it becomes more favorable for the chains to be oriented perpendicular to that force, as shown in Figure 6-13. Thus the twins were found to be mechanically removable by annealing the sample above 390° C with pressure applied along one of the crystallographic directions in the a,b plane, such that the O1 sites all occupied the axis perpendicular to the applied force. After the detwinning procedure, these samples were found to be twin free as determined by both X-ray diffraction and polarized light microscopy[38].

Detailed magnetization measurements were taken using a Quantum Design SQUID magnetometer for fields in the a,b plane, at temperatures from 5 to 85 K in 5 K steps. At each temperature, after zero field cooling, the magnetization was sampled at 1 to 5 G intervals at low fields and 10 to 100 G intervals once the curvature in the magnetization became evident. Magnetic deviation curves were again found from the magnetization curves in order to observe the entry field with the maximum possible resolution. To

Figure 6-14

de-twinned $YBa_2Cu_3O_{7-\delta}$

⬤ Cu1 sites   ◯ O1 sites

Applied
Force

b

a

Removal
of Twins
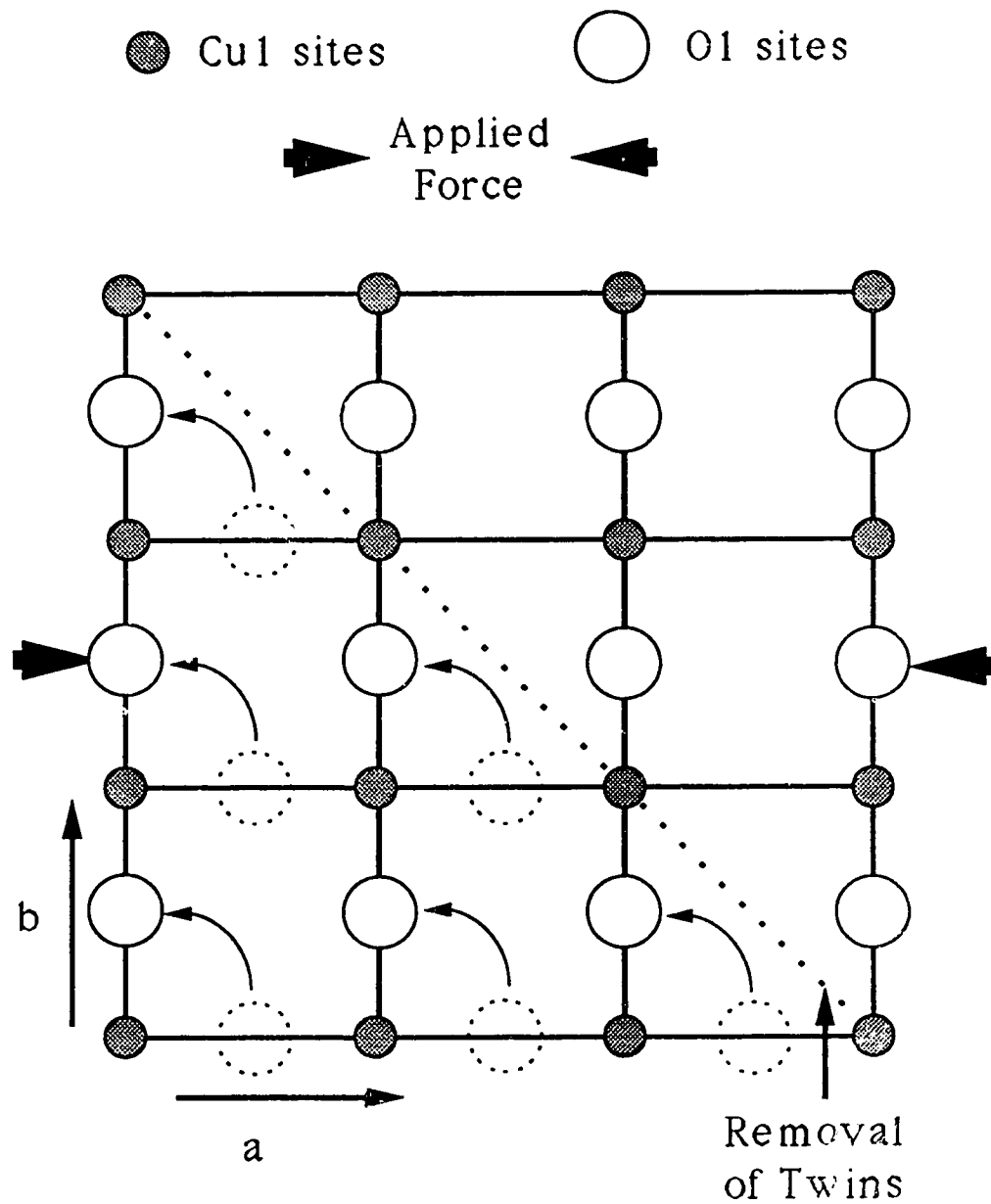
observe how misalignment affected the value of the demagnetization factor, a sample was purposely tilted so that the field was 5° off the a,b plane. The magnetization was measured at low fields for this tilted sample and compared to the magnetization measurements made when the sample was not tilted. For both 40 and 70 K, the magnetization when the sample was tilted 5° was found to significantly increase compared to the case when it was aligned, as shown in Figure 6-15. The demagnetization factor for the tilted measurements gave a value of n = 0.35, at both temperatures, as compared to the low values of n = 0.08 for the aligned measurements. Thus for these platelike samples, the results indicate a very sensitive demagnetization factor to field misalignment off the a,b plane.

Magnetization curves for the untwinned sample at 10 K, 45 K and 80 K are shown in Figure 6-16 (a). The initial linear portions of the three curves again superimpose upon one another, confirming the expected temperature independence of the Meissner slope and the demagnetization factor. The demagnetization factor, n, calculated from the slope of the Meissner region of the magnetization curves for the three crystals ranged from 0.06 to 0.15 depending on crystal shape and field orientation. Corresponding values of n obtained from ellipsoidal approximations[140] ranged from 0.05 to 0.2, in good agreement with those measured from the slope. The low values of n, and their agreement with estimates based on ellipsoidal approximations, indicate that the samples were aligned with the

Figure 6-15
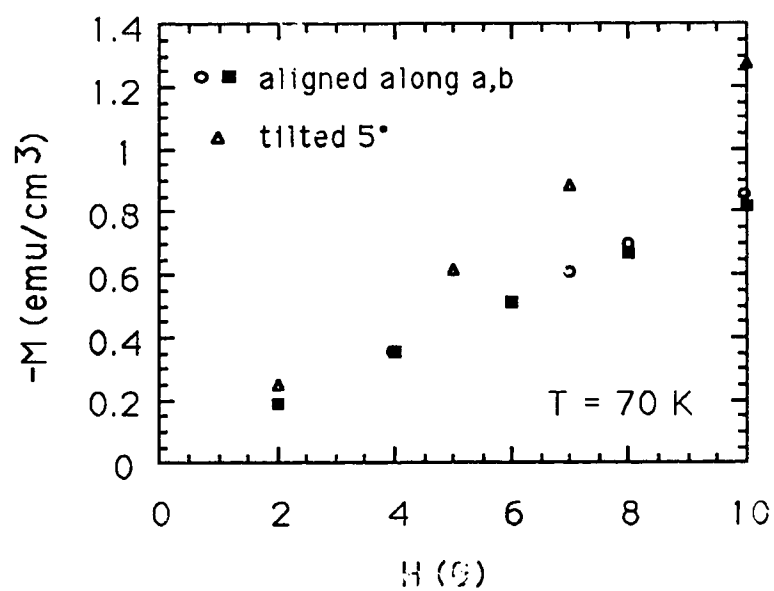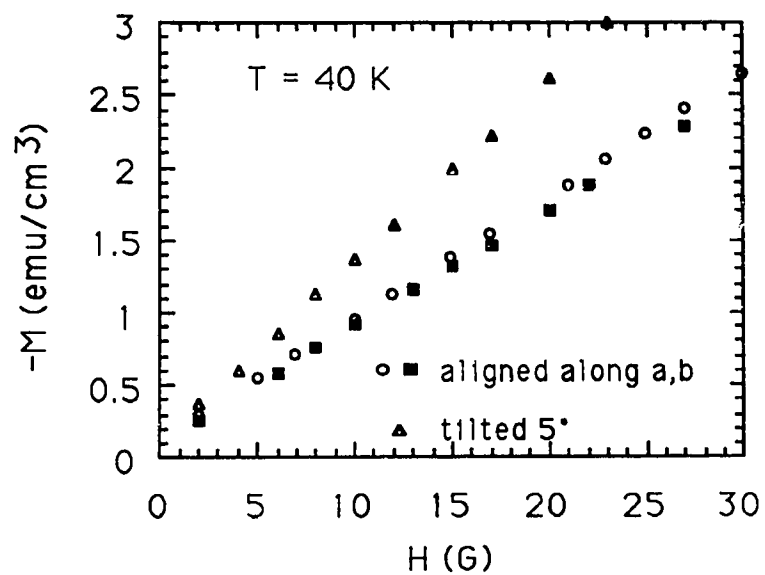
Figure 6-16
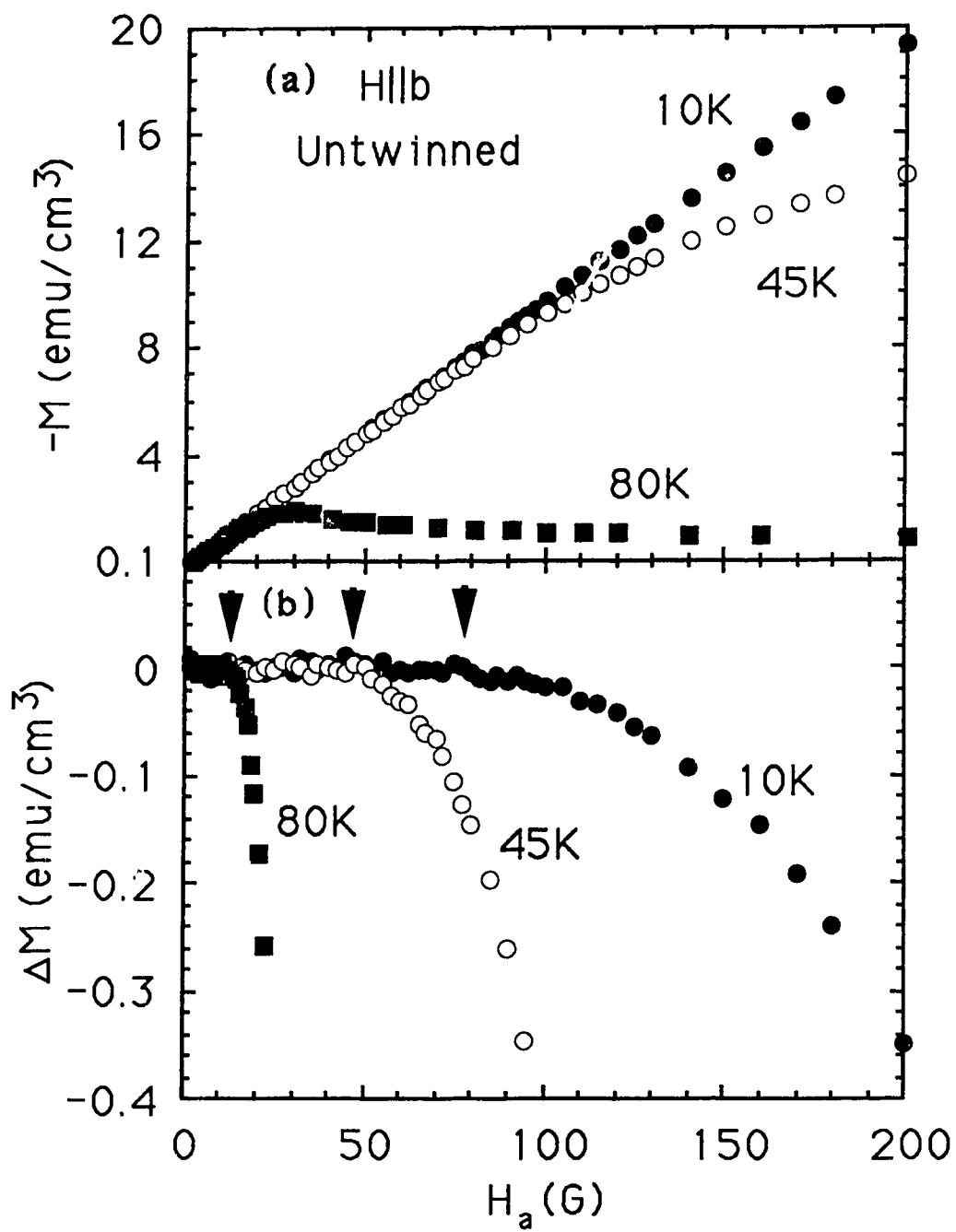
field in the a,b plane, and that the effect of sample shape on the measurements of the magnetization and flux entry is minimal. Figure 6-16 (b) shows the deviation curves corresponding to the magnetization curves in Figure 6-16 (a). The field of first flux entry is chosen as the field where the magnetization first deviates from linearity, resulting in a nonzero value of the difference ($\Delta M \neq 0$). Figure 6-16 (b) shows sharper deviations from linearity with increasing temperature, reflecting decreased pinning strength.

The temperature dependence of H_{c1} for the dual boundary and untwinned samples is shown in Figure 6-17. Figure 6-17 shows measurements of H_{c1} for H//a, H//b and one angle approximately 45° between a and b (H45ab) for the untwinned crystal. At all temperatures for all three field orientations, H_{c1} is found to be lower for the untwinned crystal than for the dual boundary crystal. Furthermore, all three field orientations in the untwinned sample are found to have a similar temperature dependence of H_{c1}. This similarity of H_{c1} with different field orientation indicates that there is no significant a-b anisotropy in the lower critical field. Upper critical field measurements by Welp et al.[38], taken on an untwinned sample of $YBa_2Cu_3O_{7-\delta}$ found similar temperature dependent slopes of H_{c2} near T_c for H//a and H//b, in agreement with the H_{c1} results. This lack of anisotropy in both H_{c1} and H_{c2} indicates that there is no significant a-b anisotropy in the superconductivity coming from the CuO chains.

Figure 6-17

152
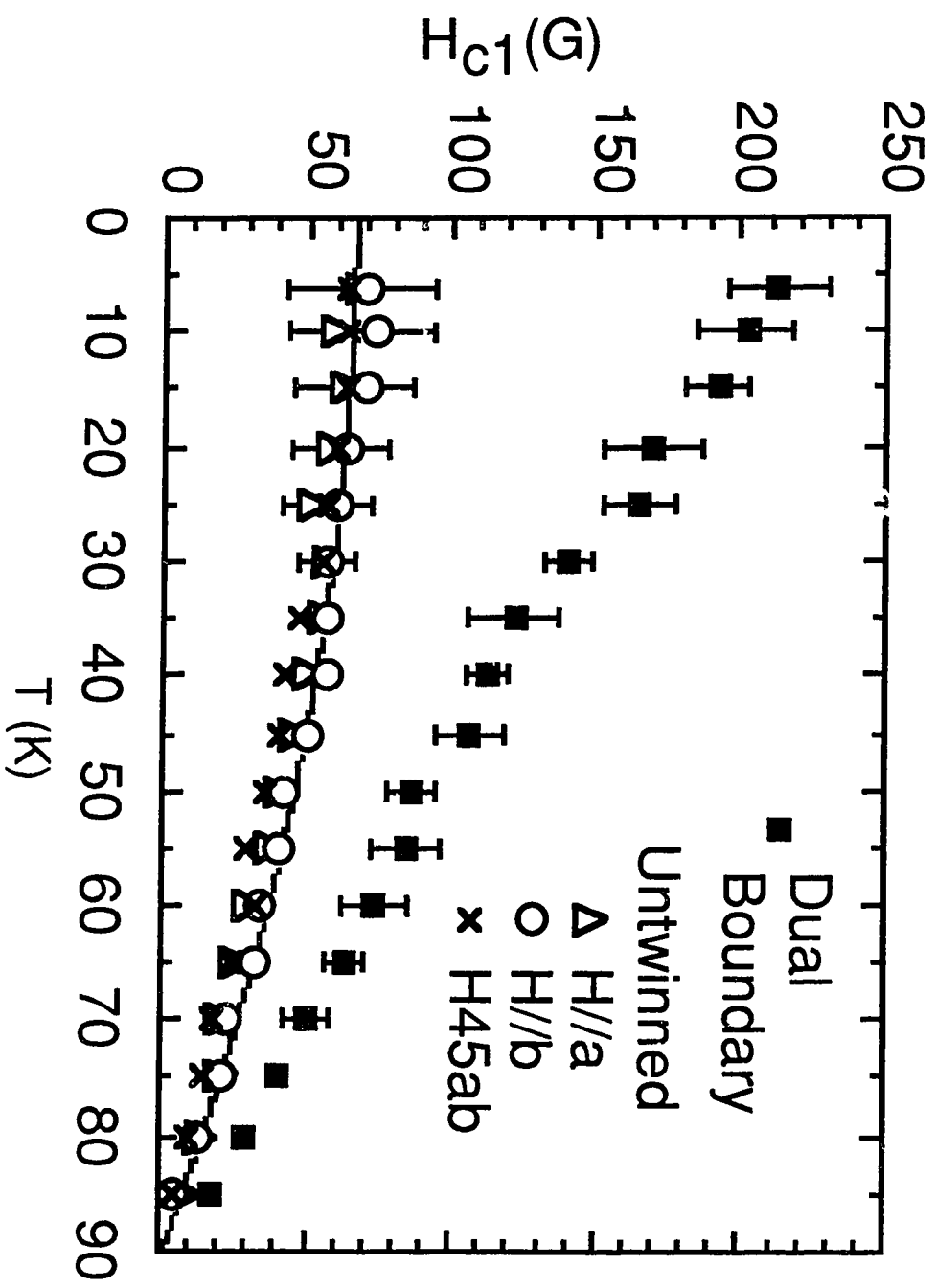
Further evidence comes from infra-red measurements by Schlesinger et al.[155] who have found similar values for the energy gap along the a and b axis. Also, critical field measurements on oxygen deficient $YBa_2Cu_3O_{7-\delta}$ samples by Vandervoort et al.[154] have found that although T_c decreases with oxygen depletion in the CuO chains, no significant change in the anisotropy of either $\frac{H_{c2}^{a,b}}{H_{c2}^{c}}$ or $\frac{H_{c1}^{a,b}}{H_{c1}^{c}}$ was found as compared to the fully oxygenated crystals. This indicates that the effective mass anisotropy does not change in spite of the severe depopulation of the oxygens in the chains and suggests that the chains play no role in the superconducting properties beyond affecting T_c by providing charge carriers to the CuO planes. This viewpoint is consistent with the absence of H_{c1} anisotropy observed in the a,b plane due to the chains. Decoration experiments by Dolan et al.[155] found slight differences in the vortex spacing along the a and b axis observed from their decoration pattern. It is not certain whether the anisotropy observed in their pattern reflects a characteristic of the superconductivity or the orthorhombicity of the crystal structure. They inferred that if there is an a-b anisotropy in the material, their results give a mass anisotropy of 1.3:1. The corresponding anisotropy for H_{c1} would be 1.14:1, a value which falls within the resolution of the data. Thus all these measurements agree that anisotropic superconductivity due to the CuO chains, if it exists, is small.

153

For the untwinned sample the magnitude of H_{c1} is found to saturate at low temperatures as shown in Figure 6-17. Figure 6-18 shows the temperature dependence of the average value of H_{c1} for all three field orientations. The temperature dependence of $H_{c1}(T)$ is found to be well described by a $(1-(T/T_c)^2)$ dependence as shown by the figure. This $(1-(T/T_c)^2)$ temperature dependence is similar to the $(1-(T/T_c)^4)$ temperature dependence often used to fit μSR[135,136], RF penetration depth[146] and low field magnetization data[147]. Thus the temperature dependence of H_{c1} for the untwinned sample is qualitatively in good agreement with direct measurements of λ. Quantitatively, assuming that $\kappa \sim 100$ and taking the low temperature value of $H_{c1}(0)=70$ G, an estimate of $\lambda^2 \sim 10^{-9}$ cm^2 is derived using equation (3-81). Estimates of the penetration depths for fields in the a,b plane and along the c axis[135,136,146,147] are approximately 1300-1400 Å and 5000-8000 Å respectively, giving a product of approximately 10^{-9} cm^2, in reasonable agreement with the estimate of λ^2 from H_{c1}.

The saturating behavior of H_{c1} at low temperatures is different from the steadily increasing behavior found for the dual boundary sample, shown in Figure 6-17. Whereas the untwinned sample gave qualitative and quantitative agreement with λ measurements, the dual boundary sample gave much more unusual results. The differences in the two crystals indicated that there may be some sample dependent feature that may be affecting the measurements of H_{c1}. Recently, the existence of twin

154

Figure 6-18

155
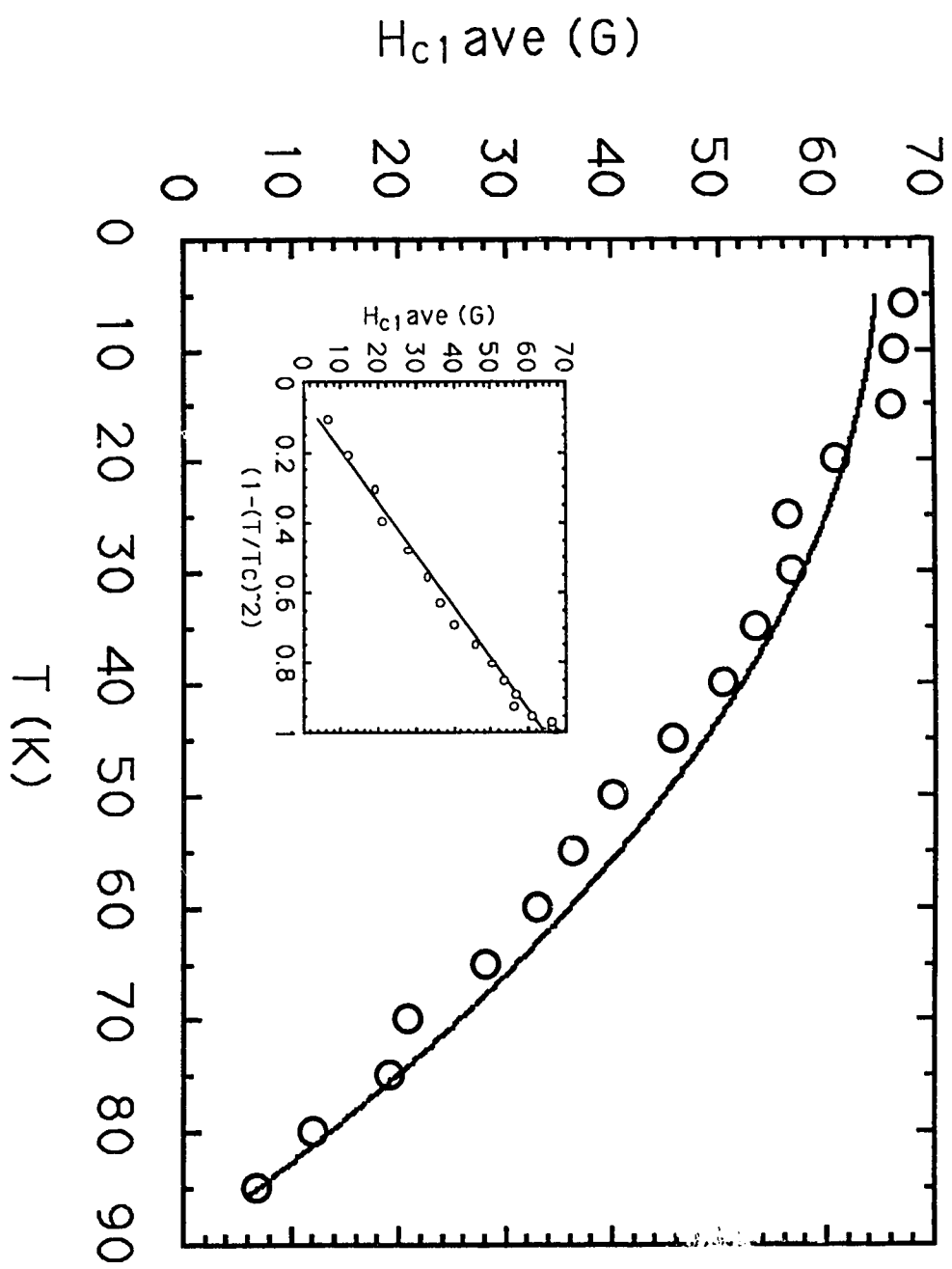
boundaries in $YBa_2Cu_3O_{7-\delta}$ has been found to have several interesting effects on superconducting properties. Magnetization measurements have shown a difference for the magnetic field parallel and perpendicular to the twin planes[156]. Transport measurements[122], magnetic torque measurements[123] and magnetic relaxation measurements[124] have found significant flux pinning by the twin boundaries for H parallel to the twin planes. Theoretical and experimental papers have discussed the effect of twin planes on the upper critical field[157-160]. Thus one possibility for the difference observed in the H_{c1} measurements for the two crystals may be effects arising from the existence of twins in the dual boundary sample.

To observe the dependence of H_{c1} on twin boundary orientation, magnetization measurements were done on the single boundary sample with fields parallel, perpendicular, and 45° from the twin planes[150]. The results of these measurements are shown on Figure 6-19. As shown in Figure 6-19, when the field is parallel to the twin planes, H_{c1} agrees with the untwinned sample. However when the field is perpendicular or at an angle 45° to the twin planes, H_{c1} increases to near that of the dual boundary sample. If the twin boundaries are regions of easy flux entry, the magnetic flux would enter the sample through the twins before it enters the bulk, thus decreasing the entry field. Such an effect would occur most readily for H in the twin planes. The similarity of H_{c1} for H parallel to the twin planes and for the untwinned crystal indicates that twin planes are not planes of easy flux entry.

Figure 6-19

157
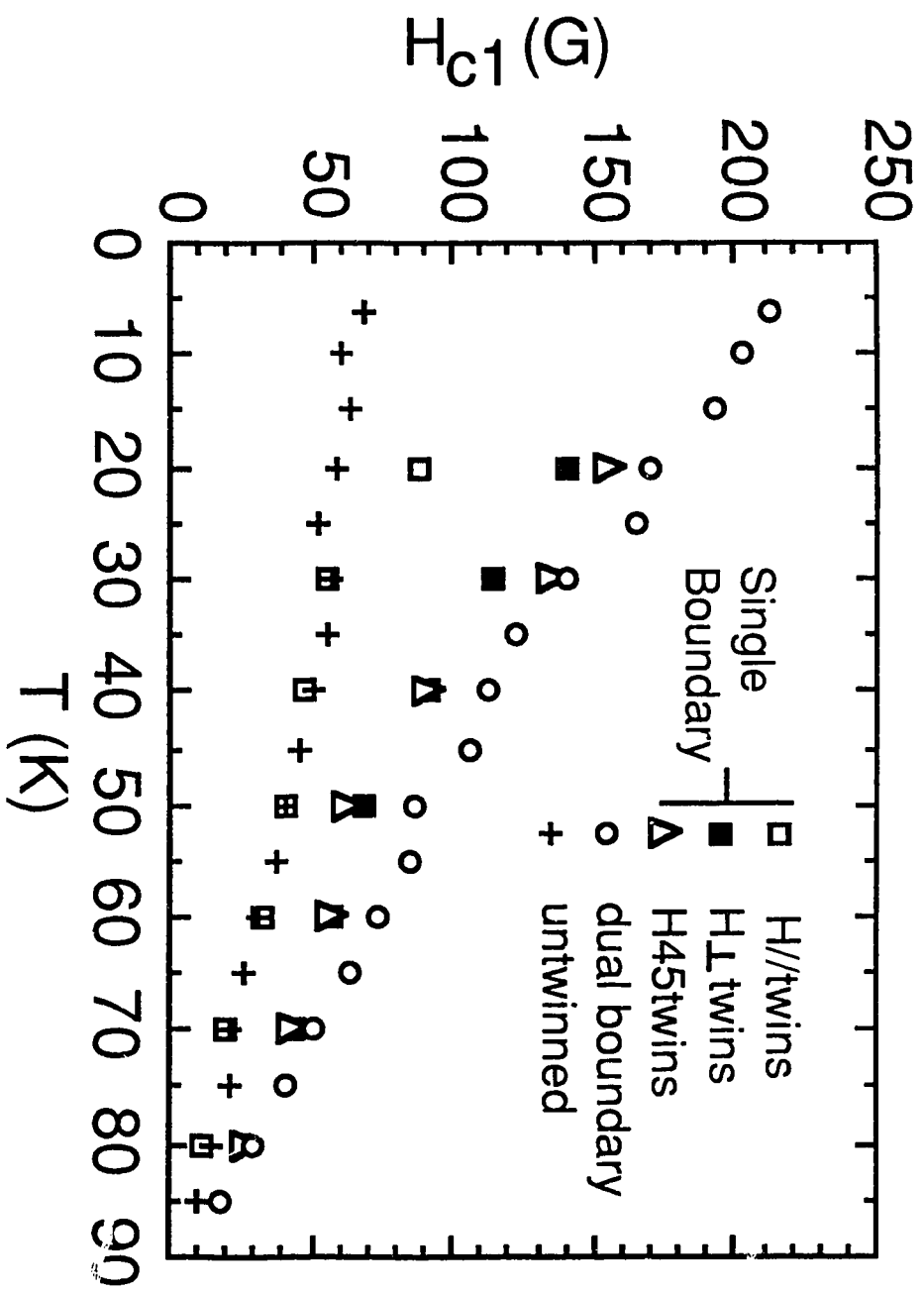
This conclusion agrees with earlier measurements of pinning in twinned and untwinned samples by Welp et al[120].

Now whether or not flux pinning by twin boundaries can explain the enhanced entry fields in the dual boundary sample will be considered. Increased flux pinning due to the twin boundaries would not only increase the apparent entry field but would also broaden the deviation curve for H beyond the entry field, shown by Figure 3-4. Figure 6-20 compares the behavior of the deviation curve ΔM, for fields parallel, perpendicular and 45° to the twin boundaries for 30 K and 70 K in the single boundary sample. While the entry field for H parallel to the twins is lower than for H perpendicular and 45° to the twins, the relative shape of the curves is similar for all three field orientations. In fact, if the deviation curves for H parallel to the twins for 30 K and 70 K are shifted up in field by 60 G and 20 G respectively, they fit the deviation curves for the other field orientations quite well. This indicates that the difference observed in the entry fields is not caused from a significant difference in flux pinning at low fields. At high fields, Kwok et al.[122], Gyorgy et al.[123] and Liu et al.[124] found pinning to be strongest for H parallel rather than perpendicular to the twins. If this behavior held at low fields as well, pinning would increase the value of the entry field for H parallel to the twin boundaries, exactly opposite to the effect observed from the H_{c1} measurements. Thus the enhanced values of the entry field for H perpendicular to or 45° from the twin boundaries are not consistent with expected pinning behavior.

158

Figure 6-20

159
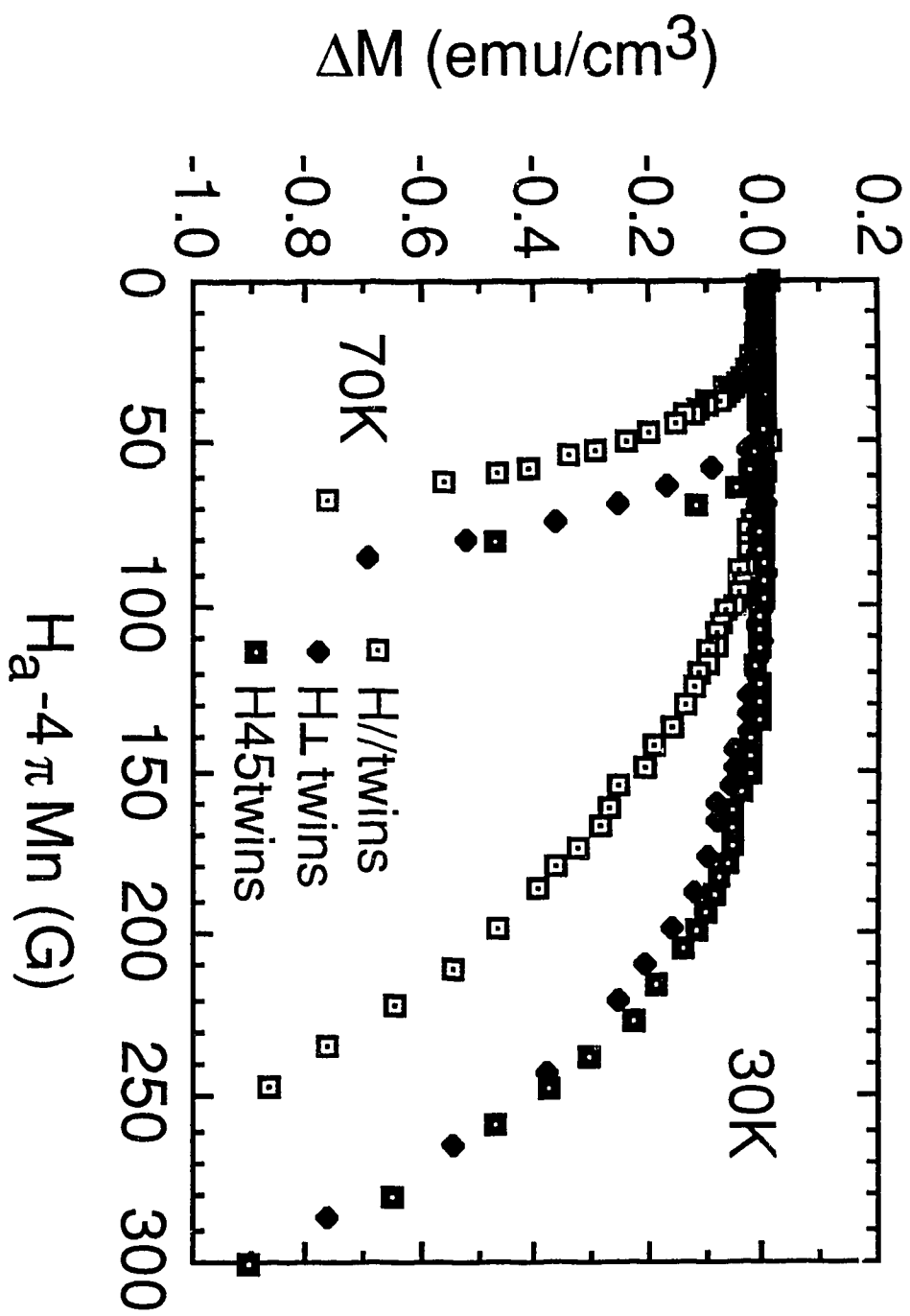
The increase in H_{c1} is interpreted as an increase in the creation energy of an isolated vortex when it crosses a twin plane. When the field is parallel to the twin boundaries, the vortex can avoid the twins by lying between adjacent boundaries. For the intersecting geometry the energy incre   would depend on the volume of the vortex-twin boundary   ersection. This feature leads to the approximate equality of H_{c1} for the perpendicular and 45° orientation of the field in the single boundary sample by the following argument. The volume of the twin boundary-vortex intersection depends on the density of twin boundaries encountered along the vortex line and on the intersection area of the vortex with each twin boundary. A graphical representation of a vortex intersecting the twin boundaries is given by Figure 6-21. At an arbitrary angle θ, the density of twin boundaries along the vortex is $\cos\theta/L$, where L is the perpendicular distance between twin boundaries. The intersection area is $\pi l^2/\cos\theta$, where l is the characteristic length describing the size of the vortex, either ξ or λ, depending on whether the extra energy is contained in the core or in the circulating vortex currents and the associated magnetic field. The product of these two factors is independent of angle, so long as the vortex is not parallel or nearly parallel to the twin boundaries. One consequence of this interpretation is an observable dependence of H_{c1} on the density of twin boundaries. As no method has yet been found of controlling the twin boundary density in single crystals, this prediction has not been tested.

The dependence of H_{c1} on the presence of twin boundaries

Figure 6-21

$l' = l/\cos\theta$

$L' = L/\cos\theta$

suggests one reason for the large discrepancies among H_{c1} measurements, ranging from approximately 100 to 600 G at T=0 K for $H//ab$[23,141-146]. In addition, the saturation of H_{c1} at low temperatures in the untwinned crystal removes an obvious qualitative discrepancy in the behavior of the penetration depth measured by μsr[135,136], RF penetration[146], the temperature dependence of M in low fields[147], and the entry field from isothermal magnetization[142-145]. The present measurements of H_{c1} for the untwinned crystal are qualitatively and quantitatively in reasonable agreement with the direct measurements of the penetration depth. Furthermore, the present measurements of H_{c1} in the untwinned crystal are qualitatively similar to those recently reported for $Y_2Ba_4Cu_8O_{16}$, an orthorhombic compound without twins[61]. Martinez et al. found that H_{c1} measured from the entry field saturated at low temperature according to a $(1-(T/T_c)^2)$ dependence, showed no a-b anisotropy and attained a value of 44 G at low temperature. The similarity of these features to those of untwinned $YBa_2Cu_3O_{7-\delta}$ crystals suggests that the superconducting properties for fields in the a-b plane are similar for these two closely related structures.

In summary, detailed magnetization measurements show that there is an increase in H_{c1} in twinned samples over untwinned samples at all temperatures. In the untwinned crystals no a-b anisotropy is found in H_{c1}. H_{c1} is increased in twinned samples only when the vortex intersects the twin boundary. The similarity in the deviation curves beyond the entry field for all

162

three field orientations in the single boundary sample suggests that this enhancement is not due to flux pinning. Finally, the tendency to saturation of H_{c1} at low temperatures removes important qualitative and quantitative discrepancies of this measurement with other estimates of λ.

A recent experiment has been conducted by Welp et al.[162] to determine upper and lower critical fields from high field, temperature dependent magnetization measurements near T_c on fully oxygenated and oxygen deficient samples using a method suggested by Hao and Clem[137]. These measurements had two advantages over other low field measurements of H_{c1}. Firstly since their measurements were done at high temperatures and in fields where magnetization is reversible, these measurements are not influenced by flux pinning effects. Furthermore, since these measurements are close to T_c the field has almost fully penetrated the sample such that demagnetization effects are minimal. The temperature dependent slope of H_{c1} near T_c in a twinned, fully oxygenated sample was found to be -2.7 G/K, in agreement with the -2.4 G/K found in the slope of the dual boundary crystal. Furthermore the temperature dependence of H_{c1} for the oxygen deficient sample was found to fit a $(1-(T/T_c)^2)$ dependence similar to that found for the untwinned sample. Measurements of H_{c1} on an untwinned sample using this method to look for a-b anisotropy and twin effects have not yet been done. However the initial results show good agreement between the two types of measurement.

163

Ch. 7 <u>Summary and Conclusion</u>

The research discussed in the preceding chapters has given insight regarding the nature of the superconductivity and its anisotropy in the high T_c superconductor $YBa_2Cu_3O_{7-\delta}$. Both the intrinsic parameters, such as the upper and lower critical fields and non-intrinsic parameters such as flux pinning and critical magnetization currents have been observed to be anisotropic. The anisotropy of these parameters reflects the anisotropy of the electronic structure from the CuO_2 layers.

The critical magnetization currents within a single crystal of $YBa_2Cu_3O_{7-\delta}$ have been found to be much higher than those observed for polycrystalline samples. These higher critical current values have increased the possibility of using this material for application purposes. Also the measurements have illustrated the importance of improving the connectivity of the grain boundaries in the polycrystalline materials in order to increase their critical currents. The critical magnetization currents were found to be anisotropic indicating anisotropy in the flux pinning energies. The anisotropy in the flux pinning may come from the anisotropic vortex geometry or anisotropic flux pinning sites (such as the twin boundaries). Finally, fast neutron irradiation on the single crystals had been shown to further improve the critical currents suggesting this method to be one possibility for increasing the critical current capabilities of this material.

The investigations of the intrinsic superconducting properties have shown both upper and lower critical field to be anisotropic. The anisotropy in H_{c1} and H_{c2} are well described by the anisotropic GL theory and reflect the crystal structure anisotropy from the CuO_2 planes. The large GL parameter estimated from these measurements indicate this material to be an extreme type II superconductor. The strong anisotropy shown in the characteristic lengths indicate a complex geometry of the vortex structure compared to isotropic superconductors. Also, the strong anisotropy observed in the magnetic penetration depth indicates the existence of hard and easy axes for supercurrent flow.

The availability of untwinned single crystals of $YBa_2Cu_3O_{7-\delta}$ made it possible to investigate both the a-b anisotropy and the twin boundary effect on the measurements of H_{c1}. Magnetization measurements on the untwinned sample showed that neither the magnitude nor the temperature dependence of H_{c1} significantly differed for H//a, H//b and H45a,b. The similarity in the measurements of H_{c1} for three field orientations suggests that the CuO chains along the b direction are not contributing to the anisotropy in the superconductivity.

The temperature dependence of H_{c1} for the untwinned sample shows saturation at low temperatures, in basic agreement with penetration depth measurements. Quantitatively, the magnitude of λ^2 estimated from these H_{c1} measurements agrees with those found from penetration depth measurements. The qualitative and quantitative agreement between the H_{c1}

measurement for the untwinned sample and penetration depth measurements resolves the discrepancy previously found between the two types of measurements. Finally, the difference in the measured value of H_{c1} for the twinned and untwinned sample reveals the possibility of twin boundary effects on the lower critical field.

Measurements taken on the single domain crystal have shown the twin boundaries to increase the measured value of H_{c1}. The increase in H_{c1} was observed to occur when the vortices intersected the twin boundaries but not for vortices parallel to the twin boundaries. The similarity in the deviation curve beyond the entry field for H//twins, H perpendicular to the twins and H 45° to the twins indicate that flux pinning is not the cause of this increase. One possibility for this difference is an increase in the vortex nucleation energy due to the presence and orientation of twins.

The results obtained in this research suggest possible future experiments to be performed. The study of twin boundary effects in H_{c1} measurements can be extended by investigating the dependence of H_{c1} on the twin density. Such an experiment requires precise control of the twin boundary spacing within the single crystals, which may be possible with precise annealing procedures. Another experiment, which can be done with the present available samples, is to investigate the a-b anisotropy of λ for an untwinned sample, using low field temperature dependent magnetic shielding measurements. The anisotropy of the critical

magnetization currents can be further investigated by applying the anisotropic Bean Model extensions given by Gyorgy et al.[163] and Sauerzopf et al.[131], to magnetization measurements on samples having different dimensions. The final obvious proposal is the research towards obtaining larger, higher quality samples for characterization.

Bibliography:

1. H. K. Onnes, Lieden Comm. 120B, 122B, 124C (1911).

2. J. F. Schooley, W. R. Hosler, and M. L. Cohen, Phys. Rev. Lett. 12, 474 (1964).

3. J. G. Bednorz and K. A. Müller, Z. Phys. B, B64 189 (1986).

4. M. K. Wu, J. R. Ashburn, C. J. Torng, P. H. Hor, R. L. Meng, L. Gao, Z. J. Huang, Y. Q. Wang and C. W. Chu, Phys. Rev. Lett. 58, 908 (1987).

5. H. Maeda, Y. Tanaka, M. Fukutomi and T. Asano, Jpn. J. Appl. Phys. 27, L209 (1988).

6. Z. Z. Sheng and A. M. Hermann, Nature 32, 55 (1988).

7. R. J. Cava, B. Batlogg, J. J. Krajewski, R. Farrow, L. W. Rupp Jr, A. E. White, K. Short, W. F. Peck and T. Kometani, Nature 332, 814 (1988).

8. Y. Tokura, H. Takagi and H. Uchida, Nature 337, 345 (1989).

9. H. Takagi, S. Uchida, K. Kitazawa, S. Tanaka, Jpn. J. Appl. Phys. 26, L123 (1987).

10. J. D. Jorgensen, H.-B. Schüttler, D. G. Hinks, D. W. Capone II, K. Zhang, and M. B. Brodsky, Phys. Rev. Lett. 58, 1024 (1964).

11. R. J. Cava, B. Batlogg, J. J. Krajewski, R. Farrow, L. W. Rupp Jr, A. E. White, K. Short, W. F. Peck and T. Kometani, Nature 332, 814 (1988).

12. D. G. Hinks, B. Dabrowski, J. D. Jorgensen, A. W. Mitchell, D. R. Richards, Shiyou Pei, and Donglu Shi, Nature 333, 836 (1988).

13. W. A. Little, Phys. Rev. 134-A, 1416 (1964).

168

14. V. L. Ginzburg, Phys. Lett. 13, 101 (1964).

15. J. E. Hirsch and D. J. Scalapino, Phys. Rev. Lett. 56, 2732 (1986).

16. M. Inoue, T. Takemori, K. Ohtaka, R. Yoshizaki and T. Sakudo Sol. St. Comm. 63, 3622 (1987).

17. Z. Ye, H. Umezawa, and R. Teshima, Sol. St. Commun. 74, 1327 (1990).

18. D. Kaiser, F. Holtzberg, M. F. Chisolm and T. K. Worthington, J. Cryst. Growth 85, 593 (1987).

19. L. F. Schneemeyer, J. V. Waszczak, T. Siegrist, R. B. van Dover, L. W. Rupp, B. Batlogg, R. J. Cava and D. W. Murphy, Nature 328, 601 (1987).

20. J. Z. Liu, G. W. Crabtree, A. Umezawa and Li Zongquan, Phys. Lett. A. 121, 305 (1987).

21. U. Welp, W. K. Kwok, G. W. Crabtree, K. G. Vandervoort and J. Z. Liu, Phys. Rev. Lett. 62, 1908 (1989).

22. A. Umezawa, G. W. Crabtree, J. Z. Liu, T. J. Moran, S. K. Malik, L. H. Nunez, W. L. Kwok, and C. H. Sowers, Phys. Rev. B 38, 2843 (1988).

23. L. Krusin Elbaum, A. P. Malozemoff, Y. Yeshurun, D. C. Cronemeyer, and F. Holtzberg Phys. Rev. B 39, 2936 (1989).

24. Y. Zhu, M. Suenaga, Youwen Xu, R. L. Sabatini and A. R. Moodenbaugh, Appl. Phys. Lett 54, (1989).

25. J. D. Jorgensen, D. G. Hinks, H. Shaken, Dabrowski, B. W. Veal, A. P. Paulikas, L. J. Nowicki, G. W. Crabtree, W. K. Kwok,

A. Umezawa, L. H. Nunez, B. D. Dunlap, C. U. Segre and C. W. Kimball, Physica B 156-157, 877 (1989).

26. W. K. Kwok, G. W. Crabtree, A. Umezawa, B. W. Veal, J. D. Jorgensen, S. K. Malik, L. J. Nowicki, A. P. Paulikas and L. Nunez, Phys. Rev. B 37 106 (1988).

27. G. W. Crabtree, J. Z. Liu, A. Umezawa, W. K. Kwok, C. H. Sowers, S. K. Malik, B. W. Veal, D. J. Lam, M. B. Brodsky and J. W. Downey, Phys. Rev. B 36, 4021 (1987).

28. Y. Yeshrun and A. P. Malozemoff, Phys. Rev. Lett. 60, 2022 (1988).

29. C. P. Bean, Phys. Rev. Lett. 8, 250 (1962).

30. M. A. Beno, L. Soderholm, D. W. Capone II, D. G. Hinks, J. D. Jorgensen, J. D. Grace, I. K. Schuller, C. U. Segre and K. Zhang, Appl. Phys. Lett. 51, 57 (1987).

31. J. J. Capponi, C. Chaillout, A. W. Hewat, P. Lejay, M. Marezio, N. Nguyen, B. Raveau, J. L. Soubeyroux, J. L. Tholence and R. Tournier, Europhysics Letters 3, 1301 (1987).

32. J. E. Greedan, A. H. O'Reilly and C. V. Stager Phys. Rev. B 35, 8770 (1987).

33. Y. LePage, T. Siegrist, S. A. Sunshine, L. F. Schneemeyer, D. W. Murphy, S. M. Zahurak, J. V. Waszczak, W. R. McKinnon, J. M. Tarascon, G. W. Hull and L. H. Greene, Phys. Rev. B 36, 3617 (1987).

34. D. J. Eaglesham, C. J. Humphreys, N. McN. Alford, W. J. Clegg, M. A. Harmer, and J. D. Birchall Appl. Phys. Lett. 51, 457 (1987).

35. S. Iijima, T. Ichihashi, Y. Kubo, and J. Tabuchi, Jpn. J. Appl. Phys. 26, L1478 (1987).

36. A. Brokman, Sol. St. Comm. 64, 257 (1987).

37. H. Schmid. E. Burkhardt, E. Walker, W. Brixel, M. Clin, J.-P. Rivera, J.-'.. Jorda, M. François and K. Yvon, Z. Phys. B 75, 305 (1988).

38. U. Welp, M. Grimsditch, H. You, W. K. Kwok, M. M. Fang, G. W. Crabtree, and J. Z. Liu, Physica C 161, 1 (1990).

39. J. P. Rice, D. M. Ginsburg, M. W. Rabin, K. G. Vandervoort, G. W. Crabtree and H. Claus, Phys. Rev. B 41, 6532 (1990).

40. D. M. Ginsburg, Physical Properties of High Temperature Superconductors I, World Scientific Publ. Singapore 1989, D. M. Ginsburg ed Ch.1)

41. P. Halder, A. Roig-Janicki, S. Sridhar and B. C. Giessen, Materials Lett. 7, 1 (1988).

42. J. P. Franck, J. Jung, W. A. Miner and M. A.-K. Mohamed, Phys. Rev. B 38, 754 (1988).

43. Z. Z. Sheng, A. M. Hermann, A. El Ali, C. Almasan, J. Estrada, T. Datta, R. J. Matson, Phys. Rev. Lett. 60, 937 (1988).

44. H. W. Zandbergen, P. Groen, G. Van Tendeloo, J. Van Landuyt and S. Amelinckx, Sol. St. Commun. 66, 397 (1988).

45. H. W. Zandbergen, G. Van Tendeloo, J. Van Landuyt and S. Amelinckx, Appl. Phys. A 46, 233 (1988).

46. J. M. Tarascon, Y. LePage, P. Barboux, B. G. Bagley, L. H. Greene, W. R. McKinnon, G. W. Hull, M. Giroud and D. M. Hwang, Phys. Rev. B 37, 9382 (1988).

171

47. R. M. Hazen, L. W. Finger, R. J. Angel, C. T. Prewitt, N. L. Ross, C. G. Hadidiacos, P. J. Heaney, D. R. Veblen, Z. Z. Sheng, A. El Ali and A. M. Hermann, Phys. Rev. Lett. 60, 1174 (1988).

48. K. Hiraga, D. Shindo, M. Hirabayashi, M. Kikiuchi, N. Kobayashi, Y. Syono, Jap. J. Appl. Phys. 27, L1848 (1988).

49. S. S. P. Parkin, V. Y. Lee, E. M. Engler, ^ ' ^azzal. T. C. Huang, G. Gorman, R. Savoy, and R. Beyers ᵣ ~ ι Lett. 60, 2539 (1988).

50. J. Yu, A. J. Freeman and J.-H. Xu, Phys. Rev. Lett. 58, 1035 (1987); L. F. Mattheiss, Phys. Rev. Lett. 58, 1028 (1987).

51. S. Massidda, J. Yu, A. J. Freeman and D. D. Koelling, Phys. Lett. A 122, 198 (1987); J. Yu, S. Massidda, A. J. Freeman and D. D. Koelling, Phys. Lett. A 122, 203 (1987).

52. S. Massidda, J. Yu and A. J. Freeman, Physica C 152, 251 (19 H. Krakauer and W. E. Pickett, Phys. Rev. Lett. 60, 1 ᵣ88).

53. L. C. . dskjaer, J. Z. J ι, R. Benedek, D. G. Legnini, D. J. Lam, M. D. Stahulak, H. Claus and A. Bansil, Physica C 156, 269 (1988); A. Bansil, R. Pankaluoto, R. S. Rao, P. E. Mijnarends, W. Dlugosz, R. Prasad and L. C. Smedskjaer, Phys. Rev. Lett. 61, 2480 (1988).

54. S. W. Tozer, A. W. Kleinsasser, T. Penney, D. Kaiser and F. Holtzberg, Phys. Rev. Lett. 59, 1768 (1987).

55. S. J. Hagen, T. W. Jing, Z. Z. Wang, J. Horvath and N. P. Ong, Phys. Rev. B 37, 7928 (1988).

56. L. Forro, M. Raki, C. Ayache, P. C. E. Stamp, J. Y. Henry and

J. Rossat-Mignod, Physica C <u>153-155</u>, 1   1988).

57. Y. Iye, T. Tamegai, H. Takeya and H. Takei, Jap. J. Appl. Phys. <u>27</u>, L658 (1989).

58. Y. Iye, International J. of Mod. Phys. B <u>3</u>, 367 (1989).

59. S. Martin, A. T. Fiory, R. M. Fleming, L. F. Schneemeyer and J. V. Waszczak, Phys. Rev. Lett. <u>60</u>, 2194 (1988).

60. B. T. Matthias, H. Suhl and E. Corenzwit Phys. Rev. Lett. <u>1</u>, 92-94, 152 (1958); M. Decrous and Ø. Fischer, <u>Superconductivity in Ternary Compounds II</u>, Springer, Berlin (1982), M. B. Maple and Ø. Fischer eds. Ch. 3.

61. G. W. Crabtree, W. K. Kwok, A. Umezawa, L. Soderholm, L. Morss and E. E. Alp, Phys. Rev. B <u>36</u>, 5258 (1987).

62. W. K. Kwok, G. W. Crabtree, D. G. Hinks, K. Zhang, and C. H. Sowers, J. Less Comm. Metal <u>153</u>, 193 (1989).

63. B. Büchner, U. Calließ, H. D. Jostarndt, W. Schlabitz and D. Wohlleben, Sol. St. Comm. <u>73</u>, 357 (1990).

64. P. Halder, K. Chen, B. Maheswaran, A. Roig-Janicki, N. K. Jaggi, R. S. Markiewicz and B. C. Giessen, Science <u>241</u>, 1198 (1988).

65. G. W. Crabtree, W. K. Kwok and A. Umezawa, <u>Quantum Field Theory as an Interdisciplinary Basis</u>, World Scientific Publ. Singapore (1988), F. C. Khanna, H. Umezawa, G. Kunstatter and H. C. Lee eds. Ch. 26.

66. A. P. Malozemoff, <u>Physical Properties of High Temperature Superconductors I</u>, World Scientific Publ. Singapore (1989), D. M. Ginsburg ed. Ch3.

67. P. L. Gammel, D. J. Bishop, G. J. Dolan, J. R. Kwo, C. A. Murray, L. F. Schneemeyer, and J. V. Waszczak Phys. Rev. Lett. 59, 2592 (1987).

68. M. E. Hawley, K. E. Gray, D. W. Capone II and D. G. Hinks, Phys. Rev. B 35, 7224 (1987).

69. R. S. Gonnelli, D. Andreone, V. Lacquaniti, F. Abbattista and M. Vallino Phys. Rev. B 39, 2261 (1989).

70. T. Timusk and D. B. Tanner, Physical Properties of High Temperature Superconductors I, World Scientific Publ. Singapore (1989), D. M. Ginsburg ed. Ch7.

71. S. E. Inderhees, M. B. Salamon, N. Goldenfeld, J. P. Rice, B. G. Pazol, D. M. Ginsberg, J. Z. Liu and G. W. Crabtree, Phys. Rev. Lett. 60, 1178 (1988).

72. W. Meissner and R. Ochsenfeld, Naturwissenschaften 21, 787 (1933).

73. H. Fröhlich, Phys. Rev. 79, 845 (1950); H. Fröhlich, Proc. Roy. Soc. A 215, 291 (1952).

74. J. N. Cooper, Phys. Rev. 104, 1189 (1956).

75. P. G. deGennes, Superconductivity of Metals and Alloys, Adisson Wesley, New York (1989).

76. J. Bardeen, L. N. Cooper and J. R. Schrieffer, Phys. Rev. 108, 1175 (1957).

77. Z. Ye and H. Umezawa, submitted to Physica C (1991).

78. F. London and H. London, Proc. Roy. Soc. A149, 71 (1935).

79. M. Tinkham, Introduction to Superconductivity, Krieger Publ. Florida (1980).

80. A. B. Pippard, Proc. Roy. Soc. A216, 547 (1953).

81. V. L. Ginzburg and L. D. Landau, Zh. Eksperim. i Teor. Fiz. 20, 1064 (1950).

82. L. D. Landau and E. M. Lifshitz, Statistical Physics, Pergamon Pr. Oxford (1980).

83. C. J. Gorter and H. B. G. Casmir, Physica 1, 306 (1934).

84. G. Rickayzen, Superconductivity, Marcel Dekker, New York (1969), Parks ed. Ch. 2.

85. A. L. Fetter and P. C. Hohenberg, Superconductivity, Marcel Dekker, New York (1969), Parks ed. Ch. 14.

86. D. J. St. James, G. Sarma and E. J. Thomas, Type II Superconductivity, Pergamon Pr. Oxford, (1969).

87. D. Cribier, B. Jacrot, L. Madhav Rao and B. Farnoux, Phys. Lett. 9, 106 (1964); D. Cribier, B. Farnoux, B. Jacrot, L. Madhav Rao, B. Vivet and M. Antonini, Proceedings of the Ninth International Conference on Low Temperature Physics, Plenum Pr. New York (1965) J. G. Daunt, D. O. Edwards, F. J. Milford andM Yaqub eds. p.509.

88. D. R. Tilley, G. J. Van Gurp and C. W. Berghout, Phys. Lett. 12, 305 (1964).

89. H. Teichler, Anisotropic Effects in Superconductors, Plenum Pr. New York (1977), H. W. Weber ed. Ch. 1.

90. H. W. Weber, E. Seidl, C. Laa, E. Schachinger, M. Prohammer, A. Junod and D. Eckert, manuscript.

91. P. de Trey, S. Gygax and J. -P. Jan, J. Low Temp. Phys. 11, 421 (1973).

175

92. R. C. Morris, R. V. Coleman and R. Bhandari Phys. Rev. B 5, 895 (1972).

93. R. Klemm, Ph.D. Thesis, Harvard Univeristy (1974).

94. G. R. Stewart, Rev. Mod. Phys. 56, 755 (1984).

95. A. Sulpice, P. Gandit, J. Chaussy, J. Flouquet, D. Jaccard, P. Lejay and J. L. Tholence, J. Low Temp. Phys. 62, 39 (1986).

96. S. Adenwalla, S. W. Lin, Q. Z. Ran, Z. Zhao, J. B. Ketterson. J. A. Sauls, L. Taillefer, D. G. Hinks, M. Levy and B. K. Sarma Phys. Rev. Lett. 65, 2298 (1990).

97. V. L. Ginzburg, Zh. Eksper. Teor. Fiz. 23, 236 (1952).

98. W. Lawrence and S. Doniach, Proceedings of the Twelfth International Conference on Low Temp. Phys. Academic of Japan, Kyoto (1970) p.361.

99. Lawrence and Doniach (1971) publ unknown.

100. D. R. Tilley, Prog. Phys. Soc. 85, 1177 (1965).

101. D. R. Tilley, Proc. Phys. Soc. 86, 289 (1965).

102. R. A. Klemm and J. R. Clem, Phys. Rev. B 21, 1868 (1980).

103. V. G. Kogan, Phys. Rev. B 24,1572 (1981).

104. A. V. Balatskii, L. I. Burlachov and L. P. Gor'kov, Sov. Phys. JETP 63, 866 (1986).

105. H. W. Weber, Kerntechnik 53, 189 (1989).

106. J. W. Ekin, J. R. Gavaler and J. Gregg, Appl. Phys. Lett. 41, 996 (1982).

107. P. W. Anderson, Phys. Rev. Lett. 9, 310 (1962).

108. C. P. Bean, Rev. Mod. Phys. 36, 31 (1964).

109. Y. B. Kim, C. F. Hempstead and A. R. Strnad, Phys. Rev. 129, 528 (1963).

110. O. V. Lounasmaa, Experimental Principles and Methods Below 1 K, Academic Pr. New York (1974).

111. A. Umezawa, M. Sc. Thesis, The University of Alberta (1986).

112. R. J. Cava, B. Batlogg, R. B. van Dover, D. W. Murphy, S. Sunshine, T. Siegrist, J. P. Remeika, E. A. Rietman, S. Zahurak and G. P. Espinosa, Phys. Rev. Lett. 58, 1676 (1987).

113. A. Umezawa, G. W. Crabtree, J. Z. Liu, H. W. Weber, W. K. Kwok. L. H. Nunez, T. J. Moran, C. H. Sowers and H. Claus, Phys. Rev. B 36, 7151 (1987).

114. K. G. Vandervoort, G. Griffith, H. Claus and G. W. Crabtree, Rev. Sci. Inst. in press (1991).

115. H. Claus, G. W. Crabtree, J. Z. Liu, W. K. Kwok, and A. Umezawa, J. Appl. Phys. 63, 4170 (1988).

116. B. W. Veal, W. K. Kwok, A. Umezawa, G. W. Crabtree, J. D. Jorgensen, J. W. Downey, L. J. Nowicki, A. W. Mitchell, A. P. Paulikas and C. H. Sowers, Appl. Phys. Lett. 51, 279 (1987).

117. P. Chaudahari, R. H. Koch, R. B. Laibowitz, T. R. McGuire and R. J. Gambino, Phys, Rev. Lett. 58, 2684 (1987).

118. D. C. Larbalestier, M. Daeumling, X. Cai, J. Seuntjens, J. McKinnell, D. Hampshire, P. Lee, C. Meingast, T. Willis, H. Muller, R. D. Ray, R. G. Dillenburg, E. E. Hellstrom and R. Joynt, J. Appl. Phys. 62, 3308 (1987).

119. A. J. Panson, A. I. Braginski, J. R. Gavaler, J. K. Hulm, M. A. Janocko, H. C. Pohl, A. M. Stewart, J. Talvacchio and G. R. Wagner, Phys. Rev. B 35, 887 (1987).

120. U. Welp, W. K. Kwok, G. W. Crabtree, K. G. Vandervoort and J. Z. Liu, Appl. Phys. Lett. 57, 84 (1990).

121. G. J. Dolan, G. V. Chandrashekhar, T. R. Dinger, C. Feild, and F. Holtzberg, Phys. Rev. Lett. 62, 827 (1989).

122. W. K. Kwok, U. Welp, G. W. Crabtree, K. G. Vandervoort, R. Hulscher and J. Z. Liu, Phys. Rer. Lett. 64, 966 (1990).

123. E. M. Gyorgy, R. B. van Dover, L. F. Schneemeyer, A. E. White, H. M. O'Bryan, R. J. Felder, J. V. Wasczak, W. W. Rhodes and F. Hellman, Appl. Phys. Lett. 56, 2465 (1990).

124. J. Z. Liu, Y. X. Jia, R. N. Shelton, and M. J. Fluss, Phys. Rev. Lett. 66, 1354 (1991).

125. J. Clem, private communication, Iowa State University.

126. H. W. Weber, G. W. Crabtree, A. Umezawa, J. Z. Liu and L. H. Nunez, High T$_c$ Superconductors, Plenum Press New York (1988), H. W. Weber ed. p. 273.

127. H. W. Weber, G. W. Crabtree, A. Umezawa, J. Z. Liu, W. L. Kwok and W. K. Kwok, MRS Int'l. Mtg. on Adv. Mat. 6, 365 (1989).

128. J. R. Cost, J. O. Willis, J. D. Thompson, and D. E. Peterson, Phys. Rev. B 37, 1563 (1988).

129. S. T. Sekula, D. K. Christen, H. R. Kerchner, J. R. Thompson, L. A. Boatner, and B. C. Sales, Jpn. J. Appl. Phys. 26, Suppl. 3, 1185 (1987).

130. A. R. Sweedler, D. L. Snead Jr. and D. E. Cox, <u>Treatise on Materials Science and Technology</u>, Academic Press, New York (1979), T. Luhman and D. Dew-Hughes ed. Vol. 14, p. 349.

131. F. M. Sauerzopf, H. P. Wiesinger, H. W. Weber, G. W. Crabtree and J. Z. Liu, Physica C 162-164, 751 (1989), F. M. Sauerzopf, H. P. Wiesinger, W. Kritscha, H. W. Weber, G. W. Crabtree and J. Z. Liu, Phys. Rev. B in press (1991).

132. H. W. Weber, F. M. Sauerzopf, H. P. Wiesinger, W. Kritcha, G. W. Crabtree, J. Z. Liu, M. C. Frischherz and M. A. Kirk, <u>Proc. ICMC 90 (Topical Conference on Materials Aspects of High Temperature Superconductors)</u>, Verlag, Oberursel (1991) H. C. Freqhardt, R. Flukiger and M. Peukert ed. Vol. 2 p. 981; H. W. Weber, H. P. Wiesinger, W. Kritcha, F. M. Sauerzopf, G. W. Crabtree, J. Z. Liu, Y. C. Chang and P. Z. Jiang, Supercond. Sci. Tech. <u>4</u>, s 103 (1991).

133. R. B. van Dover, E. M. Gyorgy, L. F. Schneemeyer, J. W. Mitchell, K. V. Rao, R. Puzniak and J. V. Wazczak Nature <u>342</u>, 55 (1989).

134. A. C. Rose-Innes and E. H. Rhoderick, <u>Introduction to Superconductivity</u>, Pergamon Pr. New York (1978).

135. D. R. Harshman, G. Aeppli, E. J. Ansaldo, B. Batlogg, J. H. Brewer, J. F. Carolan, R. J. Cava, M. Celio, A. C. D. Chaklader, W. N. Hardy, S. R. Kreitzman, G. M. Luke, D. R. Noakes, M. Senba, Phys. Rev. B. <u>36</u>, 2386 (1987); D. R. Harshman, L. F. Schneemeyer, J. V. Waszczak, G. Aeppli, R. J. Cava, B. Batlogg,

179

L. W. Rupp, E. J. Ansaldo, and D. Ll. Williams, Phys. Rev. B 39, 851 (1989).

136. B. Pümpin, H. Keller, W. Kundig, W. Odermatt, I. M. Savic', J. W. Schneider, H. Simmler, P. Zimmermann, J. G. Bednorz, Y. Maeno, K. A Müller, C. Rossel, E. Kalidis, S. Rusiecki, W. Assmus, and J. Kowalewski, Physica C 162-164, 151 (1989).

137. Z. Hao and J. R. Clem, Phys. Rev. B 43, 2844 (1991).

138. A. Umezawa, G. W. Crabtree, K .G. Vandervoort, U. Welp, W. K. Kwok and J. Z. Liu, Physica C 162-164, 733 (1989).

139. M. Däumling and D. C. Larbalestier, Phys. Rev. B 40, 9350, (1989).

140. J. A. Osborn, Phys. Rev. 67, 351 (1945).

141. M. V. Kartsovnik, V. A. Larkin, V. V. Ryazanov, N. S. Sidorov ind I. F. Shchegolev, Pis'ma Zh. Eksp. Teor. Fiz. 47, 595 (1988) [JETP Lett. 47, 691 (1988)].

142. J. P. Ströbel, A. Thomä, B. Hensel, H. Adrian, and G. Saemann Ischenko, Physica C 153-155, 1537 (1988).

143. Y. Ishikawa, K. Mori, K. Kobayashi, and K. Sato, Physica C 153-155, 1471 (1988).

144. H. Adrian, W. Assmus, A. Höhr, J. Kowaleski, H. Spille and F. Steglich, Physica C 162-164, 329 (1989).

145. M. Wacenovsky, H. W. Weber, O. B. Hyunn, and D. K. Finnemore, Physica C 162-164, 1629 (1989).

146. S. Sridar, D. H. Wu, and W. Kennedy, Phys. Rev. Lett. 63, 1873 (1989).

147. L. Krusin-Elbaum, R. L. Greene, F. Holtzberg, A. P. Malozemoff and Y. Yeshurun, Phys. Rev. Lett. 62, 217 (1989).

148. R. J. Cava, B. Batlogg, S. A. Sunshine, T. Siegrist, R. M. Fleming, K. Rabe, L. F. Schneemeyer, D. W. Murphy, R. B. van Dover, P. K. Gallagher, S. H. Glarum, S. Nakahara, R. C. Farrow, J. J. Krajewski, S. M. Zahurak, J. V. Wazczak, J. H. Marshall, P. Marsh, L. W. Rupp Jr., W. F. Peck and E. A. Rietman, Physica C 153-155, 560 (1988).

149. A. J. Jacobson, J. M Newsam, D. C. Johnston, D. P. Goshorn, J. T. Lewandowski and M. S. Alvarez, Phys. Rev. B 39, 254 (1989).

150. A. Umezawa, G. W. Crabtree, U. Welp, W. K. Kwok, K. G. Vandervoort and J. Z. Liu, Phys. Rev. B 42, 8744 (1990).

151. U. Welp, S. Fleshler, W. K. Kwok, J. Downey, Y. Fang, G. W. Crabtree and J. Z. Liu, Phys. Rev. B 42, 10189 (1990).

152. T. A. Friedmann, M. W. Rabin, J. Giapintzakis, J. P. Rice, and D. M. Ginsberg, Phys. Rev. B 42, 6217 (1990).

153. Z. Schlesinger, R. T. Collins, F. Holtzberg, C. Feild, S. H. Blanton, U. Welp, G. W. Crabtree, Y. Fang and J. Z. Liu, Phys. Rev. Lett. 65, 801 (1990).

154. K. G. Vandervoort, U. Welp, J. E. Kessler, H. Claus, G. W. Crabtree, W. K. Kwok, A. Umezawa, B. W. Veal, J. W. Downey and A. P. Paulikas, Phys. Rev. B in press (1991).

155. G. J. Dolan, F. Holtzberg, C. Feild and T. R. Dinger, Phys. Rev. Lett. 62, 2184 (1989).

156. L. J. Swartzendruber, A. Roitburd, D. L. Kaiser, F. W. Gayle, and L. H. Bennett, Phys. Rev. Lett. 64, 483 (1990).

157. A. A. Abrikosov and A. I. Buzdion, Pis'ma Zh. Eksp. Teor. Fiz. **47**, 204 (1988) [JETP Lett. **47**, 247 (1988)].

158. A. I. Buzdin, B. U. Vujicic, and D. A. Kupstov, Supercond. Sci. Technol. **2**, 249 (1989).

159. L. I. Burlachov and L. I. Glazeman, Physica C **166**, 75 (1990).

160. M. M. Fang, V. G. Kogan, D. K. Finnemore, J. R. Clem, L. S. Chumbley and D. E. Farrell, Phys. Rev. B **37**, 2334 (1988).

161. J. C. Martinez, J. J. Préjean, J. Karpinski, E. Kaldis and P. Bordet, Sol. St. Comm. **75**, 315 (1990).

162. U. Welp, S. Fleshler, W. K. Kwok, K. G. Vandervoort, J. Downey, B. Veal and G. W. Crabtree, manuscript, Argonne National Laboratory (1991).

163. E. M. Gyorgy, R. B. van Dover, K. A. Jackson, L. F. Schneemeyer and J. V. Waszczak, Appl. Phys. Lett. 55 283 (1989).

Appendix I

In 1950 F. London suggested that the trapped flux inside a superconducting ring is quantized. This assumption led to the eventual prediction of magnetic vortices in type II superconductors.[1] Assuming that the order parameter is complex so that

$$\psi = |\psi| e^{(i\phi)}, \tag{A1-1}$$

then the second GL equation (3-30) can be written

$$j = \left(\frac{2e\hbar}{m}\right)|\psi|^2 \nabla\phi - \frac{4e^2}{mc}|\psi|^2 A. \tag{A1-2}$$

Taking a line integral around a closed loop Γ surrounding the superconducting ring, one can get the flux passing through the loop.

$$\int_\Gamma A \cdot dl = \int_\Sigma \text{curl} A \cdot d\sigma = \int_\Sigma h \cdot d\sigma = \Phi \tag{A1-3}$$

Isolating A in (A1-2) and combining it with (A1-3) gives

$$\Phi = \int_\Gamma \left(\frac{c\hbar}{2e}\right) dl - \int_\Gamma \left(\frac{mc}{4e^2}\right) \frac{j}{|\psi|^2} \cdot dl. \tag{A1-4}$$

Since the order parameter modulus must be single valued (the phase varies by $2\pi n$) when making a complete turn around Γ, (A1-4) can be rewritten as

$$\Phi = \left(\frac{nc\hbar}{2e}\right) - \frac{mc}{4e^2} \int_\Gamma \left(\frac{j}{|\psi|^2}\right) dl. \tag{A1-5}$$

Φ is defined as a fluxoid. The first term in (A1-5) gives the flux that has entered the ring while the second term represents any current that is flowing along the path integral. Choosing Γ such

183

that j=0, the last term of (A1-5) goes to zero and the flux within this ring can be written as,

$$\Phi = n\frac{ch}{2e} = n\Phi_0 \qquad (A1-6)$$

where Φ_0 is the flux quantum, $\Phi_0 = 2 \times 10^{-7}$ G cm^2. Thus the flux inside a superconducting ring is quantized in intergral numbers of Φ_0.

1   A. A. Abrikosov, Pis'ma Zh. Eksp. Teor. Fiz. 32, 1442 (1957) [JETP Lett. 5, 1147 (1957)]

Appendix II

The form of Equation (3-110) is derived from Maxwell equation (3-16), assuming a linear internal field gradient having the slope H^*/R. The form of equation (3-16) is written for the Gaussian system of units[1], where H is in Gauss, R is in cm, $c = 3 \times 10^{10}$ cm/s and j is in statamp/cm^2. The units that the critical current density is most often written in is A/cm^2 where the conversion of statamp/cm^2 to A/cm^2 is

$$1 \frac{A}{cm^2} = 3 \times 10^9 \frac{statamp}{cm^2}. \qquad (A2\text{-}1)$$

Rewriting equation (3-16) into the form

$$j_c = \frac{-c}{4\pi}\left(\frac{H^*}{R}\right), \qquad (A2\text{-}2)$$

the corresponding relation for the units can be written

$$j_c\left(\frac{statamp}{cm^2}\right) = \frac{3 \times 10^{10}\left(\frac{cm}{s}\right)}{4\pi}\frac{H^*(G)}{R(cm)}. \qquad (A2\text{-}3)$$

Equation A2-3 states that to keep both sides of the equation consistent, the net units on the right hand side of the equation must be statamp/cm^2. To change the basis of units of j_c to A/cm2, the units of right hand side of (A2-3) must be changed using (A2-1). Thus, j_c can be written in A/cm2 by writing (A2-3) in the form

$$j_c\left(\frac{A}{cm^2}\right) \qquad (A2\text{-}4)$$

$$= \frac{3 \times 10^{10}\left(\frac{cm}{s}\right)}{4\pi}\frac{H^*(G)}{R(cm)}\frac{1\frac{A}{cm^2}}{3 \times 10^9 \frac{statamp}{cm^2}}.$$

Equation (A2-4) can be more conveniently written by writing c=10 so that

$$j_c\left(\frac{A}{cm^2}\right) = \frac{10\left(\frac{cm}{s}\right)}{4\pi}\frac{H^*(G)}{R(cm)}\frac{1\frac{A}{cm^2}}{1\frac{statamp}{cm^2}} \qquad (A2-5)$$

which is in the form (3-110).

---

1   J. D. Jackson, Classical Electromagnetism, J. Wiley and Sons, New York (1975).

Appendix III

The basic method for the growth of single crystal $YBa_2Cu_3O_{7-\delta}$ is discussed by Kaiser et al.[1], Schneemeyer et al.[2], and Liu et al.[3] The method used for growing single crystal $YBa_2Cu_3O_{7-\delta}$ is commonly called a self flux method because the flux that is used to grow the crystals is composed of the same material as the crystal itself. For $YBa_2Cu_3O_{7-\delta}$, the starting materials most commonly used to grow the crystals are Y_2O_3, $BaCO_3$ and CuO powders. Separately, these three powders have very high melting points (> 1500 ° C). However when they are mixed together, a solid state reaction occurs between the materials at much lower temperatures.

For $YBa_2Cu_3O_{7-\delta}$ powder, the three starting materials are mixed in the proper stoichiometric ratio of the metallic ions equal to the $YBa_2Cu_3O_{7-\delta}$ final product. Thus the starting materials are mixed in the ratio of; half mole of Y_2O_3 vs. two moles of $BaCO_3$ vs. three moles of CuO. It is important to obtain maximum homogeneity when mixing the starting materials to ensure proper stoichiometry of the finished product. This involves careful grinding of the starting material and pre-reacting the mixture at lower temperatures with re-grinding between each pre-reaction, before the final reaction at 900 ° C takes place. One method for producing fine grain powder of starting material is by grinding the powder in a ball mill.

The starting stoichiometry used to grow single crystal $YBa_2Cu_3O_{7-\delta}$ is higher in $BaCO_3$ and CuO content than that of the

polycrystal. The excess $BaCO_3$ and CuO become the flux necessary to grow the single crystals. Without the proper amount of flux added to the starting mixture only very small crystals, if any, will be formed.

The flux is found to be quite corrosive and may react with the crucible that is holding the mixture[4]. This crucible corrosion may result in crucible material to enter the single crystals and become impurities. Several types of crucibles (Pt, AlO_2, ZrO_2 and Au) were tested when growing the single crystals. Of the crucibles tested, only the crystals grown in ZrO_2 and Au crucibles were found to have high superconducting transitions. The crystals provided by Dr. Liu were also grown in Au crucibles.

The method that has so far produced the best single crystals with respect to size and quality will be discussed. Au crucibles were used to grow the crystals. The stoichiometry of the starting mixture was a 1-4-10 ratio of Y-Ba-and Cu. Thus for every half mole of Y_2O_3, four moles of $BaCO_3$ and ten moles of CuO were added. The starting powders were mixed and pressed into pellets, placed in the gold crucible and fired in air. The mixture was initially fired at 925 ° C for four hours. The sample was then heated to 980 ° C for one and a half hours to melt the mixture. The mixture was then slow cooled at a slow rate of 4 °C/hour, down to 890 ° C to ensure proper crystallization. Finally the mixture was cooled to room temperature at a rate of 100 °C/hour.

This growth procedure resulted in small platelike crystals to be formed within the flux. The size of the samples ranged from 1

to 3 mm along the face of the plate and 0.2 to 0.5 mm in thickness. The c axis was always found to be along the thickness of the plate. When measured inductively in a field of 1 G, the as-grown samples were found to have low T_c (T_c < 90 K) and a large transition width (ΔT_c > 50 K). After annealing the samples at 400 ° C in flowing oxygen for ten days, Tc was found to increase (Tc ~ 92 K) and become much sharper (ΔT_c < 1 K). The superconducting transitions of these crystals were found to be similar to the transitions of new single crystals (made by Dr. Liu) as discussed in Ch. 5. X-ray analysis of these single crystals found them to be single phase, having the unit cell dimensions given in Ch. 2.

1   D. Kaiser, F. Holtzberg, M. F. Chisolm and T. K. Worthington, J. Cryst. Growth 85, 593 (1987).

2   L. F. Schneemeyer, J. V. Waszczak, T. Siegrist, R. B. van Dover, L. W. Rupp, B. Batlogg, R. J. Cava and D. W. Murphy, Nature 328, 601 (1987).

3   J. Z. Liu, G. W. Crabtree, A. Umezawa and Li Zongquan, Phys. Lett. A. 121, 305 (1987).

4   H. J. Scheel, W. Sadowski and L. Schellenberg, Supercond. Sci. Technol. 2, 17 (1989).
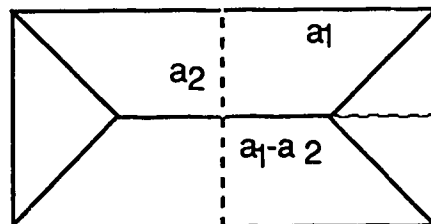
Appendix IV

For a rectangle of dimensions $2a_1 \times 2a_2$, shown in Figure A4-1,

Figure A4-1
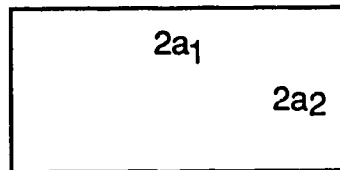
assuming isotropic field penetration and ignoring corner effects, the field would fully penetrate the sample along a_2 before a_1. The resulting geometry of the field penetration at $H = H^*$ would have a tent-like structure shown in Figure A4-2.

Figure A4-2

To calculate $\int H dv$, the sample can be integrated in two sections, A (unshaded) and B (shaded) as shown in Figure A4-3.

Figure A4-3
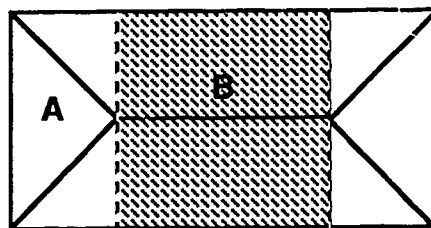
For section A, assuming x to be the axis along a_1 and y to be the axis along a_2, since the field penetration is assumed to be uniform the diagonal line going down the sample is of the form $x = y$ where the local field along y is written as

$$h(y) = \frac{H^*}{a_2} y.$$ (A4-1)

So the internal field in section A is written

$$\int H dv = L8 \int_0^{a_2} \int_0^x \left(\frac{H^*}{a_2}\right) y \, dy \, dx = L8 \left(\frac{H^*}{a_2}\right)\left(\frac{a_2^3}{3}\right)$$ (A4-2)

where L is the length of the sample along the field. For section B, since there is no field penetration along the x axis, the internal field is just the local field integrated along the y axis,

$$\int H dv = L4(a_1 - a_2) \int_0^{a_2} \left(\frac{H^*}{a_2}\right) y \, dy$$

$$= L2H^* (a_1 a_2 - a_2^2).$$ (A4-3)

The total internal field is the sum of (A4-2) and (A4-3)

$$\int H dv = L\left[2H^* a_1 a_2 - 2H^* a_2^2 + \frac{8}{3} (H^* a_2^2)\right]$$

$$= L2\{H^* a_1 a_2 + \frac{1}{3} (H^* a_2^2)\}.$$ (A4-4)

So from (A4-4) the average internal magnetic induction given by equation (3-106) is written for $H = H^*$

191

$$B = \frac{L2\{H^*a_1a_2 + \frac{1}{3}(H^*a_2{}^2)\}}{L4a_1a_2}$$

$$= \frac{H^*}{2}\{1 + \frac{1}{3}\left(\frac{a_2}{a_1}\right)\}. \qquad (A4-5)$$

The net diamagnetism at H = H* is just the difference between H* and equation (A4-5), which is

$$-4\pi M = H^* - \frac{H^*}{2}\{1 + \frac{1}{3}\left(\frac{a_2}{a_1}\right)\}$$

$$= \frac{H^*}{2}\{1 - \frac{1}{3}\left(\frac{a_2}{a_1}\right)\}. \qquad (A4-6)$$

As discussed in Ch. 3, a result of the Bean model is that the amount of diamagnetism remains constant for fields above H* so that expression (A4-6) represents the diamagnetic signal for all fields H ≥ H*. From Maxwell's equations, for H along the z direction

$$\text{curl}H = \frac{dH}{dy}i + \frac{dH}{dx}j, \qquad (A4-7)$$

and assuming the field gradient to be the same along x and y so that

$$\frac{dH}{dy} = \frac{dH}{dx} = \frac{H^*}{a_2}, \qquad (A4-8)$$

j_c can be related to H* by the relation

$$\frac{H^*}{a_2} = \frac{4\pi j_c}{10}. \qquad (A4-9)$$

Substituting equation (A4-9) into equation (A4-6) gives the result

$$-M = \frac{a_2}{20}j_c\{1 - \frac{1}{3}\frac{a_2}{a_1}\}. \qquad (A4-10)$$

192

Vita

Ado Umezawa was born on September 17, 1962 in Tokyo
Japan and is the younger of two brothers. He arrived in Edmonton,
Alberta in 1975, where he attended Harry Ainlay Composite High
School. He was admitted into the Faculty of Science at the
University of Alberta in 1980 and graduated with a Bachelor of
Science degree in physics in 1984. In 1984, he was admitted into
the Faculty of Graduate Studies at the University of Alberta, where
he conducted research in the magnetic and superconducting
properties of rare earth compounds. He received a Masters of
Science degree in physics in 1986. In 1986, he joined Argonne
National Laboratory in Argonne, Illinois as a visiting student
associate from the University of Alberta, under a joint educational
program between the two institutions. His research at Argonne
involved the electromagnetic characterization of various high T_c
superconductors and rare earth compounds. This thesis is a result
of some of that research.